Dynamics of Space-Charge and Molecules on Surfaces Investigated by Means of Picosecond Low-Energy-Electron-Diffraction

---

Dissertation

zur

Erlangung der naturwissenschaftlichen Doktorwürde
(Dr. sc. nat.)

vorgelegt der

Mathematisch-naturwissenschaftlichen Fakultät

der

Universität Zürich

von

Claudio Cirelli
aus Italien

Promotionskomitee

Prof. Dr. Jürg Osterwalder
Prof. Dr. Thomas Greber
Prof. Dr. Herbert Over

Zürich 2006

Die vorliegende Arbeit wurde von der Mathematisch-naturwissenschaftlichen Fakultät der Universität Zürich auf Antrag von Prof. Dr. Jürg Osterwalder und Prof. Dr. Hans-Werner Fink als Dissertation angenommen.

Abstract

In order to observe phenomena on the molecular level, it is necessary to develop a technique that is sensitive to all the microscopic spatial degrees of freedom on the time scale of the molecular processes. For the case of surface physics, the standard tool for structure determination is Low-Energy-Electron-Diffraction (LEED). This technique, endowed in a pump-probe experiment framework has the potential to follow in real time the excitation and the relaxation dynamics at surfaces on the picosecond time scale.

This thesis describes the realization of the first proof-of-principle experiment for time-resolved LEED (t-LEED).

The surface sensitivity of low-energy electrons is guaranteed by the fact that their elastic scattering cross-section is larger than for high-energy electrons or X-ray photons. However, this advantage has to be paid for by the difficulty to obtain electron pulses with an appreciable time width, which defines the experimental time resolution. Therefore, one of the key-points for the realization of photon-pump electron-probe experiments resides in the generation of the electron pulses and in their propagation towards the sample surface. In the present work the design, realization and characterization of a new home-built electron gun is presented. A temporal spread of electron pulses of few tenths of picoseconds and a flux of about 1 electron/pulse were achieved at the sample position at 65 eV.

Low-energy electrons are also the most suitable tool to study surface space-charge effects: an intense pump pulse produces on a metal surface the emission of electrons via multi-photon absorption processes. The generation and temporal evolution of this electron cloud can be probed with low-energy electron pulses, since the time constants of the diffraction process and of short-lived space-charge are in the same order of magnitude. Furthermore, a detailed investigation of this phenomenon permits to disentangle changes in the spot intensity due to effective structural dynamics from those due to space-charge effects.

In an intensive study of the dynamics of space-charge produced by pump laser pulses on Cu(111), it is found that the 55 eV probe electrons gain up to 60 meV and their energy spectrum is narrowed during the interaction time with the space-charge photoelectrons. If the pump fluence is limited below a certain value, space-charge effects become negligible and if the structural changes of the system are significant even at low pump fluence, then transient changes in the LEED spot intensity can be related to effective surface structural changes. This is the case of the first-order order-disorder phase transition which occurs for a C_{60} multilayer adsorbed on Ag(111) below 225 K, where the molecular rotation stops. The main achievement of this thesis is the successful observation of this phase transition in real-time by means of t-LEED.

Zusammenfassung

Zur Beobachtung molekularer Phänomene in Echtzeit benötigt man eine Methode, welche atomare Strukturen mit einer Zeitauflösung im Bereich der Zeitkonstanten mikroskopischer Prozesse vermessen kann. Die relevanten Skalen sind hierbei Nanometer ($1\,\mathrm{nm} = 10^{-9}\,\mathrm{m}$) und Picosekunden ($1\,\mathrm{ps} = 10^{-12}\,\mathrm{s}$). In der Oberflächenphysik ist die Beugung nieder-energetischer Elektronen (LEED, engl. für Low-Energy-Electron Diffraction) die Standardmethode zur Bestimmung atomarer Strukturen. In dieser Dissertation wird die Realisierung des ersten erfolgreichen zeitaufgelösten LEED-Experimentes beschrieben.

Die Oberflächenempfindlichkeit nieder-energetischer Elektronen mit Energien von etwa 100 eV ist begründet in hohen Streuquerschnitten, die jene von hoch-energetischen Elektronen und Röntgenphotonen teilweise um Grössenordnungen übersteigen. Der Vorteil hoher Streuquerschnitte muss allerdings mit technischen Schwierigkeiten bei der Herstellung sehr kurzer Elektronenpulse bezahlt werden, wobei die Pulslänge in diesen Experimenten die erreichbare Zeitauflösung definiert. Aufgrunddessen kommt der Erzeugung und der Propagation der Elektronenpulse zur Probe hin zentrale Bedeutung zu. In dieser Arbeit werden Design, Realisierung und Chrakterisierung einer neuen, selbst gebauten Elektronenquelle vorgestellt. Mit dieser Quelle können Elektronenpulse mit Längen von nur mehreren zehn Picosekunden erzeugt werden bei einem relativ hohen Elektronenfluss von einem Elektron pro Puls.

Neben der Strukturbestimmung eignen sich nieder-energetische Elektronenpulse auch sehr gut zur Untersuchung von Raumladungseffekten: ein intensiver Laserpuls erzeugt über Multiphotonen-Photoemission Photoelektronen vor einer metallischen Oberfläche. Die Erzeugung und zeitliche Entwicklung dieser Elektronenwolke kann über Wechselwirkung mit dem gepulsten Elektronenstrahl untersucht werden, weil die Zeitkonstanten, mit denen sich die Raumladung entwickelt, von der gleichen Grössenordnung sind wie die Pulsdauern unserer Elektronenpulse. Eine detaillierte Untersuchung der Raumladung erlaubte es, deren Effekte auf zeitaufgelöste Elektronenbeugungsexperimente von reinen ultraschnellen Änderungen der Oberflächenstruktur zu trennen.

Dank genauer Untersuchungen der Raumladung vor einer Cu(111)-Fläche haben wir herausgefunden, dass die 55 eV Elektronen des Abfragepulses während der Dauer der Wechselwirkung mit der Raumladung bis zu 60 meV Energie gewinnen und sich gleichzeitig ihr Energiespektrum verschmälert. Wenn die Fluenz des Pumppulses unter einen gewissen Wert gesenkt wird, kann man Raumladungseffekte vernachlässigen. Auf diese Weise können reine Strukturtransienten untersucht werden, gesetzt den Fall die Effekte sind schon bei kleiner Pumpfluenz messbar. Dies ist der Fall des Ordnungs-Unordnungsphasenüberganges, der in Multilagenfilmen von C_{60}-Molekülen auf Ag(111) bei 225 K beobachtet werden kann. Unterhalb dieser Temperatur friert die molekulare Rotationsbewegung ein und bereits die Deposition kleiner Energiemengen durch die Absorption des Pumppulses führt zu signifikanten Effekten. Der Hauptteil der vorliegenden Dissertation widmet sich der erfolgreichen Beobachtung dieses Phasenüberganges in Echtzeit mittels zeitaufgelöster Elektronenbeugung.

Contents

Abstract **i**

Zusammenfassung **ii**

1 Introduction **1**

2 Experimental setup **5**

2.1 Laser system 6

2.2 UHV system 6

2.3 Sample preparation 10

3 Generation of electron pulses **13**

3.1 A new electron gun 14

3.2 Time resolution 15

3.3 Ray tracing simulations 17

3.4 Performance 19

3.4.1 Electron yield 19

3.4.2 Beam profile 20

3.4.3 Energy distribution and space-charge effects 22

3.4.4 Time resolution 24

3.4.5 LEED patterns 25

4 Electron Diffraction **27**

4.1 Introduction to LEED 28

4.2 Debye-Waller theory 30

4.3 Surface Debye temperature 31

4.3.1 Surface Debye temperature of C_{60}/Ag(111) 33

5 Pump-and-probe experiments **37**

5.1 Introduction 37

5.2 Electron-Photon pulse correlator 39

5.3 Coincidence without the pinhole correlator 41

6 Surface space-charge **44**

6.1 Specular beam scattering 45

6.2 Space-charge dynamics 46

6.3 Space-charge model 51

6.4 Pump fluence dependence 54

6.5 Conclusions . . . 56

7 Time-resolved LEED **58**

7.1 Stability of photo-excited C_{60} adsorbed on Ag(111) . . . 59

7.2 C_{60} multilayer on Ag(111) . . . 61

7.3 t-LEED from C_{60} multilayer on Ag(111) . . . 63

8 Conclusions and outlook **67**

Bibliography **69**

List of Acronyms

2PPE	Two Photon Photoemission
BBO	β-Barium Borate crystal
BS	Beamsplitter
CCD	Charge Coupled Device
DW	Debye-Waller
ESCA	Electron Spectroscopy for Chemical Analysis
FWHM	Full Width at Half Maximum
HREELS	High-Resolution Electron Energy-Loss Spectroscopy
LEED	Low Energy Electron Diffraction
t-LEED	time-resolved Low Energy Electron Diffraction
MEED	Medium Energy Electron Diffraction
MCP	Micro-channel plate
ML	Monolayer
RHEED	Reflection High Energy Electron Diffraction
RT	Room Temperature
UHV	Ultra–High Vacuum
UPS	Ultraviolet Photoelectron Spectroscopy
XPS	X–ray Photoelectron Spectroscopy
XPD	X–ray Photoelectron Diffraction

1 Introduction

Over the last several years, the advent and development of ultrafast lasers [1] has opened the possibility to observe *in real time* motions of atoms during chemical and physical changes, like bond forming and breaking or molecular vibrations and rotations. All these dynamics happen on the femto- (fs) to the picosecond (ps) time scale and at the nanometer length scale.

A detailed understanding of such mechanisms requires the observation of atoms or molecules with experiments provided with adequate spatial and temporal resolution. The development of an experimental technique capable of combining a time resolution in the order of $10^{-13} \cdots 10^{-12}\,\mathrm{s}$ [2] with a spatial resolution on atomic scale would allow for studying transient non-equilibrium structures, before, during and after their relaxation towards the equilibrium state.

For long time the direct exploration of these dynamics has been a dream and only refined theories regarding the expected reaction velocities have been developed [3]. In the last decades, the development of short-pulse lasers made possible the realization of experiments with temporal resolution of the order of 1 ps. A completely new research field in physics and chemistry, called *femtochemistry* was opened and one of its fathers, A. H. Zewail, was awarded in 1999 with the Nobel Prize in Chemistry [4].

The basic experimental setup is common to most of the so called *pump-probe* experiments: a femtosecond laser pulse is split into two parts creating thereby two pulses, thus ensuring perfect time synchronization. One pulse ("pump") is used to initiate an ultrafast process while the second pulse ("probe") serves to investigate the transient states of the system in a well-defined moment after the pump pulse. Assembling the results of these probe measurements as function of time delay between pump and probe, one obtains a stroboscopic movie of the system evolution [5–7].

The static structure of molecular assemblies can be mapped out with atomic scale resolution by using electron diffraction and X-ray diffraction. So far X-ray diffraction and high energy electron diffraction have succeeded to be endowed with ultrafast temporal resolution. Time-resolved X-ray diffraction can provide a temporal resolution as low as of some 100 fs [8–11]. But to date this technique suffers from an insufficient signal-to-noise ratio to adequately resolve the atomic details, unless synchrotron or laser-plasma based sources are utilized [12].

However, in synchrotron based experiments the synchronization (jitter) between the pump laser pulse, produced by a femtosecond laser system, and the probe X-ray pulse, generated by the electron bunch in the storage ring, has to be established. This procedure introduces a further limitation for the time resolution: such synchronization is generally achieved within a few picoseconds. Furthermore, X-ray diffraction is not very surface sensitive and the scattering cross section is low.

Quite in contrast the scattering cross section of electrons is several orders of magnitude higher than that of X-rays and electron diffraction is much more surface sensitive than X-rays diffraction [13]. Mainly for this reason short electron pulses are by far the most suitable tool for observing fast structural changes happening on solid surfaces. The knowledge of these dynamics is useful for understanding a series of phenomena like phase transitions [14] or surface reconstructions [15].

In electron diffraction experiments, the need of high sensitivity to the first topmost atomic layers sets constraints for the electron kinetic energy and scattering angles. Therefore two main energy ranges are generally exploited: high kinetic energies, typically ranging from about 10 to 50 keV, where surface sensitivity is achieved by grazing incidence (Reflection High Energy Electron Diffraction, RHEED), and low energies of about 10 to 300 eV (Low Energy Electron Diffraction, LEED), where the scattering angles are large.

So far time-resolved electron diffraction experiments are restricted to electron kinetic energies of the former range for the reason of time resolution: the higher the kinetic energy of the emitted electrons, the narrower is the time spread of the electron pulses [16, 17]. At the moment ultrafast electron crystallography achieves a time resolution even in the sub-picosecond region [14, 18–20].

Going to lower electron energies, as with LEED, bears however the big advantage that the design of the electron gun/optics and detection system is much simpler than with a RHEED gun. Moreover, the sensitivity is with LEED slightly higher than with RHEED due to the larger (elastic) scattering cross section, and the signal-to-background ratio of the diffracted spots better thanks to the higher coherence of the scattered waves.

On the other hand one has to face different drawbacks when dealing with low energy electron pulses, the most important of which are:

1. The achievement of high temporal resolution is particularly difficult. Even using laser pulses as short as a few tenths of femtoseconds, it is hard to convert them in electron pulses narrower than 10 ps. Beside the low electron velocity, a narrow pulse time spread is hampered also by the increased importance of space-charge effects within the single electron pulses [21].

2. It is not trivial to find a system which exhibits a fully *reversible* pump laser excited structural change, which can be resolved with low energy electrons. Indeed for a reversible process, the energy transfer provided by a single pump laser pulse may be so low that the expected signal may be too small to be detected above the background noise.

On the road towards the development of time-resolved LEED (keyword t-LEED) experiments, these two issues have to be taken into account. The main part of this thesis is dealing with our efforts in resolving these two issues, in order to reach the first proof-of-principle for t-LEED experiments.

As a first step, a novel laser activated electron gun, designed to produce electrons pulses with kinetic energy lower than 300 eV, was developed and tested. Particular care was invested in the characterization of this new device and in the determination of the space-charge limit, set by the laser fluence. Beyond this limit the energy spread of the generated electron pulses is significantly increased and the time resolution is compromised. In the best experimental conditions, an upper limit of the electron gun time resolution was measured to be around 35 ps for 65 eV electrons. The latter value was determined utilizing the new electron-photon pulse correlator [22], which has become over the last years our standard tool for cross-correlating light and electron pulses.

As a first experiment, the laser induced vibrations of large molecules on metal surfaces were investigated: the motion of these heavy molecules is expected to be slow enough to be resolved by means of t-LEED. One monolayer of C_{60} molecules deposited on Cu(111) or Ag(111) surfaces is coherently excited by charge-transfer mechanism from the substrate after absorption of the pump laser pulses. One might expect to generate a laser-induced film breathing motion in the direction perpendicular to the surface in the same fashion as H. Park and coauthors have recently observed in aluminum thin films by femtosecond electron diffraction in *transmission* mode [23]. Unfortunately this experiment was not successful probably due to the poor energy coupling between the linearly polarized laser light and the C_{60} monolayer: indeed the reflectivity of silver or copper surfaces for the pump radiation of 800 nm wavelength is close to 98%. This prevents also an appreciable Debye-Waller effect to be detected, since at maximum laser fluence the surface heating would not be larger than a few degrees, even though the surface Debye temperature was measured to be lower than 50 K.

Although no satisfying information about transient surface structure could have been collected investigating the C_{60} monolayer on metals surface system, quite interesting results were obtained about surface space-charge dynamics. The generation and the lifetime of an electron cloud produced by absorption of intense laser pulses on the bare Cu(111) surface, was studied measuring the energy-resolved diffracted electron beam intensity as a function of delay. These measurements were feasible thanks to the novel experimental setup adopted, which includes the installation of a hemispherical electron spectrometer.

Laser induced ultrafast electron pulses have recently attracted some interest due to their potential applications in plasma physics like for instance in the laser confinement fusion field [24, 25]. Even though our experiments are dealing with electron energies smaller by several orders of magnitude, nevertheless a better understanding of the dynamics of such charged particle clouds may contribute to the research in this field.

Pump-probe experiments are considered the key to explore the temporal evolution of phase transitions, since the local atomic motions associated with these phenomena are expected to occur on the picosecond time scale. One of the most promising candidate systems to observe a temperature dependent order-disorder surface phase transition is given by well-ordered C_{60} multilayers deposited on metal surfaces. It is known that solid C_{60} undergoes a *surface* order-disorder phase transition at $T = 225\,\mathrm{K}$, well below the temperature of the corresponding *bulk* phase transition, which is detected at $T = 260\,\mathrm{K}$ [26]. In particular the first phase transition was studied by means of high-resolution electron energy-loss spectroscopy (HREELS), LEED and photoemission and its origin was assigned to the rotation of the molecules around their center: below the critical temperature, the rotation stops and the first-order phase transition occurs [27]. Studying this system by means of a t-LEED experiment, we could observe transient changes in the differential scattering cross section, which in turn reduce the diffracted electron spot intensity. The measured effect most probably is due to the laser induced rotational motion of the C_{60} molecules.

These experiments constitute the first proof-of-principle for time resolved LEED.

It has to be mentioned that the poor experimental time resolution achieved in t-LEED experiments did not permit yet the *direct* observation of coherent molecular motions. However, the study of the transient response of the system upon laser radiation allowed the determination of important parameters, like the time constant which governs the relaxation of the system towards the equilibrium state.

2 Experimental setup

All the experiments reported in this thesis have been performed in an Ultra-High-Vacuum (UHV) system coupled to a femtosecond laser system. Fig. 1 shows a schematic drawing of the experimental setup, which consists of two main parts.

Laser system: the femtosecond (fs) laser system provides ultra-short laser pulses that are used to perform pump-probe experiments. These pulses serve both to excite the sample and to produce short electron pulses at the photocathode of electron gun.

UHV system: the UHV chamber is where the experiment takes place at a base pressure of 5×10^{-11} mbar; besides the surface science ordinary tools for sample preparation and characterization and the laser-activated electron gun, the main components of this system are the electron detectors, which serve to record position and energy of the electrons before or after the diffraction on the sample surface.

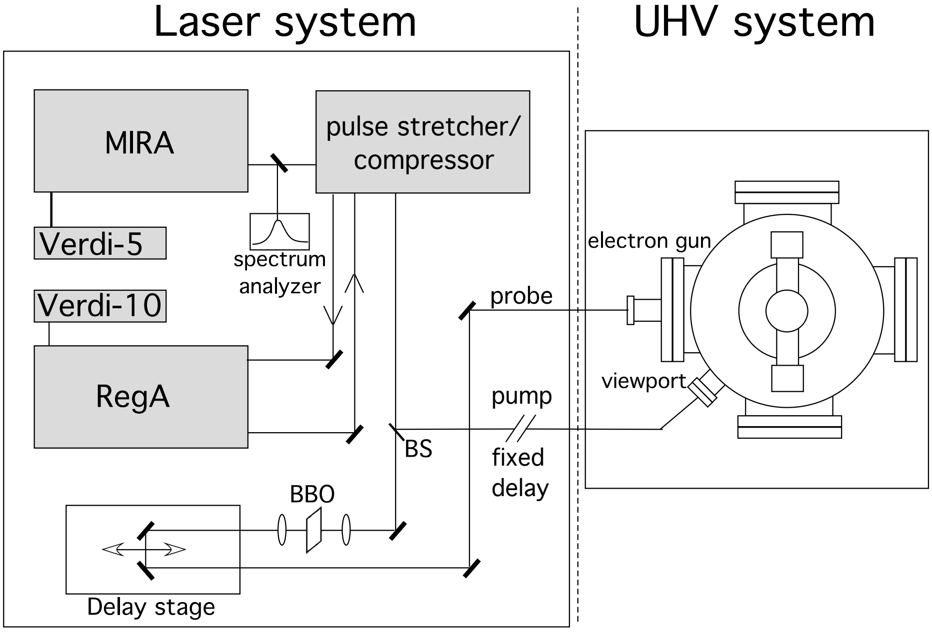

Figure 1: *Schematic drawing of the experimental setup. On the left-hand-side the optical table is sketched with its major components: MIRA oscillator (pumped by a Verdi-5 laser), RegA amplifier (pumped by a Verdi-10 laser), pulse stretcher and compressor, beamsplitter (BS) and mirrors, frequency doubling crystal (BBO) and delay stage. On the right-hand-side the UHV system.*

2.1 Laser system

Our system consists of a commercial Coherent MIRA Ti:sapphire oscillator, pumped by a VERDI−5 W diode-pumped Nd:Vanadate solid state laser (532 nm, continuous wave) [28]. The oscillator emits pulses centered around the central wavelength $\lambda_o = 800\,\mathrm{nm}$ with a spectral-width $\Delta\lambda \sim 28\,\mathrm{nm}$ and a time-width Δt of about 55 fs. The maximum power is roughly 500 mW with a repetition rate of 76 MHz, which translates into a pulse energy of $\sim 6.6\,\mathrm{nJ/pulse}$.

The output pulses can be amplified to higher pulse energies by a chirped-pulse Regenerative Amplifier (Coherent RegA 9050), pumped by a VERDI−10 W (532 nm, continuous wave). The amplification process takes place only if the oscillator pulses are passed through a grating stretcher in order to increase their time-width up to some tenths of picosecond; after the amplification their time duration is of the order of 100 ps and the pulses are compressed back to about 70 fs by a grating compressor, which basically cancels the effects of the stretcher. After the amplification process, the pulse energy is $\sim 5\,\mu\mathrm{J/pulse}$ at a repetition rate of 250 kHz.

Just after the compression, the 800 nm laser light is split into two beams by a beamsplitter (BS in Fig. 1), one of which is focused into a Beta-Barium-Borate (BBO) crystal, where it is frequency doubled. The average power of the 400 nm light is about 10 mW, which translates into 40 nJ/pulse.

The 400 nm beam passes through a delay stage, which can vary its optical path up to 60 cm and is then directed towards the vacuum chamber where it serves to generate electron pulses in the way described in chapter 3.

2.2 UHV system

Besides standard techniques for surface preparation and characterization, our vacuum system is equipped with several tools, which are sensitive to electron position and energy. In particular in the setup used to perform electron diffraction experiments, we can work with three different electron detectors all installed on the same plane as the electron gun:

- a standard LEED detector, which allows one either to map the electron distribution in reciprocal-lattice space and to check the sample surface quality (Auger spectroscopy);
- a resistive-anode position-sensitive detector, which provides the number and spatial distribution of electrons impinging onto its sensitive area;
- an energy analyzer, which permits to measure the electron energy distribution.

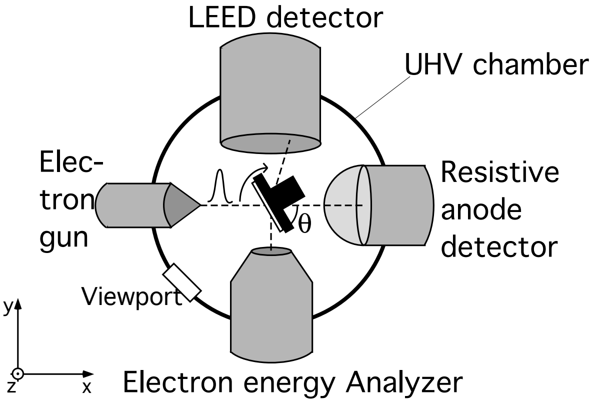

Figure 2: *Schematic drawing of the vacuum chamber (top view); the electrons pulses coming from the laser-activated electron gun fly in a free-field region towards the sample, which is placed in the center of the chamber, and after diffraction are collected either by the LEED detector or the electron energy analyzer. If the sample is removed from the path, the electron beam can be analyzed in the resistive anode detector*

Fig. 2 shows the arrangement of such detectors in the vacuum chamber. The sample is mounted on a manipulator which allows rotations of ±90° in polar angle θ and of 360° in azimuthal angle [29]. Actually the rotation in polar angle is limited to only 60° in one direction to prevent the back of the manipulator to crash against the entrance of the energy analyzer. Furthermore the manipulator is equipped with a xyz-translator which permits movements up to 25 mm in the x and y directions and up to 50 mm along z (coordinate perpendicular to the detector plane).

The sample can be cooled down to 80 K by means of a liquid Helium flow and to 180 K with liquid nitrogen.

The UHV system is also equipped with the standard tools for surface science, like Ar-ion sputter gun and C_{60} evaporator for sample preparation and a twin anode X-ray source (Mg $K\alpha$ and Si $K\alpha$) for sample quality characterization.

The pump laser light can be sent towards the sample through the viewport located at 45° between the electron gun and the analyzer.

LEED detector. The detector is a commercial 4-grid hemispherical retarding field analyzer with back display optics and a coaxially mounted electron gun [30]. It is also equipped with two micro-channel plates (MCP) for amplification and has been proved that it is able to count single electrons [17]. The total acceptance angle of the detector is 75°.

Electrons coming from two sources can be diffracted towards the phosphorous screen of this detector. Fig. 3 shows typical data acquired either with the integrated filament gun or the laser activated gun. When the former is used, limitations in the sample rotation do not allow to record normal incidence LEED patterns (Fig. 3a), while when the latter is at work, it is possible to image the specular beam onto the phosphorous screen

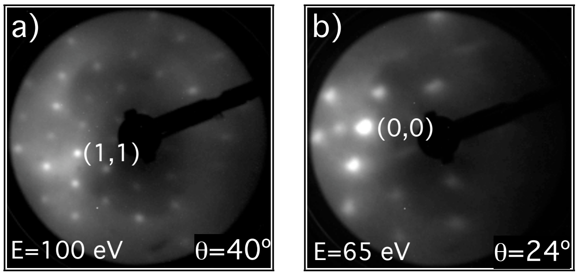

Figure 3: *LEED patterns of a C_{60} monolayer on Cu(111) collected with the two electron sources. a) At* 100 eV *and* $\theta = 40°$ *with the integrated filament gun. b) At* 65 eV *and* $\theta = 24°$ *with the laser activated gun: the (0,0) spot is imaged onto the phosphorous screen of this detector.*

(Fig. 3b): in particular for angles of incidence θ close to 45°, normal incidence LEED patterns can be recorded.

Resistive-anode position-sensitive detector. We have at our disposal a commercial position-sensitive detector system from Spectroscopy Instruments GmbH [31]. Detectors of this kind allow the detection of individual charged particles, like electrons; since the location of each event is precisely determined, images in the detection plane can be reconstructed.

The system is made up of two basic components, a sensor assembly and a position computing electronics package. The first consists of two MCP electron multipliers and a resistive anode encoder; the second consists of preamplifiers and computing circuits which process the data from the resistive anode encoder and provide the x and y coordinate of each detected electron. The resistive-anode system works on a charge division principle: when an electron strikes the input of the electron multiplier, a pulse of $\sim 10^6$ electrons is produced; this charge is collected by 4 electrodes on the resistive anode. The (x, y) position of the electron is computed from the charge division among the electrodes.

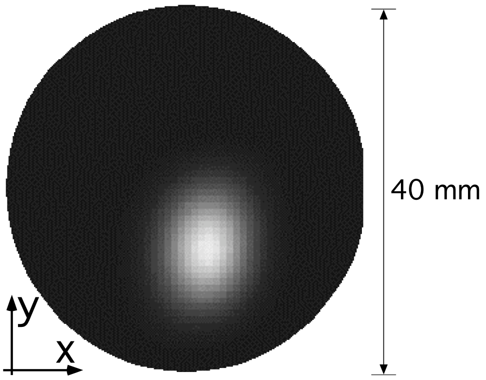

Figure 4: 100 eV *electron energy beam picture recorded by the resistive anode position sensitive detector (exposure time 10 seconds). The integral of the spot results in an electron yield of about 1 electron per laser pulse, while line profiles give beam dimensions of* $\sim$ 5×8 mm *at the entrance of the detector MCPs.*

The main application of such detector is to give quantitative information about the pulsed electron beam produced at the cathode of the laser-activated electron gun. The detector sensor active area is a circle, with a diameter of 40 mm. Fig. 4 shows a 100 eV electron energy beam picture recorded with the detector. The integration of the spot intensity results into a value for the total electron yield of the beam, while by line profile analysis the beam size can be estimated.

In particular for the picture of Fig. 4 a beam current of about 1 electron per 800 nm laser pulse and a beam size of 5 × 8 mm are obtained. The latter is the electron beam size determined at the entrance of the detector MCPs, which is located about 14 cm away from the electron gun cathode; thus the angular beam divergence is 1° and 1.5° (see section 3.4.2 for details).

Electron energy analyzer. The UHV chamber is equipped with a CLAM2 electron energy analyzer [32]. This detector is a 100 mm mean radius hemispherical electron spectrometer and is equipped with an integral dual element transfer lens and a single channel electron multiplier.

The defining slit dimensions can be varied between 1 mm, 2 mm diameter (circular shape) or 2 mm, 4 mm (square shape). Most of the experiments reported in this thesis have been performed with the maximum aperture, using a pass energy value of 50 eV in order to increase the count rate of the analyzed electrons. Although this approach worsens the energy and angular resolution of the instruments, it becomes necessary since we are deal-

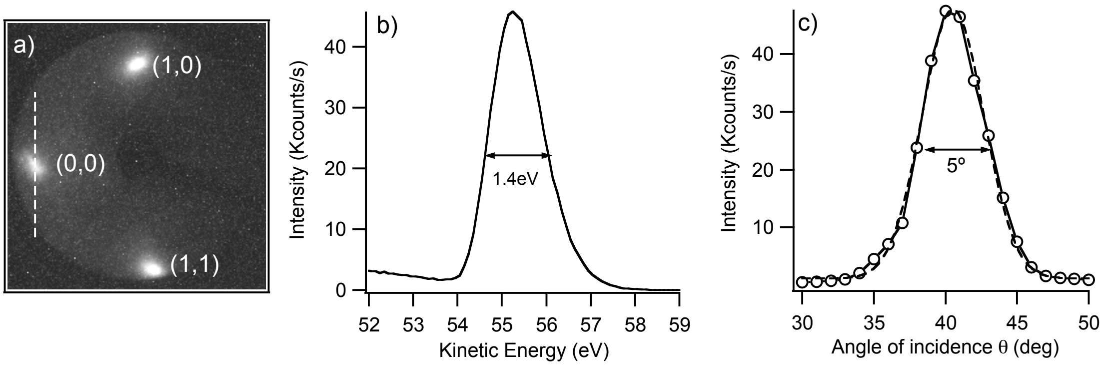

Figure 5: *a) Electron diffraction pattern of Cu(111) surface recorded with the LEED detector with* 120 eV *electron pulses produced using* 2 nJ/*pulse laser pulses (*10 s *exposure time). b) Energy spectrum of the specular spot measured with the electron energy analyzer for* 55 eV *electrons from a Cu(111) sample; a Gaussian yields a width of* $\Delta E = 1.4\,\mathrm{eV}$ *FWHM. c) Polar scan of the Cu(111) specular spot in the peak maximum at* $E = 55.25\,\mathrm{eV}$*; the angular width is* 5° *FWHM, in good agreement with the value* 5.5° *measured by a line profile of the LEED pattern in a).*

ing with pulsed electron beams of the order of few tenths of femtoamperes.

As depicted in Fig. 2, by rotating the sample about the polar and the azimuthal axis it is possible to direct one of the diffracted spots into the entrance slit of the electron spectrometer. In view of a time-resolved experiment the implementation of an electron energy analyzer may give several advantages: among those a faster data acquisition and a better time resolution, due to the capability of energy-resolving the diffracted electrons. In particular the latter functionality allows for the measurement of transient energy shifts of the diffracted electrons, which would not be observable with the standard LEED detector.

Fig. 5 shows an analysis of the specular spot of Cu(111). The parameters of the laser activated electron gun are optimized by checking the diffraction pattern (Fig. 5a) recorded with the LEED detector. Then the manipulator is rotated around the vertical axis by about 90°, so that the desired diffracted beam is directed into the entrance of the electron energy analyzer. With this detector, measurements of the energy and angular width of the diffraction spots as shown in Fig. 5b and Fig. 5c for the specular spot, are possible.

2.3 Sample preparation

For the experiments presented in this thesis Cu(111) and Ag(111) were used as metal substrates onto which a monolayer or multilayers of C_{60} where deposited.

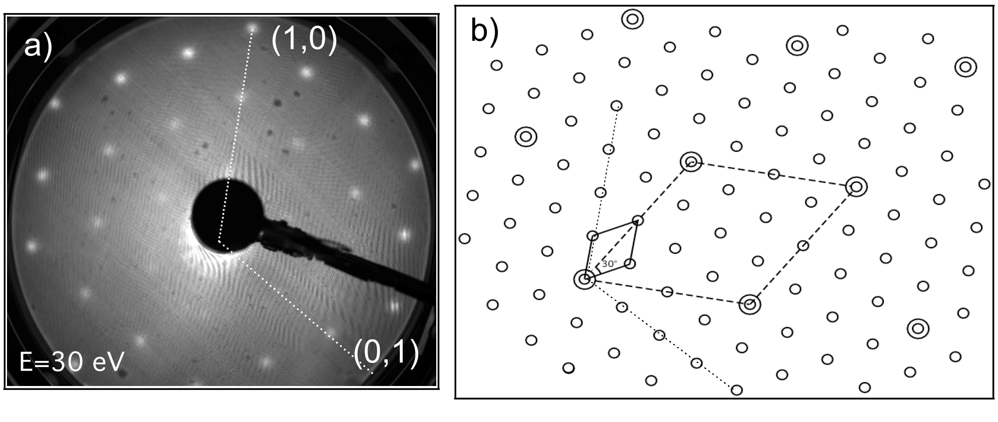

Figure 6: *a) LEED pattern of one C_{60} monolayer on Ag(111), recorded at* 30 eV *electron energy. b) Schematic view of the real space structure; the full and the dashed line describes the unit cell of the substrate and of the overlayer, respectively. In a) and b) the direction of the reciprocal space lattice vectors are drawn as dotted lines.*

The copper and silver surfaces were prepared by standard sputter/anneal cycles, with maximum temperatures reached up to $\sim$ 950 K. Surface order and cleanliness were checked by LEED and by X-ray Photoelectron Spectroscopy (XPS) measurements, respectively.

C_{60} powder (99.9% purity) was evaporated by sublimation from a titanium crucible heated to 620 K, at a substrate temperature close to 400 K. With this procedure an ordered C_{60} multilayer can be grown on the metal surface; subsequent annealing of the sample to 600 K results in the desorption of all the layers, except the first, which is stronger bound to the surface [33]. Thereby a well prepared monolayer structure is achieved. It has been demonstrated that the low evaporation rate ($\sim$ 2.5 ML/h) and the sample temperature are important parameters in order to get well ordered structures [34,35].

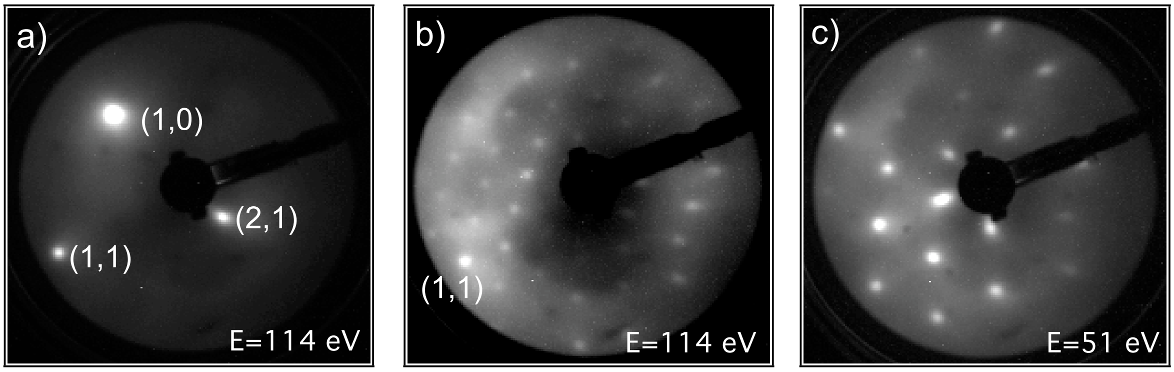

Figure 7: *Room temperature LEED patterns for a) clean Cu(111) and b) one monolayer of C_{60}/Cu(111) at* 114 eV *electron energy. c) One monolayer of C_{60}/Cu(111) at $E = 51\,\mathrm{eV}$, the pattern corresponds to an ordered 4×4 structure. For all the three pictures, the angle of incidence is* 37° *referred to the sample normal.*

One monolayer of C_{60} forms different structures on Ag(111) and Cu(111): on Ag(111) surface deposition of more than one monolayer of C_{60} forms a commensurate hexagonal $(2\sqrt{3} \times 2\sqrt{3})R30°$ structure [36,37], and some additional structures rotated by 14 degree and 46° [38], with the latter two disappearing after the annealing, when only one monolayer remains. Fig. 6a shows a normal incidence LEED pattern of the $(2\sqrt{3} \times 2\sqrt{3})R30°$ structure, recorded with 30 eV electron energy; this picture was collected in a UHV chamber different from that described in section 2.2, where it is possible to measure normal incidence diffraction patterns. The reciprocal lattice vectors are drawn as dotted lines. In Fig. 6b the real space structure is shown: the overlayer unit cell is 12 times larger than the one of the substrate and it is rotated by 30°.

On Cu(111) the surface lattice constant is equal to 2.55 Å, while the nearest neighbor distance in bulk C_{60} is 10.0 Å [39]; thus the lattice mismatch between the latter and four times the distance Cu-Cu atom is only 2%, suggesting a commensurate 4×4 growth of C_{60} on this surface. Indeed the monolayer system LEED patterns shown in Fig. 7 confirm this view. In Fig. 7 diffraction patterns at the same electron energy (114 eV) and azimuthal angle are shown for clean Cu(111) and one monolayer of C_{60}/Cu(111). The angle of incidence is 37° with respect to the sample normal.

3 Generation of electron pulses

In the setup of a time resolved LEED experiment a pulsed electron beam is used as a *probe* and a pulsed laser beam is used as a *pump*.

A typical setup of a laser-pump and electron-probe experiment is sketched in Fig. 8.

A short laser pulse is divided in two branches by a beamsplitter. One branch, the *pump pulse* is directly sent towards the sample where it drives the sample in an excited state; the second branch is focused from behind onto the cathode of the electron gun, where an electron pulse is produced via two-photon photoemission (2PPE). This electron pulse, the *probe pulse* is accelerated and, eventually, focused onto the sample. The time delay between the two pulses is well defined and depends only on the path lengths of the two light pulses and the flight time of the electrons in the pulse. This delay can be varied by moving a delay stage, thus changing the path length of one of the two branches with respect to the other.

The key point of such an experiment resides in the conversion of the laser pulses into electron pulses and in the propagation of such pulses towards the sample position. Indeed while the light-pump pulses can be as narrow as few tenths of femtoseconds, the electron-probe pulses are generally much wider in time when they probe the sample surface and eventually define the time resolution of the experiment.

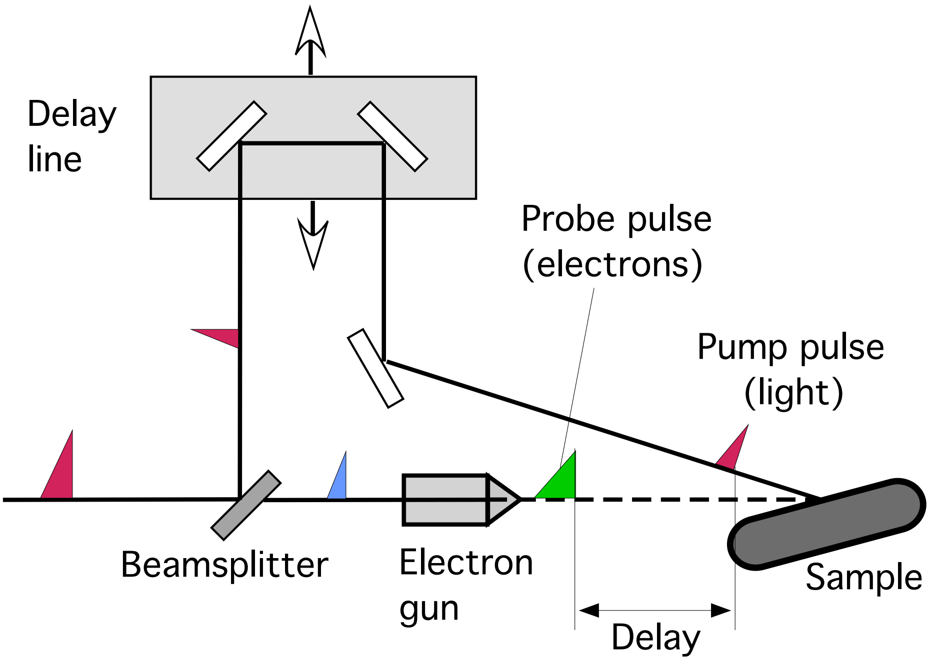

Figure 8: *Typical setup of a light-pump electron-probe experiment.*

Since the electron pulses get broader while propagating, it is realistic to consider an intrinsic time width Δt in the range of 1% of the total flight time.

3.1 A new electron gun

Any design of a pulsed laser activated electron gun has to deal with the problem of fulfilling the following requirements at the sample position:

- The time spread of the electron pulse has to be as narrow as possible, in order to keep the time resolution the smallest.
- The electron beam has to be energetically monochromatic.
- The electron beam has to be collimated and with a small spotsize. In particular, to perform pump-probe experiments, the latter should be kept smaller than the pump laser spotsize; in this way all the electrons in the beam can probe the pump-excited sample region.

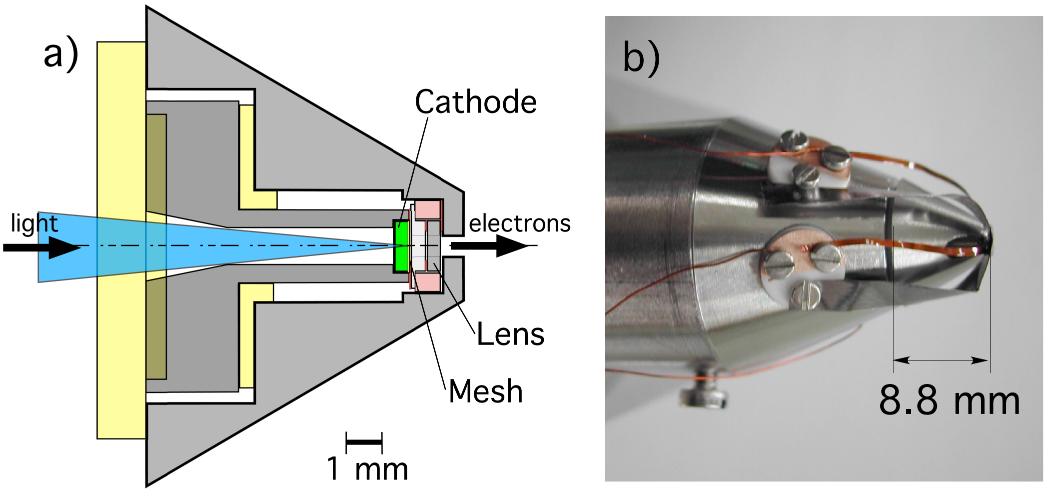

Figure 9: *a) Sketch of the new electron gun head. In the topmost part a* 5 µm *thick gold mesh acting as anode and an electrostatic lens find place. b) Photo of the gun head; the Cu covered Kapton wires used to charge the anode and the lens are visible as well as a thin metal stripe used to shield the field from the wires and ensure a free field region.*

In a former design of a pulsed LEED gun [40], the collimation of the electron beam was achieved shooting the electrons through an 800 µm long grounded micro channel plate

(MCP), positioned just after the cathode. This improved coherence of the electrons was paid by a transmission as low as 10^{-5} [17].

Therefore a new gun was designed and realized in our workshop with a (i) a maximum transmission without loss of beam collimation and time resolution and (ii) a smaller solid angle that shadows a detector and the incoming light pulses (60° full cone).

In Fig. 9 a drawing of the actual design is shown together with a photograph of the top part of the gun.

The photocathode consists of a thin atomically flat gold film (20 nm thick) grown on a 400 μm thick sapphire substrate. The electrons produced by 400 nm laser pulses are accelerated over a short distance (only 50 μm) towards a grounded gold mesh (5 μm thick, 44% geometrical transmission), acting as anode. An additional 300 μm thick electrostatic lens is placed after the anode in order to focus the electrons towards the sample. The typical distance cathode-sample is in the order of few millimeters and a shield electrode ensures a field-free region for the electrons outside the head of the gun.

The cathode is charged via a wire contact from the back, while the anode and the electrostatic lens are charged via Kapton isolated wires, 25 μm thick and 20 mm long, covered with copper on one side. The isolation of all the charged metal components with respect to ground is ensured using a 350 μm thick sapphire tube and Kapton isolated discs.

3.2 Time resolution

One of the main constraints in the generation of electron pulses is the necessity to keep the pulse duration (i.e. time resolution) as short as possible. Indeed in order to watch events happening on the molecular level, such as vibrations and rotations of adsorbates, it is necessary to have at disposal a device with picosecond time resolution.

In general, two terms contribute to the time spread Δt of an electron pulse:

1. In the *acceleration region* between the cathode and the anode, the pulse time dispersion Δt_{acc} is directly proportional to the cathode-anode distance and inversely proportional to the electron kinetic energy.

2. In the field free *drift region* between the anode and the sample, the time spread Δt_{drift} depends on the electrons path length difference and the total time of flight.

The equation can be written as follows [22]:

$$\Delta t = \Delta t_{acc} + \Delta t_{drift} = \frac{\Delta E_0 \sqrt{m_e}}{2eU\sqrt{2E_0}} d_{acc} + \Big(\frac{\Delta E_0}{2eU} + \frac{\Delta s}{s}\Big) t_{flight} \tag{1}$$

where m_e is the electron mass, E_0 is the initial electron energy at the photocathode, ΔE_0 is the width of the energy distribution, eU the electron kinetic energy, d_{acc} the cathode-anode distance, s the total electron path length, Δs the electron path length difference and t_{flight} the total time of flight.

The field free region contribution to the time dispersion is generally dominating compared with the acceleration region contribution. As shown in Table 1 for different beam primary energy, the latter is contributing only to a few percent of the total time spread. The values reported in Table 1 are calculated using Eq. (1) assuming a cathode-sample distance of 5 mm, a path length difference calculated by an angular beam divergency of about 2°, an initial electron energy $E_0 = 0.5\,\text{eV}$ with an energy width limited to 1 eV. As it will be shown in the next sections these values are quite realistic and correspond to the actual measured performances.

Table 1: *Pulse time dispersion in the acceleration region (Δt_{acc}) and in the field free region (Δt_{drift}) calculated with Eq. (1) for different primary energies.*

Energy (eV)	Flight time (ns)	Δt_{acc} (ps)	$\Delta t_{drift}(ps)$	Δt (ps)
10	2.4	6	100	106
50	1.1	1.2	12.1	13.3
100	0.79	0.6	5.1	5.7
150	0.66	0.4	3.2	3.6
200	0.56	0.3	2.1	2.4

It can immediately be seen that in order to minimize Δt either the electron energy (i.e. velocity) should be large, or the total time of flight (i.e. path length) should be small. Due to the small electron energies the LEED gun had to be designed for small distances; when constructing the new gun this requirement together with the constraint of keeping d_{acc} small has been met.

Electron energy distribution The width of the electron energy distribution ΔE_0 is given by $2h\nu - \Phi$, where Φ denotes the work function of the cathode material. Thus the choice of a suitable photocatode material is very important: it is desirable to choose a material providing a work function Φ as close as possible to the laser energy $2h\nu$. Gold fits this requirement with the further advantage to be chemically inert in ultrahigh vacuum. Since the work function of gold for photoelectric effect is 5.1 eV with two photons

of 3.1 eV we would expect an energy width of about 1 eV.
Together with the acceleration distance of 50 µm this results in a nominal Δt_{acc} of about 1.5 ps for 100 eV electrons.

Electron path length difference The quantity Δs represents the path length difference of each electron in the pulse; from Eq. (1) it follows that it is desirable to have the smallest path difference possible in order to keep the temporal spread small: ideally, all the electrons of a pulse should reach the target after traveling the same path length.
On the other hand, an additional requirement is to have a parallel and collimated electron beam at the sample position, thus some focusing or collimating procedure is required.
From Eq. (1) it is trivial to calculate that if the electron path difference Δs is kept smaller than 0.5% of the total path length s equal to 5 mm, then Δt_{drift} takes a value slightly smaller than 5 ps if the electron energy distribution is limited to 1 eV. Thus considering also the small contribution given by the acceleration region, the total time spread Δt results to be slightly larger than 5 ps, for 100 eV electrons.
In the present design the collimation of the beam is performed with a 300 µm thick electrostatic lens, which bends the trajectories of the electrons traveling off axis towards the center. Indeed these electrons take a longer time to arrive at the focal point than electrons traveling along the axis, but as explained in section 3.3 it is possible to keep the time spread derived only from the path difference below 5 ps despite the use of the lens.

3.3 Ray tracing simulations

Extended ray tracing simulations have been performed in order to estimate the nominal time resolution of the new high flux electron gun [41]. In these simulations, the electrons leave the cathode with a uniform space distribution, a 0.5 eV wide energy Gaussian distribution centered at 0.5 eV and an angular cosine distribution [42]. The time of flight of the electrons and their position with respect to the central axis are recorded at the sample position located 4 mm from the cathode. A histogram plot reveals that the electrons are arranged in position and time following a Gaussian distribution, whose Full Width at Half Maximum (FWHM) gives a good estimation of the time spread Δt and the electron beam width.
A plot of these quantities as a function of the voltage applied to the electrostatic lens permits to deduce at a certain cathode voltage the best value of lens voltage by which either an appreciable focusing effect (small beam width) and a sufficient small time spread

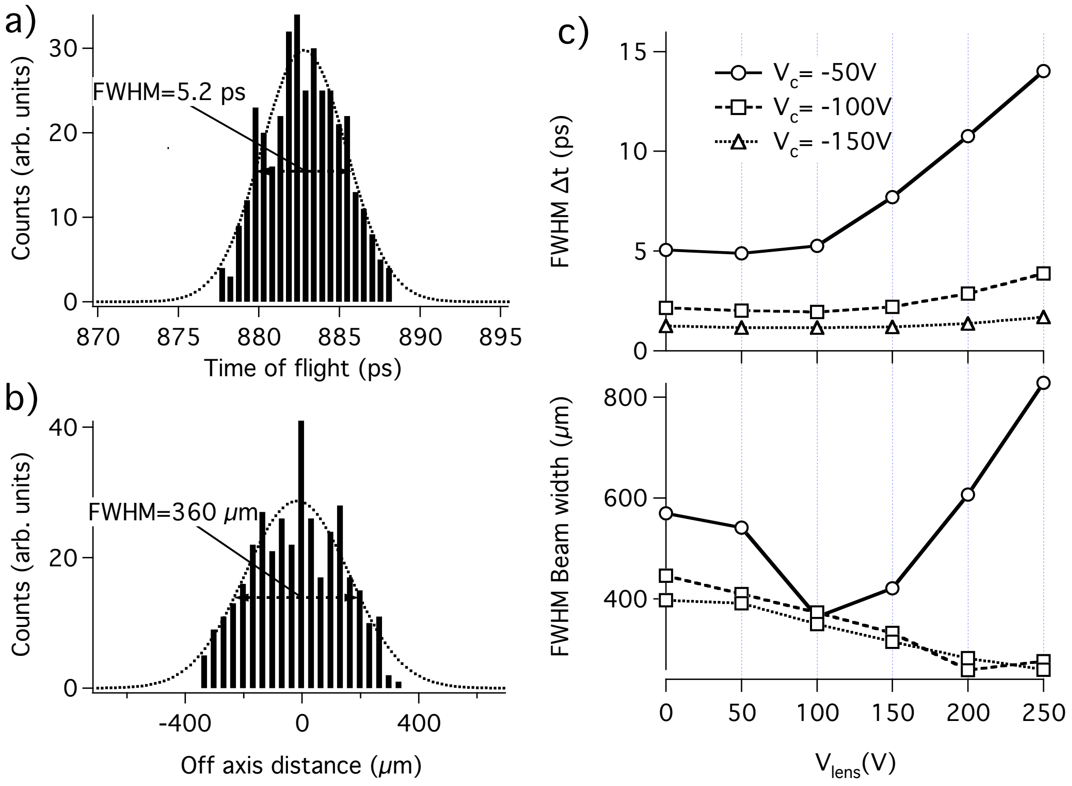

Figure 10: *a) Electrons distribution as a function of time and b) Electron distribution along the axis perpendicular to the direction of flight. Both distributions were obtained assuming a cathode voltage* $V_c = -50\,\mathrm{V}$*, a lens voltage* $V_{lens} = +100\,\mathrm{V}$ *and can be fitted with a Gaussian profile. c) Plot of electrons time spread* Δt *and beam width deduced from the Gaussian fit as a function of* V_{lens} *for three different values* V_c*.*

is achieved.

In Fig. 10 the results of this analysis are reported for three different values of cathode voltage. As predicted by Eq. (1) the effect of the lens electric field and thus the time resolution of the electron pulse get worse the slower the electrons are.

The focusing effect of the lens is clearly visible in the bottom part of Fig. 10c: for 50 V accelerating voltage, the minimum beam size is reached when the lens voltage is about 100 V. For higher voltages the trajectories of the electrons are so bended and the path difference so large that either the time spread and the spotsize gets worse. For faster electrons, the effect of the electrostatic lens becomes less important and the time resolution is always below $2-3\,\mathrm{ps}$ while the spotsize can be reduced by roughly 25% compared to the zero field situation.

All these simulations were performed at normal incidence, without taking into account additional path length difference due to tilt of the sample.

3.4 Performance

In order to test the performance of the new gun, first the shape and the size of the electron beam, the electron yield and the energy distribution were measured at a cathode voltage of $-100\,\mathrm{V}$, using a position-sensitive resistive-anode detector with a retarding grid and a hemispherical sector electron energy analyzer (VG CLAM2).

The second step was to perform diffraction experiment using a commercial microchannel LEED detector. Using the first design of the electron gun, the diffracted beams had to be integrated over several minutes, because of the fairly low electron beam current. The main goal of the new design is to ensure a good signal-to-background ratio in a reasonable integrating time. In our setup, spherical four grid optics are used, followed by two MCP mounted in chevron configuration. The MCP amplified current is visualized on a planar fluorescent screen, and the light spots are recorded by a Peltier-cooled Charge-Coupled-Device (CCD) camera.

3.4.1 Electron yield

First the total electron yield of the new gun was determined measuring the current deposited onto a metal plate placed at the sample position. This test was performed in a separate UHV chamber, as the detection of currents in the order of few picoamperes results impossible in the main chamber. In this experiment a maximum value of 12.2 pA was measured with full blue light power (around 1 nJ/pulse) at a repetition rate of 80 MHz. This results in 0.95 electrons/pulse.

When the electron gun was mounted on a flange of the main UHV chamber, a direct measurement of the electron yield is feasible using the resistive-anode detector placed in front of the head of the gun. With a repetition rate now of 250 kHz, we can exploit higher laser powers, but we also deal with cathode space-charge onset which decreases the photoemission efficiency (see section 3.4.3). When pulses excited with 1 nJ energy hit the cathode, 235 thousands electrons per second are counted in the detector, resulting in 0.94 electrons/pulse.

This result shows that the space-charge effect sets an intrinsic limit for the total electron yield: it is not sufficient to increase the pulse energy of the 400 nm laser light to have a more intense beam, since the efficiency of the photon-to-electron conversion process decreases. Nevertheless the regenerative amplifier operating at 250 kHz repetition rate will be used for most of the experiments reported in this thesis, since it permits to gain

almost three order of magnitude in *pump* (800 nm wavelength) laser fluences, which are necessary to enhance a transient effects on the sample surface.
Combining the two methods described above we can conclude that the electron yield of the new high flux electron gun is roughly 1 electron/pulse when the cathode is illuminated with 1 nJ/pulse pulses. In comparison with the first gun design which provides 1.4×10^{-4} electrons per 1.2 nJ/pulse pulses [17], we gain almost four orders of magnitude in terms of total electrons produced.

3.4.2 Beam profile

The shape of the electron beam was determined using the resistive-anode detector placed at a distance of about 14 cm from the head of the gun. In this way, pictures of the electron spot can be recorded and the angular beam divergence can be estimated from the size of the spot. Moreover, varying the voltage applied to the electrostatic lens the effective capability of focusing the beam can be measured and compared with the simulations.

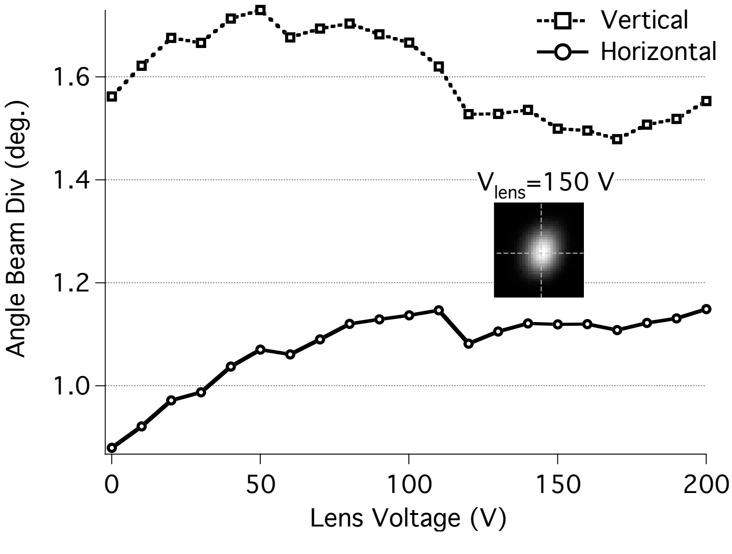

Figure 11: *Measurement of the beam divergence angle performed with a position-sensitive detector located* 14 cm *away from the gun head. In the inset the picture recorded at a lens voltage of* 150 V *is displayed.*

Fig. 11 shows the results of this experiment: the width of the beam was measured along the vertical and horizontal axis by cutting with a line profile the beam images. The electron beam clearly presents an elliptical shape being the horizontal and vertical axis roughly 0.5 mm and 0.7 mm respectively. This translates into an angular divergence of about 1° and 1.5°.

Quite surprisingly, the collimating effect of the electrostatic lens results to be pretty weak over the range of more than 200 V. Indeed both the shape and the dimension of the beam remain almost constant over this range, but looking more carefully it seems that the collimation is more effective along the vertical direction.

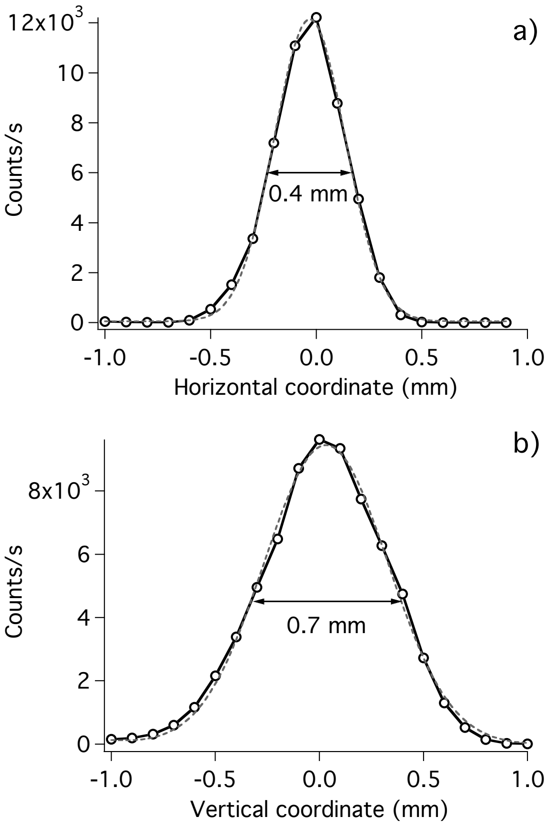

Figure 12: *Beam profiles as collected moving a pinhole of diameter* 0.5 mm *across the beam. a) horizontal coordinate, the measured FWHM is* 0.4 mm*; b) vertical coordinate, FWHM is* 0.7 mm*.*

The observation that the lens effect is different for the two directions together with the observed elliptical spot shape suggest a possible misalignment of some element, like the lens itself, inside the head of the gun.

The previous setup allows the direct observation of the spot and the optimization of those parameters which are crucial for the generation of the electron pulses. Among these, the distance of the lens, which focuses the blue laser light onto the photocathode, and the alignment of the laser beam so that the center of the cathode is hit.

On the other hand this design provides no information about the spotsize at the place of interaction, i.e. at the sample position. In order to do that, the electron beam has been scanned using an aluminum plate in the middle of which a 0.5 mm diameter pinhole was drilled.

The results of this experiment are shown in Fig. 12 and was realized as follows: the plate is placed at the sample position and moved along the two directions orthogonal to the beam, so that the beam can pass through the pinhole. Then the plate is moved across the beam, while recording the number of electrons reaching the detector placed behind.

3.4.3 Energy distribution and space-charge effects

Shooting the electron beam into the entrance of the electron energy analyzer allows the measurement of the energy spectrum. With a measurement of this kind, we can derive an estimation of the time resolution of the electron gun, using Eq. (1).
Actually the electron energy analyzer is mounted on the chamber on a flange located at 90° with respect to the the laser activated electron gun. A metal plate charged at a voltage higher than the cathode voltage is placed at $\sim 45°$, acting as an electrostatic mirror to direct the electron beam towards the analyzer aperture.

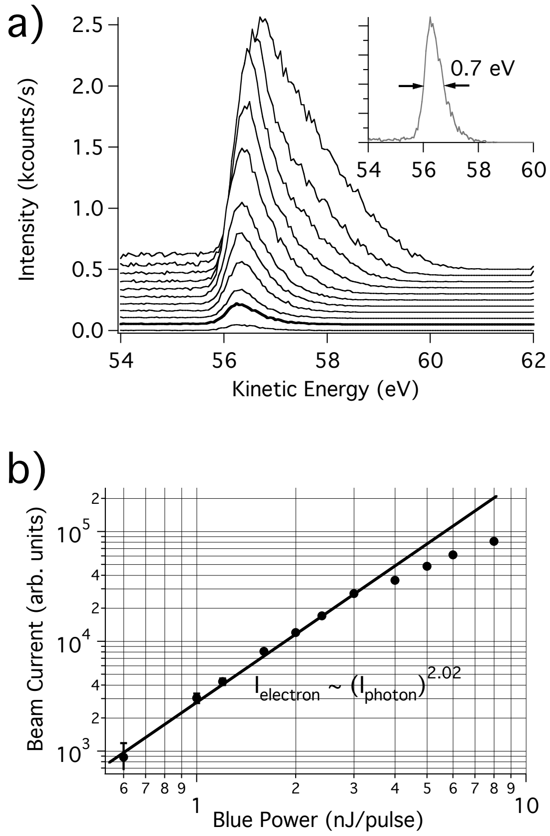

Figure 13: *a) Spectra of photoelectrons measured at cathode voltage of* −55 V *while increasing the blue laser power from* 0.6 nJ*/pulse up to* 8 nJ*/pulse; in the inset the spectrum for* 1 nJ*/pulse power is shown. b) Beam current as a function of blue laser power: for powers higher than* 3 nJ*/pulse, a decreasing efficiency of photoemission effect takes place, as indicated by the deviation from the second order process line (note the logarithmic scales).*

Fig. 13 shows several spectra of the electrons coming from the cathode kept at a voltage of −55 V for increasing power of the 400 nm pulsed laser light (blue light) at 250 kHz repetition rate. The integral of the energy spectrum has the same units as a beam current, even though the absolute number is almost two orders of magnitude lower than the electron yield measured in 3.4.1; this is probably due to the fact that not the full electron beam is collected into the analyzer aperture.

When a two-photon photoemission process is involved as in this case, we would expect to see the area of the peak increasing with increasing laser power following a power law with exponent as close as possible to the value of 2. This is actually the case at least up to a certain laser power; beyond this limit the total number of electrons reaching the sample position is reduced (Fig. 13b). This effect is caused by the onset of a space-charge effect: when too many electrons are emitted within a very short time, typically 100 fs, they interact with each other via Coulomb repulsion, while they are slowly accelerated towards the anode.

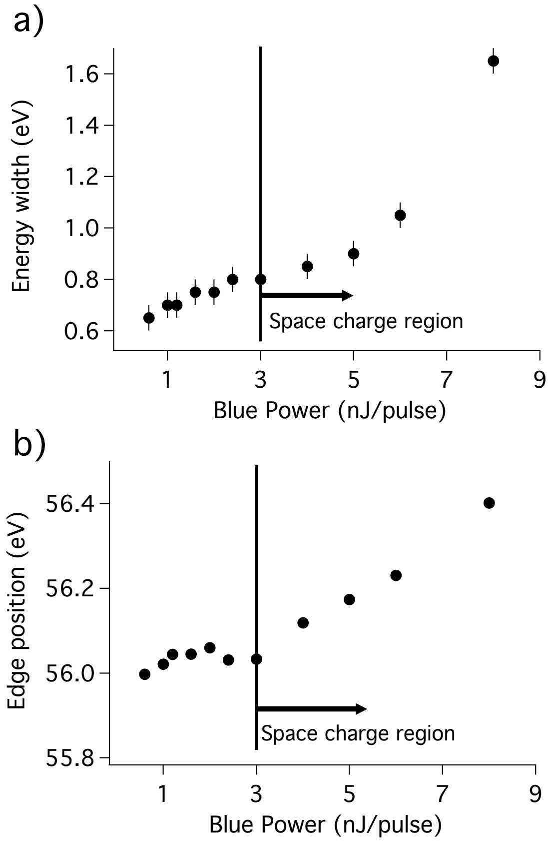

Figure 14: *Spectral energy width (a) and leading edge position (b) as a function of laser light power for* 55 eV *electrons: above the space-charge limit estimated in Fig. 13, the spectra become wider and their edge shifts towards higher kinetic energy.*

This repulsion between electrons within a pulse leads to a swelling of the pulse in all spatial directions, implying a lengthening of the pulse duration. In an energy resolved measurement, the space-charge effect causes a progressive broadening and increasing asymmetry of the peak with increasing power. Looking at Fig. 13 we can set the threshold for the space-charge onset at a laser power of about 3 nJ/pulse; above this limit the

spectra become considerably wider in energy and consequently also in time.
As shown in Fig. 14a the width of energy spectrum increases almost linearly with the increasing laser power; still at the space-charge limit the measured FWHM is as low as 0.8 eV. For laser powers larger than 5 nJ/pulse the width starts to exceed 1 eV. Plugging in this value for the energy spread into Eq. (1) results in a nominal time resolution lower than 10 ps even for so slow electrons.
In Fig. 14b the energy position of the peak leading edge is shown as a function of the laser power focused onto the cathode. We do not observe any significant energy shift up to the value of 3 nJ/pulse, which we assign to be the space-charge limit. After this threshold the leading edge moves almost linearly towards higher kinetic energies, with a maximum measured shift of about 400 meV.

3.4.4 Time resolution

An upper limit for the effective electron gun temporal resolution may be deduced by measuring a photon-pump electron-probe correlation curve: the details of this pump-probe experiment are described in section 5.2 and reference [22].

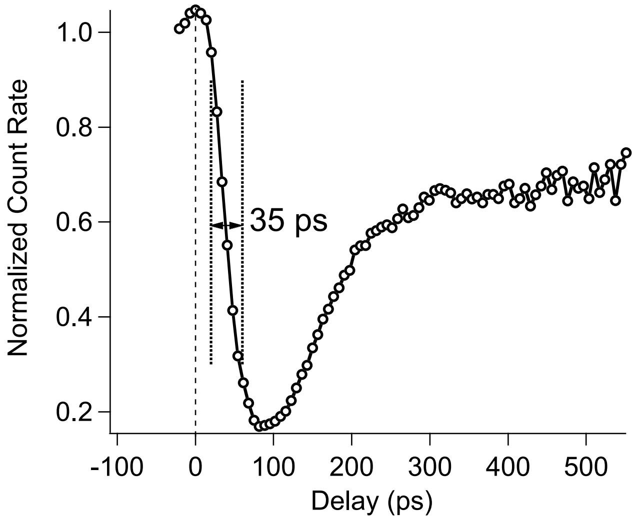

Figure 15: *Shortest feature ever observed with the new electron gun. The "drop time"* $\Delta t = 35\,\mathrm{ps}$ *may be considered as an upper limit of the electron gun time resolution. This curve was obtained with* 55 eV *electron pulses.*

Here the fastest event ever observed is reported in Fig. 15: the time interval Δt over which the normalized intensity drops from 90% to 10% of its maximum step height can be considered as an upper limit of the electron pulses temporal width, which eventually defines the time resolution.
The curve shown in Fig. 15 was measured with 55 eV electron pulses at a cathode-sample distance of about 10 mm and results in a value of $\Delta t \leqslant 35\,\mathrm{ps}$, in good agreement with

the estimation of 28 ps given by Eq. (1). It has to be noted that cathode space-charge effects should not induce further broadening to the observed temporal width, since the laser light power was set to 2 nJ/pulse, below the cathode space-charge limit determined in section 3.4.3.

3.4.5 LEED patterns

The most important proof to test the performances of the new gun was the collection of LEED pictures from single crystal samples. The cathode-sample distance was limited to 6 mm in order to ensure the minimum time spread of the electron pulses, as the latter increases with increasing the total electron time of flight (see 3.2). The first LEED patterns were obtained in a geometry close to specular reflection.

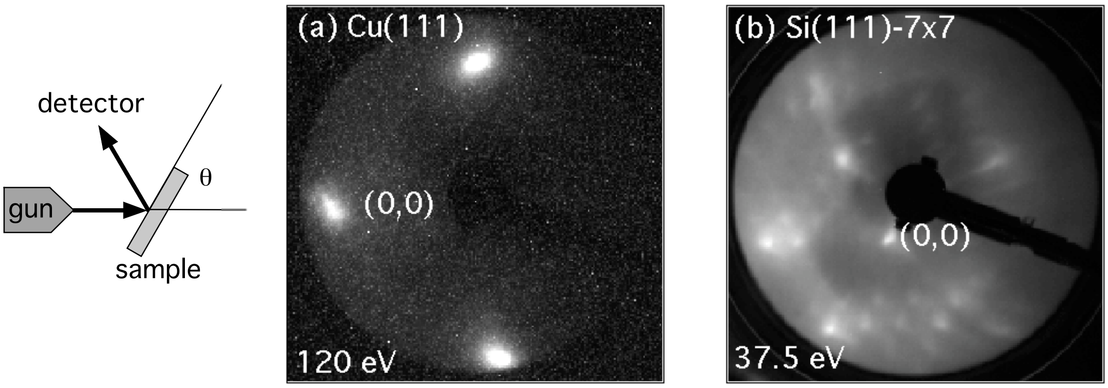

Figure 16: *LEED patterns collected with the laser activated electron gun for (a) clean Cu(111) (electron energy=*120 eV*),* 10 s *exposure time; (b) clean Si(111)-7×7 (electron energy=*37.5 eV*,* 20 s *exposure time. On the left the scattering geometry is sketched, being the angle θ equal to* 58° *for (a) and* 49° *for (b) respectively. The position of the specular beam is indicated in the pictures as reference.*

Fig. 16 shows two representative LEED images from two different samples, namely Cu(111) and Si(111)-7×7. For both images the exposure time was limited to 10 seconds only, while the laser power was 2 nJ/pulse and 8 nJ/pulse for (a) and (b), respectively. The images are comparable to LEED pictures obtained using conventional electron guns with thermally activated cathode. In particular the Si(111)-7×7 reconstruction pattern shows that we are able to resolve diffraction spots very close in k space, proving the excellent beam focusing and collimation at the sample position.

Furthermore, in order to avoid path length differences, the sample has to be oriented in a position as close as possible to normal incidence.
In these conditions, the LEED optics allow the reflected electrons to be detected within 55°-95° scattering angle, which means only on half of the LEED screen. A measurement of this kind is shown in Fig. 17 where the clean Ag(111) sample surface was probed with an electron beam produced by 1 nJ/pulse laser pulses. The angle of incidence is 85° and the electron energy and the azimuthal angle was chosen so that the (3,0) spot was visible on the screen.

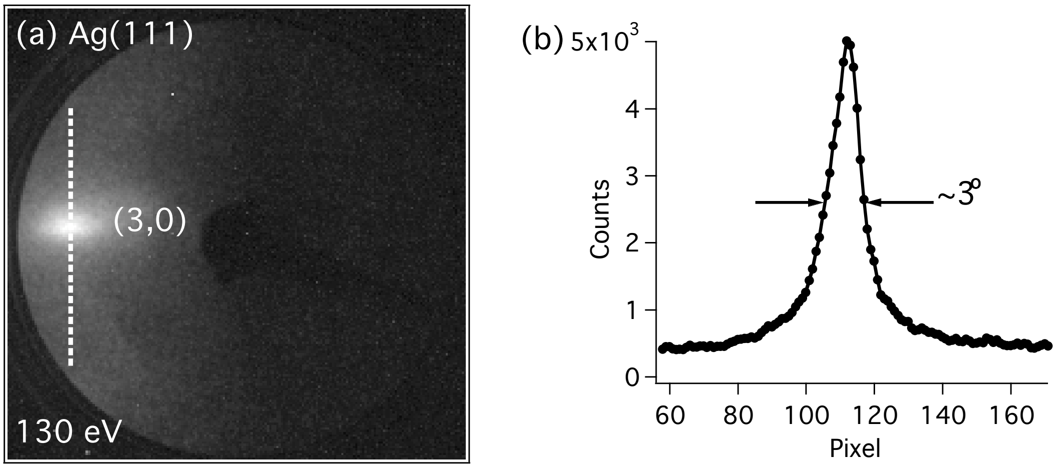

Figure 17: *a) LEED pattern taken almost at normal incidence (θ=85°) from Ag(111) crystal with exposure time of 30 seconds and laser power of* 1 nJ*/pulse; b) Spot profile line of the (3,0) spot, whose angular width is* 3° *and the signal-to-background ratio roughly 10:1.*

Quantitative measurements can be performed for this picture: a spot profile line shows a signal-to-background ratio in the order of 10:1 and a spot width of about 3°, while an integration of the peak intensity yields about 4×10^3 electrons per second in the spot.

4 Electron Diffraction

The investigation of ultra-fast physical processes happening on surfaces requires the development of a technique which combines both time and space domain, so that it is possible to determine geometrical structures with nanometer resolution and on picosecond time scale. Techniques based on electron diffraction are capable to provide such a good spatial resolution. Generally electron diffraction methods are sorted in three main categories according to the kinetic energy of the electron primary beam, before the scattering.

- In Low Energy Electron Diffraction (LEED) electrons have kinetic energy in the range of $10 - 300\,\mathrm{eV}$. This technique is by far the most surface sensitive; also at normal incidence, the perpendicular to the surface component of electron momentum and consequently the penetration depth of the electrons into the crystal are small (less than 5 atomic layers). As a consequence, after the scattering from the surface, the electrons carrying the information about the structure of the first layers are detected without an appreciable loss of energy [43–45]. Moreover the signal-to-background ratio of the diffracted spots is good thanks to the high coherence of the scattered waves.

- Medium Energy Electron Diffraction (MEED) utilizes electrons with kinetic energy in the range of $0.5 - 2\,\mathrm{keV}$; MEED is often used to monitor the thickness increase during thin-film growth studies .

- In Reflection High Energy Electron Diffraction (RHEED), electrons have energies in the range of $10 - 50\,\mathrm{keV}$ and are generally directed towards the sample surface with a very small incidence angle, in order to reduce the perpendicular component of the electron momentum and the penetration depth [46].

In Fig. 18 the elastic scattering cross sections for electrons at different wavelength are shown for carbon and silver. Compared with other surface techniques like X-ray Photoelectron Diffraction (XPD), in which photons are used, several orders of magnitude in the elastic scattering cross section are gained using massive particles like electrons. This difference is further enhanced when light elements, which are almost transparent for X-rays, are taken into account.

According to Fig. 18 the electron surface sensitivity is at maximum for electron energies in the range of $10 - 100\,\mathrm{eV}$, when the electron wavelength is of the order of the distance between the atoms in the crystal (about $1.2\,\mathrm{Å}$ for $100\,\mathrm{eV}$ electrons). In this energy range, the mean free path length is limited to less than 5 monolayers. This is the energy domain of LEED which allows the direct measurement of the diffraction pattern at any angle of

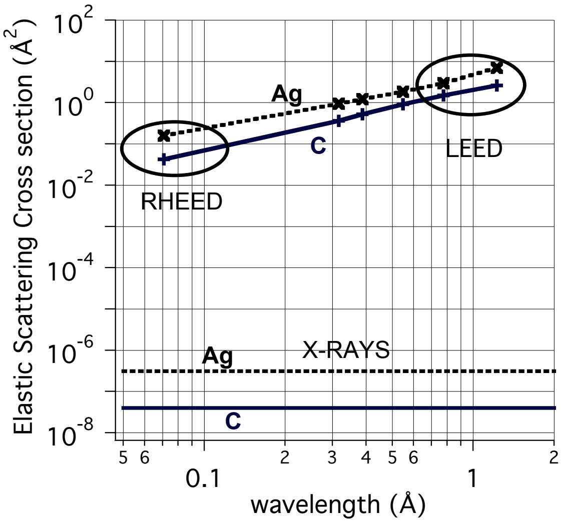

Figure 18: *Elastic scattering cross section as a function of wavelength for electrons and photons for carbon (C) and silver (Ag). The data for the electron scattering cross sections are calculated applying the optical theorem using the theoretical values tabulated by Fink and coauthors [47, 48], while for X-Rays a simple Thompson scattering model is used.*

incidence. The main type of information which can be extracted are the interlayer spacings or height differences between layers, with an accuracy of approximately ±0.02 Å. When higher energies are used, as in the case of RHEED, some geometrical constraints are put into the game in order to reduce the electron mean free path length; in general, the electrons are sent towards the crystal surface with a very small grazing angle, normally only $1-2°$. In Fig. 18 the cross sections for the electrons have been calculated applying the optical theorem and using the coefficients tabulated by Fink and coauthors [47,48], for photons a simple Thompson scattering model, independent of the wavelength has been used.

4.1 Introduction to LEED

The first evidence of low energy electron diffraction has to be dated back to 1927, when Davisson and Germer observed, almost by accident, pronounced maxima in the angular distribution of electrons backscattered from a Nickel crystal [49].

Low energy electrons, with incident energy from 10 eV to 300 eV, have wavelengths of the order of the Angstrom, which are comparable to the spacing between atoms both parallel and perpendicular to a crystal surface; this results into an interference of the electrons waves with the periodic arrangement of the surface atoms.

A standard setup of a LEED experiment is shown in Fig. 19a: electrons with a defined energy produced by an electron gun, hit the sample surface and are partially back-scattered and propagate out from the sample toward a display detector. This detector has four concentric hemispherical grids and an outer phosphor screen; the first and the last grid, and sample are at ground potential. The second and third grids are at a potential several volts less than the electron beam voltage. The screen is held at several thousand

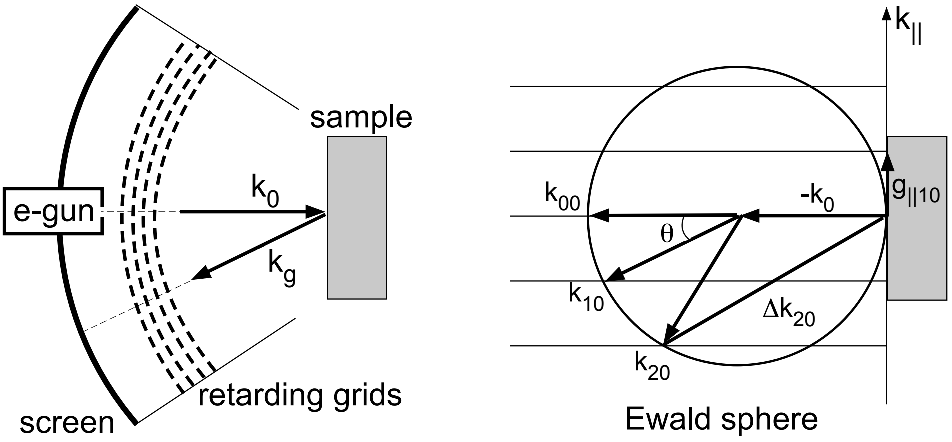

Figure 19: *Tthe LEED experimental setup is shown on the left-hand-side: electrons hit the sample surface with a incident momentum* $\mathbf{k}_0$ *and are backscattered towards the screen in some preferential angular directions* $\mathbf{k}_g$*; on the right-hand-side two-dimensional Ewald construction used to find the constructive interference directions.*

volts. Diffracted beams travel from the sample toward the detector's first grid through a field-free region. The next two grids filter out most inelastically scattered electrons coming from the sample. The electron beams then travel through the fourth grid and are accelerated toward the screen, where are imaged as fluorescent spots.

With this procedure, the elastically diffracted electrons map the surface reciprocal lattice; this pattern gives direct information about the symmetry and in-plane spacing of atoms in a surface. In fact constructive interference occurs when the momentum transfer $\Delta\mathbf{k} = \mathbf{k}_g - \mathbf{k}_0$ is equal to a reciprocal lattice vector $\mathbf{g}$ (Laue diffraction condition).

The direction of the scattered electrons can be found with the construction of the Ewald sphere, as depicted in Fig. 19b. In presence of a surface the periodicity of the crystal reduces from three to two dimensions, because of the discontinuity in the direction perpendicular to the surface. In this situation the reciprocal lattice consists of distinct points in any plane parallel to the surface which form extended rods in the normal direction.

The vectors $\mathbf{k}_g$ which fulfill the Laue condition are then given by the intersection of the Ewald sphere with the reciprocal lattice rods.

As mentioned in the previous section, low energy electrons are considered the best tool for structural determination of surfaces. Since most of surface structures have been solved by means of LEED, it is generally accepted that this technique is unique in extracting cristallographic data of ordered surfaces.

For this purpose a standard experiment is realized as follows: the intensities of the dif-

fraction spots (I), at a fixed parallel momentum transfer, are recorded while scanning the energy of the incident electrons (V). These so-called I-V experimental curves are then compared by an automated “trial-and-error” procedure with the theoretical ones, calculated with multiple-scattering program, until the best agreement between theory and experiment is achieved and the surface geometry is found [43, 50].
Nowadays, the LEED tool has reached such a high level of reliability which renders this method a standard technique in surface crystallography. This is demonstrated by the fact that about 50% of the newly determined surface structures are solved by LEED. Moreover the atomic geometry of complex surface structures, like for instance coadsorption systems, can be determined by exploiting the diffraction patterns of low energy electrons [51].
But LEED measurements are also suitable to provide information about dynamics, like thermal motion, of the topmost atoms of a crystal or particles adsorbated at the surface [52]; indeed the statistical movement of atoms around their equilibrium positions modifies the two-dimensional periodicity and thus it redistributes the reflected electrons away from the Bragg peak direction into the background, resulting into an attenuation of the LEED spot intensity. In the case of isotropic vibrations, such as the ones induced by thermal motions, this decrease of intensity can be described by the well known Debye-Waller (DB) factor [53].

4.2 Debye-Waller theory

In the Debye-Waller treatment, electron diffraction is described by the kinematic theory; for isotropic vibrations, the damping of the scattering intensity is equivalent to temperature-dependent phase shifts. These temperature-dependent phase shifts are mostly used in LEED calculations to take into account thermal vibrations of the atoms, respecting the multiple-scattering nature of LEED [54]. Therefore theoretical I-V curves completed with temperature-dependent effects can be still calculated and compared with the experimental ones.
An explicit equation describing the drop of a diffraction spot intensity as function of temperature can be derived, by using scattering phase shifts and neglecting the multiple scattering between the atoms.
Let’s consider N surface unit cells, each one containing n atoms; if we perform a scattering experiment with an incident electron beam energy E, the reflected amplitude for a specific Bragg spot identified by the index g is given by a sum over all the contributions from each single atom and can be written in the form [52]:

$$A_g(E) \propto \sum_{p=1}^{n} \sum_{j=1}^{N} f_p(\Delta \mathbf{k}_g) e^{-i\Delta \mathbf{k}_g \cdot \mathbf{r}_p^j} \tag{2}$$

where the momentum transfer $\Delta\mathbf{k}_g$ is given by the difference between the wave vector of the *reflected* wave $\mathbf{k}_g$ and the wave vector of the *incident* wave $\mathbf{k}_0$: $\Delta\mathbf{k}_g = \mathbf{k}_g - \mathbf{k}_0$; f_p is the atomic scattering factor and $\mathbf{r}_p^j$ is the instantaneous position of the atom p in the unit cell j.

When the atoms are set in motions they are free to vibrate about their mean position $\mathbf{r}_p^j$. A good approximation consists in assuming that diffracting electrons move so quickly compared to the motions of atoms, that the latter can be thought as having unchanged displacement during the process of diffraction. This is the Born-Oppenheimer approximation, which corresponds to neglecting energy loss to phonons and is usually achieved since electrons move faster than atoms by a factor of 10^3 and the typical energy losses would be $\ll 0.1\,\mathrm{eV}$.

The reflected intensity, proportional to $|A_g|^2$, follows from Eq. (2)

$$I_g(E) \propto \sum_{p,q=1}^{n} \sum_{j,l=1}^{N} |f_p(\Delta\mathbf{k}_g)|^2 e^{i\Delta\mathbf{k}_g \cdot \mathbf{r}_p^j} e^{-i\Delta\mathbf{k}_g \cdot \mathbf{r}_q^l} \tag{3}$$

Although the atoms are effectively stationary on the time scale of the diffraction process, their motion is sufficiently rapid for a detector to record intensities averaged over atomic displacements; assuming uncorrelated movements of atom p unit cell j and atom q in unit cell l then the thermal averaged intensity can be written as

$$I_g(E,T) \propto N^2 \left| \sum_{p=1}^{n} f_p(\Delta\mathbf{k}_g) \langle e^{-i\Delta\mathbf{k}_g \cdot \Delta\mathbf{r}_p} \rangle_T e^{-i\Delta\mathbf{k}_g \cdot \mathbf{r}_p^0} \right|^2 \tag{4}$$

The average $\langle e^{-i\Delta\mathbf{k}_g \cdot \Delta\mathbf{r}_p} \rangle_T$ represents the temperature correction due to the vibration of the atom p about its equilibrium position $\mathbf{r}_p^0$ with amplitude $\Delta\mathbf{r}_p$.

Since it is possible to prove that $\langle \exp(-i\Delta\mathbf{k}_g \cdot \Delta\mathbf{r}_p) \rangle_T = \exp(-\frac{1}{2}\langle [\Delta\mathbf{k}_g \cdot \Delta\mathbf{r}_p]^2 \rangle_T)$ and considering for simplicity the case $n = 1$ (only one atom per unit cell), then Eq. (4) takes the form

$$I_g(E,T) = I_g(E) e^{-M} \tag{5}$$

where the factor $I_g(E)$ includes all the terms *non*-temperature dependent and corresponds to the spot intensity for the beam labeled g at the energy E for a hypothetical rigid lattice.

The term $\exp(-M)$ is called *Debye-Waller factor* with

$$M = \langle |\Delta\mathbf{k}_g \cdot \Delta\mathbf{r}|^2 \rangle_T \tag{6}$$

4.3 Surface Debye temperature

In the Debye-Waller treatment atomic vibrations are assumed to be *harmonic*. In general this assumption is quite valid in all the range of temperatures when considering the

intensity of the elastic diffraction peaks, as it is in the case of LEED.
If the atomic vibration amplitudes are also assumed to be *isotropic*, then the atomic scattering matrices result to be diagonal in angular momentum space; while this condition is always valid for atoms in the bulk, for surface atoms it is fulfilled only for vibrations perpendicular to the surface. For low-order beams, in the LEED geometry close to normal incidence, $\Delta\mathbf{k}_g$ is almost perpendicular; therefore we mainly measure the mean-square atomic vibrational amplitude perpendicular to the surface.
Under these conditions, the thermal averaging procedure in Eq. (6) can be resolved:

$$\langle|\Delta\mathbf{k}_g\cdot\Delta\mathbf{r}|^2\rangle_T \approx \langle(\Delta\mathbf{k}_g)_\perp\cdot\Delta\mathbf{r}_\perp\rangle_T^2 \approx |\Delta\mathbf{k}_g|^2\langle\Delta\mathbf{r}_\perp^2\rangle_T \tag{7}$$

The separation performed in the second step of Eq. (7) is a consequence of the isotropic vibration amplitudes assumption.
Using the Debye model of lattice vibrations, the mean square displacement $\langle\Delta\mathbf{r}_\perp^2\rangle_T$ can be written

$$\langle\Delta\mathbf{r}_\perp^2\rangle_T = \frac{3\hbar^2}{mk_B\theta_D}\Big[\frac{1}{4}+\frac{T^2}{\theta_D^2}\int_0^{\frac{\theta_D}{T}}\frac{x}{e^x-1}dx\Big] \tag{8}$$

where k_B is the Boltzmann constant, m the mass of the vibrating particle at the temperature T and θ_D is the *surface Debye temperature* which can be intended as a measure of the compressibility of the solid: the higher is θ_D, the harder is the solid.
In the high temperature limit when $T \gg \theta_D$, then Eq. (8) can be approximated as

$$\langle\Delta\mathbf{r}_\perp^2\rangle_T \approx \frac{3\hbar^2}{mk_B}\frac{T}{\theta_D^2} \tag{9}$$

Finally, combining Eq. (5), Eq. (7) and Eq. (9), the intensity of the scattered electrons can be written as

$$I_g(E,T) = I_g(E)\exp\Big(-|\Delta\mathbf{k}_g|^2\frac{3\hbar^2}{mk_B}\frac{T}{\theta_D^2}\Big) \tag{10}$$

Therefore the logarithm of the intensity plotted as a function of temperature T gives a straight line. From the slope the surface Debye temperature, related to the mean-square atomic vibrational amplitude perpendicular to the surface, can be calculated.
This approach can be applied not only to surface atoms vibrating in high-symmetry sites of a close-packed surface, but also to adatoms moving for instance in the on-top position.
In Eq. (10) the value of $|\Delta\mathbf{k}_g|$ are obtained from the LEED pattern.

4.3.1 Surface Debye temperature of C_{60}/Ag(111)

The approach explained in the previous sections was applied to the C_{60}/Ag(111) system. It is known that C_{60} evaporated on clean Ag(111) surface forms a $(2\sqrt{3} \times 2\sqrt{3})R30°$ commensurate structure [33].

For such a molecular arrangement, the vibrational modes can be either *intermolecular* or *intramolecular*; in addition, the first can be classified into two types: translational modes which are of the standard one atom per basis varieties (with the C_{60} molecule taking the role of a large single atom), and the rotational modes (librons).

Phonon dispersion and density of state calculations for solid C_{60} show that inter- and intramolecular modes are well separated in energy by a gap of nearly 22 meV [55]. In particular the intermolecular-phonon density of states shows peaks at around 2.3 and 3.7 meV and extends up to 7.6 meV, well below the region of the intramolecular vibrational modes, which are calculated at energies larger than 30 meV.

It is the large difference in bond strength between the covalent bonds on the cage (intramolecular) and the molecular bonds between the cages (intermolecular) that leads to this separation of energies in the phonon spectrum.

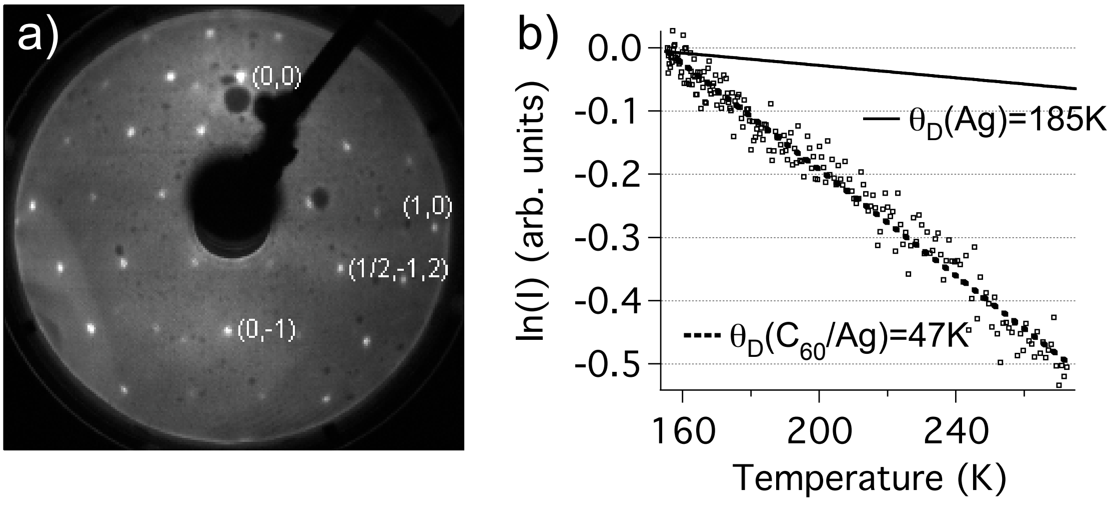

Figure 20: *a) LEED pattern of one monolayer of C_{60} on Ag(111) collected at T=150 K with electron energy E=44.5 eV, the integer order spot and the specular are labeled as reference. b) Temperature induced intensity reduction (Debye-Waller curve) in the $(1/2, -1/2)$ spot: the dashed line is the best fit resulting in a surface Debye temperature $\theta_D = 47\,\mathrm{K}$. The solid line represent the experimental curve measured for the (1,0) spot of the clean Ag(111) substrate, where a surface Debye temperature of* 185 K *is obtained.*

As previously stated LEED is in general sensitive to vibrations of adsorbates with quite large mean-square displacements perpendicular to the surface, which are in turn associated with small vibration energies. This means that a measurement of the LEED spot intensity reduction due to a temperature raise would give access to the determination of the energy of the C_{60} molecules oscillating in the direction perpendicular to the Ag(111) surface.

Fig. 20 shows an experiment of this kind. The LEED pattern was collected at a temperature of about 150 K, with electron beam energy E=44.5 eV; an angle of incidence of 10° allows the detection of superstructure spots with larger parallel momentum transfer. In Fig. 20 the positions in the reciprocal space of the integer order spots and of the superstrucure $(1/2, -1/2)$ spot are marked.

In the right-hand-side the temperature induced reduction of the $(1/2, -1/2)$ spot intensity is shown. The integrated intensity of the spot under investigation is recorded while the temperature is raised, or lowered, and normalized with respect to the background. In the plot of Fig. 20b the logarithm of such normalized intensity is shown as a function of temperature: the linear fit of these data yields a surface Debye temperature of 47 K. The same experiment performed on the (1,0) spot intensity of the clean Ag(111) surface at the same energy gives a surface Debye temperature of 185 K. These two measurements are not directly comparable, because realized on two different spots of two different systems (in Eq. (10) the mass of the vibrating particle plays an important role). Nevertheless in the plot of Fig. 20b both curves are displayed to enhance the slope change of the intensity drop: the solid line represents the intensity attenuation which the C_{60}/Ag(111) $(1/2, -1/2)$ spot would manifest if the system would have the same surface Debye temperature as the clean silver surface.

As expected the value of θ_D measured for surface silver atoms is roughly 20% smaller than the *bulk* Debye temperature, which is known to be 225 K [56]: this difference demonstrates the increased thermal vibrations of surface atoms (mainly in the normal direction) relative to those of the bulk.

From Eq. (9) we know that a given Debye temperature defines an univocal mean-square displacement. In the harmonic approximation, the latter can be related to the vibrational frequency $\omega_\perp$ via the formula

$$\langle \Delta \mathbf{r}_\perp^2 \rangle_T \approx \frac{k_B T}{m \omega_\perp^2} \tag{11}$$

Table 2 reports a set of measurements of surface Debye temperature together with the corresponding energy $E_{vib,\perp} = \hbar\omega_\perp$ at different energies for ten C_{60}/Ag(111) superstructure and one integer LEED spots.

It has to be noted that these data where obtained with 7 different preparations following the same recipe: after each preparation the temperature ramp was performed only once

Table 2: *Surface Debye temperatures and corresponding perpendicular vibrational energy $E_{vib,\perp}$ of 1 ML C_{60}/Ag(111) measured for different beams at different incident electron energies.*

Energy (eV)	Beam index g	θ_D(K)	$E_{vib,\perp}$(meV)
42.2	$(-1/3, -2/3)$	40	2.0
	$(0, -1/2)$	42	2.1
	$(1/3, -1/3)$	44	2.2
44.5	$(1/2, -1/2)$	47	2.3
	$(1/2, 1)$	46.5	2.3
49	$(1/6, -1/6)$	46.5	2.3
	$(-1/6, -1/3)$	48	2.4
51.2	$(-5/6, -7/6)$	42	2.1
	$(0, -1)$	55.5	2.8
56	$(1/6, -1/6)$	48	2.4
70	$(1/3, 1/6)$	52.5	2.6
80.1	$(1/3, 1/6)$	49	2.4

at a fixed energy, sometimes recording the intensity of more than one not-equivalent spot.

The average surface Debye temperature results $46 \pm 4\,\mathrm{K}$ and the corresponding average perpendicular vibrational energy $2.3 \pm 0.2\,\mathrm{meV}$. These values are simply the mean values of the results displayed in Table 2, but some additional interesting information can be inferred plotting the surface Debye temperature or the vibrational energy as a function of the incident electron energy over the exploited energy range.

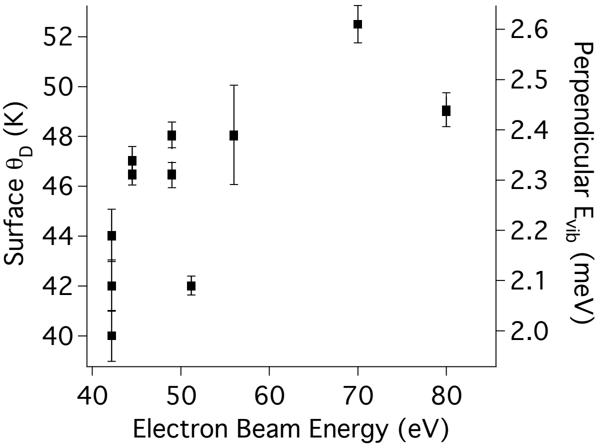

Figure 21: *Surface Debye temperature (left axis) or perpendicular vibrational energy (right axis) as a function of the electron beam primary energy over a range of about* 40 eV *for the superstructure spots of C_{60}/Ag(111) listed in Table 2. The error bars are obtained by the fitting procedure.*

Fig. 21 shows a likely increase of the surface Debye temperature with increasing electron energy. This trend can be explained if we take into account that an increase of energy would result into an increase of the electron mean free path length into the crystal: some of the impinging electrons may probe not only the C_{60} molecules but also the silver substrate atoms, whose surface Debye temperature is almost 4 times larger [46].

An additional hint supporting this view of the substrate contribution is given by the result obtained for the integer $(0, -1)$ spot (see Table 2), where the surface Debye temperature is roughly 30% larger than the one deduced at the same energy for a not-integer diffraction spot.

On the other hand, in the presented analysis the contribution to the spot intensity drop given by the *lateral* translation of the C_{60} molecules has been neglected. This assumption may be considered no longer valid in the low energy domain, where the contribution of mean square displacement parallel to the surface $\langle \Delta \mathbf{r}_{||}^2 \rangle_T$ is more important than for higher energies, where $(\Delta \mathbf{k}_g)_\perp$ is larger. Therefore the parallel contribution to the Debye-Waller factor has to be included in Eq. (7), rendering the determined value of $E_{vib,\perp}$ larger.

In conclusion, the measured $I(T)$ traces show an apparent Debye-Waller behavior, i.e. an exponential decrease of the intensity with the temperature. The value of 2.3 meV for the average perpendicular energy, deduced in the framework of the Debye-Waller theory, fits reasonably well with the literature values tabulated for intermolecular vibrations, like translational or rotational (librons) modes [57, 58].

Furthermore the data shown in Fig. 20 and summarized in Table 2, in particular the relatively low value of the surface Debye temperature for C_{60}/Ag(111) indicates how sensitive this molecular system reacts on temperature changes and how suitable LEED is as a tool to follow this variation.

5 Pump-and-probe experiments

5.1 Introduction

Fundamental processes happening on the molecular level, such as vibrations and rotations of molecules or breaking of chemical bonds occur on the time scales of femtoseconds to picoseconds.

If one is going to take a look at events that happen over the span of picoseconds, then one needs to be *ultrafast*. That is where the pump-probe technique comes into play.

First, one has to "pump", or trigger an event by applying a laser pulse that induces an excitation of the sample. The sample is disturbed from its equilibrium and returns after some time to its initial state. One keeps pumping the sample at regular intervals, that need to be longer than the response of the sample to ensure that there is no overlap of excitation events from the current pump and the previous pump.

There are all kinds of interesting interactions that can occur, so looking at what happens is a good start to sorting out the details of those interactions. If one can pump the sample and get it to behave the same way over and over again, then one can probe it and find what is happening over those short intervals. In other words: a reversible process is required.

While the sample is changing, one wants to *probe* the response of the system to the excitation event that has been created. In general in pump-probe experiments both pulses are originated from a single laser pulse at the beginning. Then part of the beam from the laser is split by a beam splitter and sent off to travel over a different path. This path includes a “delay line” which is a device that varies the path length that the light has to travel with respect of the pump beam.

If both pulses are generated from the same laser pulse, the *"time zero"* (coincidence between pump and probe) is clocked by the source itself and can be found back at the interaction region, provided that both beams travel for the same time from the point where they are split till they rejoin on the sample.

Fig. 22 shows the principle of a pump-probe experiment: the curve represents a hypothetical excitation curve (induced by the pump pulses), which can be read the probe pulses. When the probe pulse arrives at the sample surface at different time delays, it records the system in different conditions. The time axis represents the arrival time of the probe pulses with respect to the pump pulses and translates into different positions of the delay stage.

1. The probe pulse arrives *before* the pump, meaning before the excitation starts, the system is still in equilibrium.

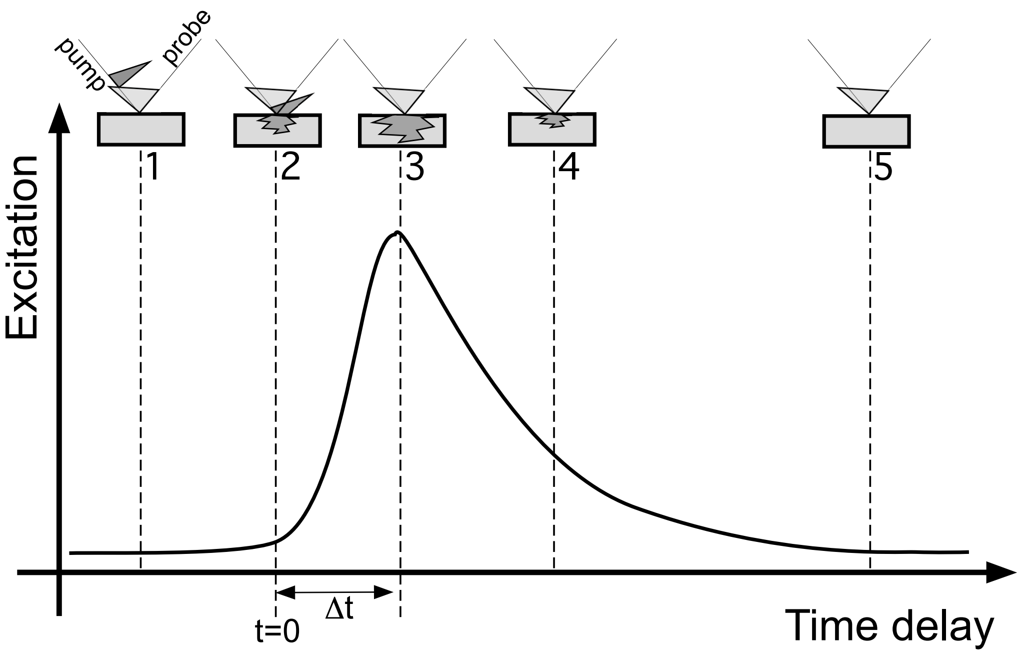

Figure 22: *Principle of a pump-probe experiment, seen at different delay times. 1. The probe pulse comes before the excitation starts, the system is in equilibrium. 2. Pump and probe pulses arrive at the same time on the sample and the excitation starts (time zero). 3. The pump pulse is completely adsorbed, the system is out of equilibrium. 4. The system relaxes while the transient excitation gets over. 5. The system is back to the equilibrium condition.*

2. The pump and the probe pulses hits the sample surface at the same time; the excitation starts and the system goes out of equilibrium. As a convention the time $t = 0$ (time zero) can be set here.

3. The excitation reaches its maximum.

4. The probe pulse arrives when the pump-induced effect is decreasing and the system is relaxing towards its equilibrium.

5. The system is back to its equilibrium.

As mentioned before, the full transient excitation (from time delay 2 to 5, referring to Fig. 22) has to be reversible and shorter than the time distance between two consequent pump pulses. In this way, keeping fixed a delay stage position the system can be probed many times in the same condition before moving to a different delay time. This procedure permits the acquisition of data integrated until the desired signal-to-noise ratio is reached. In our standard setup the repetition rate is 250 kHz, thus the pulse separation is 4 µs, long enough to allow the system to come back to its equilibrium state after the excitation process, which normally lasts no longer than some tenths of nanosecond.

While the pump pulses are in most of the cases photons, the probe pulses may be either photons or X-rays or electrons. In all pump-probe experiments the pump and the probe beams have to be overlapped both *spatially* and *temporally* at the center of interaction.

In a photon-photon experiment, the spatial overlap is realized simply superimposing the two spots at the sample surface, while the temporal overlap is achieved when the two laser beams travel exactly the same distance.

In a photon-electron experiment this procedure is more complicated since the electron spot can rarely be directly seen and the electron time of flight depends on the electron velocity, which means electron energy. For instance it takes the same time for 100 eV electrons to fly over 1 mm as for light to travel over 47 mm. Thus for each energy the time delay between photon-pump pulse and electron-probe pulse has to be adjusted. In this aspect it is desirable to have at disposal a simple method to establish both spatial and temporal overlap independently of the experiment on the sample surface itself.

Following the procedure explained in reference [22], the determination of coincidence in space and time is now obtained with a routine measurement and used as reference for the experiments performed on the sample surface.

5.2 Electron-Photon pulse correlator

The cross-correlation between light and electron pulses for time-resolved electron diffraction experiments is performed exploiting the onset of a space-charge by the pump laser pulses. The pulsed electron beam is threaded through a 0.5 mm diameter pinhole drilled into an aluminum plate, while the pump laser beam is focused onto the pinhole itself, producing an electronic space charge by multiphoton photoemission. In coincidence, the transmitted flux of electrons changes due to the Coulomb interaction between the electrons in the pulse and the ones in the space-charge cloud.

With such a setup, the spatial overlap between electrons and photons is determined by the pinhole itself while the temporal overlap is obtained by recording the transmitted electron yield as a function of the delay between electrons and photons; moreover, the fastest feature observed in the transient transmission can be used to set an upper limit for the electron pulse duration, which eventually defines the experimental time resolution (see also section 3.4.4).

If the sample is then placed exactly at the same distance from the electron gun as the aluminum plate, then the temporal and spatial coincidence is preserved, and the reference time delay “zero” is set.

Fig. 23 shows a correlation curve for 100 eV electron pulses produced with the LEED gun

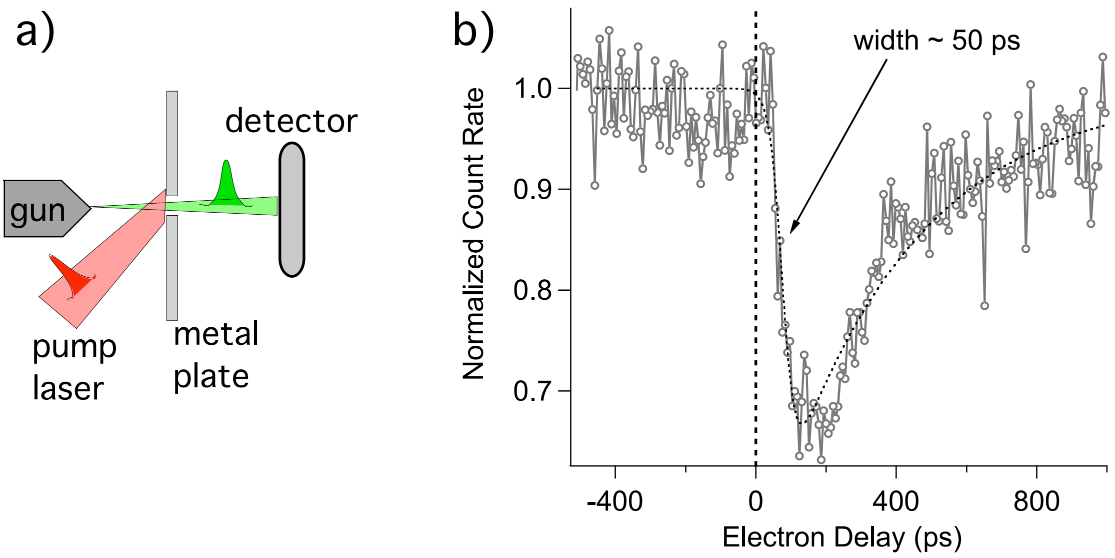

Figure 23: *a) Sketch of the pinhole electron-photon pulse correlator: electron pulses coming from the gun pass through the* 0.5 mm *diameter pinhole and are detected by a single-electron detector, while the space-charge cloud is created by the* 800 nm *wavelength laser pulses focused onto the pinhole. b) Fastest event observed in the present setup with* 100 eV *electron pulses: the leading edge is fitted with a broadened step function, whose width yields* $\Delta t = 50$ ps.

presented in section 3.1; the pump laser fluence impinging the 0.5 mm diameter pinhole is 1.2 mJ/cm^2 and the cathode-plate distance is about 10 mm. For each delay position the data were normalized by the count rate measured without pump light.

The correlation curve shown in Fig. 23b can be fitted with the following equation, which represents a combination of a Fermi-Dirac function to describe the leading edge and an exponential function to follow the relaxation:

$$I(t) = \frac{I_0}{1 + e^{\frac{-(t_0 - t)}{\Delta t}}} e^{-\frac{(t_0 - t)}{\tau}} + C \tag{12}$$

where $I(t)$ is the normalized electron transmission through the pinhole, I_0 is the signal amplitude and C an offset constant; t_0 defines the leading edge position, while Δt and τ are the two characteristic temporal parameters, describing the onset and the lifetime of the space charge effect, respectively.

As mentioned above, the temporal width of the cross correlation curve leading edge Δt may be used to determine an upper limit of the temporal electron pulse width, which limits the intrinsic time resolution of the experiment. The fit of the data shown in Fig. 23b results in a leading edge of width $\Delta t = 50$ ps. This value is slightly larger but still in good agreement with the 16 ps predicted by Eq. (1) when the distance cathode-plate is equal to 10 mm.

Even though the temporal profile of the electron pulses cannot be characterized as precisely as with a streaking technique measurement [59], the main advantage of this method resides in the possibility of sampling the pulses directly at the interaction region and in its easiness to obtain the pulses coincidence.

5.3 Coincidence without the pinhole correlator

For the actual electron scattering experiments, an hemispherical electrostatic energy analyzer was used as already presented in section 2.2. With this setup, we expect to have a better time resolution, due to the monochromaticity of the detected electrons, and a faster data acquisition, since it allows to obtain normalized intensity curves with a chopping rate of about 20 Hz, which is enough to remove most fluctuations in the laser intensity.

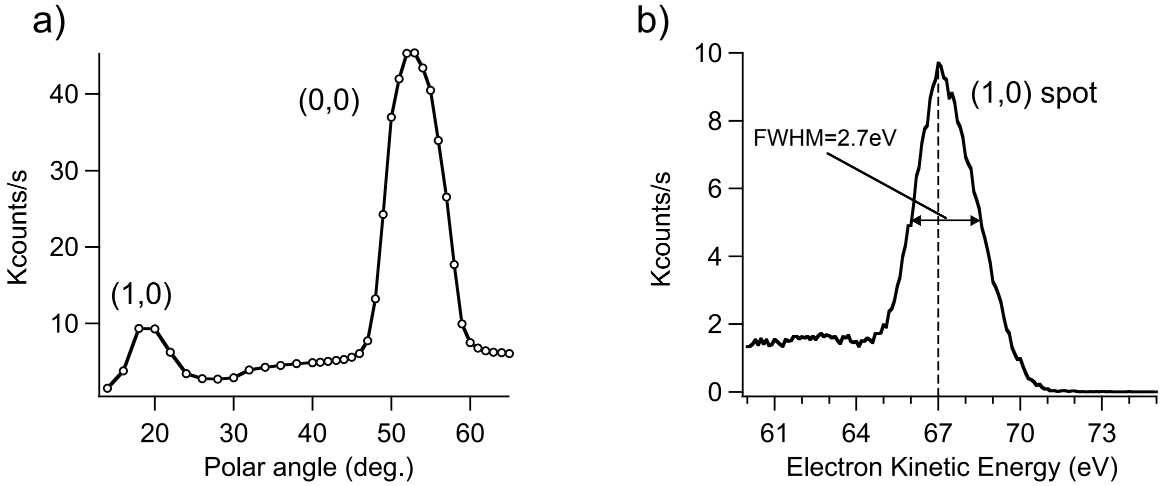

Figure 24: *a) Polar scan along the (10) direction of clean Cu(111). b) Energy resolved (1,0) spot measured with* 67 eV *kinetic energy electron pulses: a gaussian fit of the spot profile results in an energy width of* 2.7 eV*.*

In order to perform time resolved electron scattering experiments one needs to set the sample manipulator polar and azimuthal angles in such a way that one of the diffracted beams is directed into the acceptance cone of the electron analyzer.

Fig. 24a shows a polar scan along the (10) direction of clean Cu(111) surface collected with 67 eV electron pulses produced by 4 nJ laser pulses; the sample was rotated around the polar angle, while the intensity of the diffracted peak maximum was recorded with the electron energy analyzer. Clearly two peaks are detected: at an angle of incidence of 52° referred to the sample surface normal the high intensity peak has been labeled as the specular (0,0) spot and at 20° polar angle, the first order LEED spot with indices (1,0). The angular separation between the two spots is in good agreement with the reciprocal space distance deduced from a LEED pattern collected at 67 eV. The signal-to-background ratio for the first order LEED spot is roughly 5:1; Fig. 24b shows an energy scan of the (1,0) spot, the full width at half maximum of which is 2.7 eV.

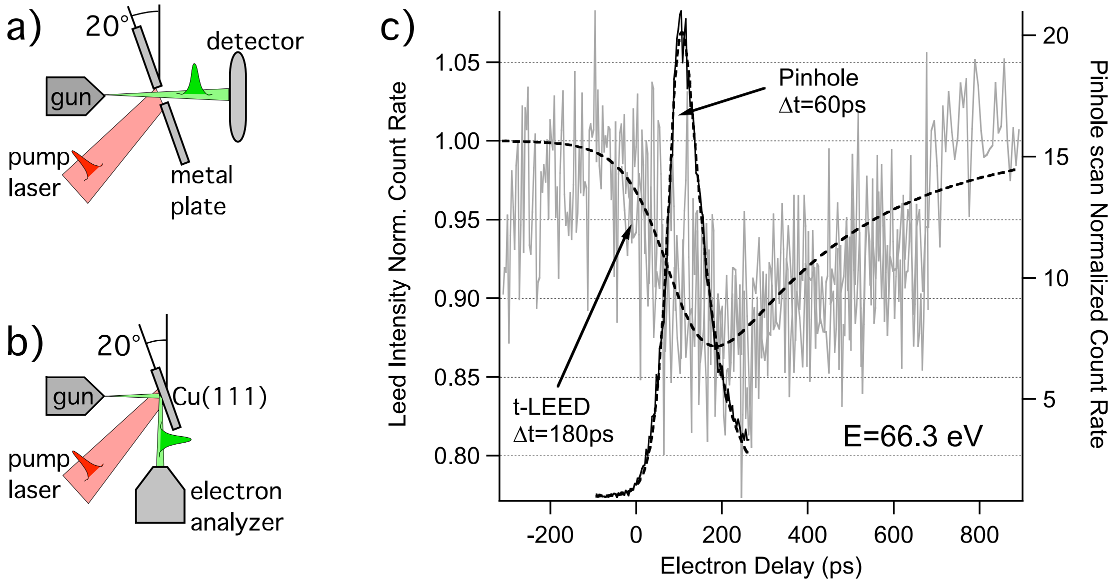

Figure 25: *a) Sketch of pinhole electron-photon pulse correlator with metal plate tilted* 20° *out of normal incidence. b) The Cu(111) single crystal is located exactly in the same position as the aluminum plate in a): the (1,0) LEED spot hits the acceptance cone of the electron energy analyzer. c) Cross correlation curve between laser pump and* 67 eV *electron probe beam for the pinhole correlator together with the (1,0) copper LEED spot; for the latter, the energy selected was* 66.3 eV, 0.7 eV *less than the peak maximum position (see spectrum in Fig. 24b).*

Once the desired LEED spot hits the acceptance cone of the electron energy analyzer, the time-resolved measurement can be performed. Fig. 25c demonstrates the first determination of coincidence in space and time measured recording the intensity of the (1,0) LEED spot at a fixed energy, close but not exactly at the peak maximum position. As a reference, the cross correlation curve measured with the pinhole electron-photon pulse correlator is shown in the same graph. In order to enhance the signal from the diffracted spot, the pump laser fluence was increased by increasing the pulse energy and decreasing the spotsize on the sample surface: however just a 15% effect is detected when the pump laser fluence is as high as $1.2\,\mathrm{mJ/cm^2}$.

In the reference correlation curve the huge lensing effect, meaning the increase of count rate at coincidence, has been already observed when large pump laser fluences are utilized (see for instance Ref. [22]) and still the mechanism leading to it is not completely clear. For sure the shape of the correlation curve and the amplitude of the effect are strongly dependent not only on the total number of electrons in the space charge cloud, but also on the space charge dynamics. The latter is likely dependent on the relative position between the metal plate and the the pump laser beam: for instance no lensing effects have been ever measured when the angle of incidence is close to 45° and at normal incidence a shielding effect (drop of electron transmission through the pinhole at coincidence) is often observed when the laser beam is shot slightly aside the pinhole.

The cross correlation curve measured with the pinhole correlator presents a leading edge, of $\Delta t = 60\,\mathrm{ps}$ much faster than that one observed from the (1,0) LEED spot, which is about 180 ps. This resolution may be limited by the relative large angle of incidence of electron beam with respect to the sample surface normal [29] and by the intrinsic lifetime of the physical mechanism which decreases the LEED spot intensity at 66.3 eV up to 15%. Nevertheless, Fig. 25 shows the successful demonstration of coincidence determined directly at the single crystal surface.

6 Surface space-charge

In the previous chapter, it was shown that the intensity of a LEED spot diffracted from the clean Cu(111) surface is modulated by the pump laser beam: when pump photons and probe electrons hit the surface at the same time, a decrease of the spot intensity is recorded. The temporal coincidence is determined by means of the electron-photon pulse correlator, presented in section 5.2. In principle the normalized cross-correlation curve displayed in Fig. 25c may suggest that a local sample surface heating, induced by the intense pump laser, is taking place.

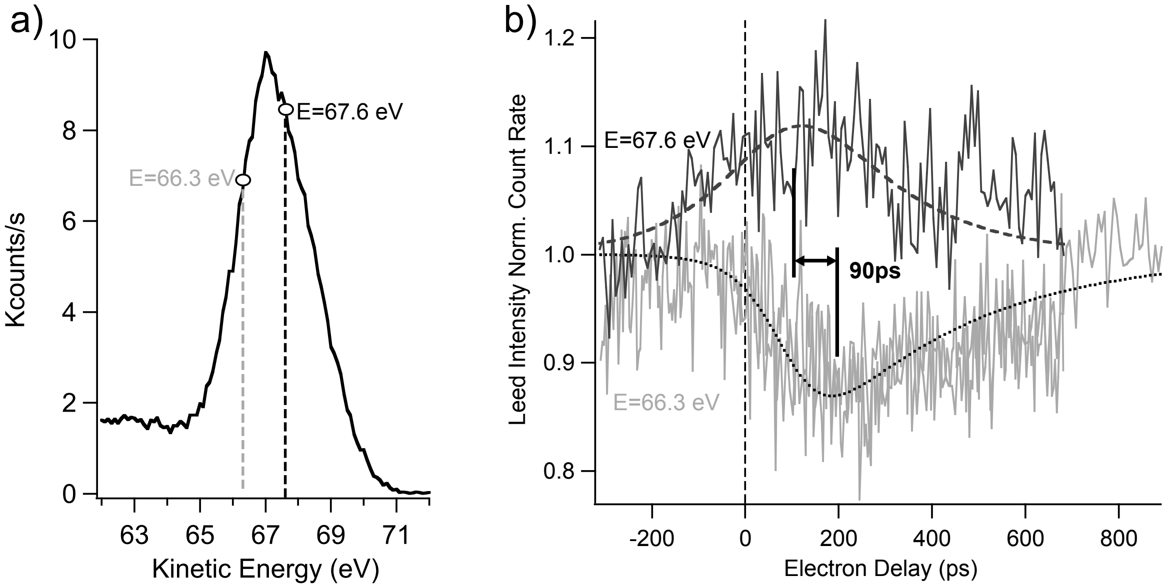

Figure 26: *Energy and time dependence of the cross correlation curves between laser pump and electron probe. a) (1,0) Cu(111) spot measured at kinetic energy* 67 eV*. b) Correlation curves measured at* $E = 67.6\,\mathrm{eV}$ *(in black) and* $E = 66.3\,\mathrm{eV}$ *(in grey), i.e., at kinetic energies slightly higher and lower than the peak maximum energy in (a), respectively.*

However, according to the Debye-Waller theory [43, 60] a 15% intensity decrease would correspond to a temperature increase of more than 70 K, even considering a surface Debye temperature θ_D some tenths of degrees smaller than the tabulated bulk value for copper, which is 315 K [56]. Instead, taking into account the specific heat of copper, $C_V = 24.47\,\mathrm{J/mol\,K}$, a laser spot size of 0.4 mm diameter and an energy deposited of 1.5 µJ per pulse, the estimated surface temperature increase results less than 4 K.
Therefore the measured effect is most likely due to transient space-charge produced by the pump laser: the high fluence pump laser pulses, impinging on the metal surface,

produce an electronic space-charge by multiphoton photoemission. In turn the short-lived space-charge affects the probing electron pulses.

This model can be confirmed demonstrating that the intensity variations are energy dependent. Fig. 26b shows the cross correlation curves for two different energies, marked in Fig. 26a; the fit of the data realized with Eq. (12) yields the same values of Δt and τ (180 ps and 350 ps, respectively) but different delays where the maximum effect is detected.

In particular the maximum of the spot intensity increase is measured to happen about 90 ps *before* the drop. The reason of such an asymmetry can be explained once the full space-charge dynamics is understood but some preliminary conclusion can already be drawn:

- The surface space-charge effect can be used to determine the temporal and spatial overlap between pump photons and probe electron pulses, directly on the sample surface.
- The laser induced electron cloud created on the metal sample surface has a lifetime in the range of few hundreds of picoseconds; its creation and evolution is a reversible process and can be studied by means of time resolved low energy electron diffraction, even with a time resolution in the order of 60 ps, like in our case.
- The full understanding of the space-charge evolution is fundamental in order to obtain transient structural information by means of t-LEED, like for instance the laser excited collective motion of adsobate molecules; indeed the space-charge signal may hide the surface structural dynamics, as previously shown for the Ge(111)-c(2 × 8) and In/Si(111)-(4 × 1) systems [61].

6.1 Specular beam scattering

In order to study in detail the space-charge dynamics we adapted our experimental setup so that the specular electron beam back-scattered from a Cu(111) crystal was detected using an electron energy analyzer. In this way, the experiment can profit from faster data acquisition, the specular beam being at least 5 times more intense than any other diffracted spot. The main drawback is the loss of the information carried by the electrons that undergo a higher-order diffraction process, but most likely the space-charge induced effects are the same for electrons of any order of diffraction, except for the different scattering angles.

For the purpose of studying the specular reflection the polar angle was set to 50° with respect to the sample normal, as deduced by the polar scan shown in Fig. 24a. An additional 0.5 mm diameter pinhole was drilled into the aluminum plate 45° off-normal: in this way the electron beam can pass trough the hole also when the manipulator is tilted in order to allow the specular beam to be detected.

The primary electron energy was optimized for maximum reflectivity of the (0,0) spot. For electron energies below 70 eV, the spot intensity varies showing a local maximum for $E = 55\,\text{eV}$; at higher energies, the electron reflectivity decreases almost exponentially. Therefore a primary energy of 55 eV was chosen for the following experiments.

6.2 Space-charge dynamics

Fig. 27 shows the response of the Cu(111) target upon 100 fs, 800 nm light pulse excitation with a fluence of 2.6 mJ/cm^2. In Fig. 27a the specular beam intensity as a function of the delay between light-pump and electron-probe pulses is displayed. The pump beam is chopped with a frequency of about 20 Hz, and for each delay stage position the data are recorded simultaneously with and without the pump beam. This allows the data recorded *with* pump light to be normalized with respect to those taken *without* pump light. The "point-by-point" normalization procedure permits to remove effects due to laser instabilities, electron gun cathode aging or misalignment of the computer-controlled delay stage which can alter the shape and intensity of the detected energy spectrum.

In order to highlight the transient changes, the asymmetry is represented in Fig. 27b as a function of the delay between pump and probe, negative delays meaning that the electrons are hitting the sample surface before the pump pulses. Here we define the asymmetry as $(I_w - I_0)/(I_w + I_0)$, where I_w is the intensity of the elastically scattered electrons when the pump light is on the sample and I_0 the one without pump light.

The temporal coincidence (delay zero) and spatial overlap is determined with a reference curve measured with the pinhole correlator, as outlined in secion 5.2.

As already pointed out in the previous section, the electron energy spectrum is affected by the pump pulse: what we observe is a delay-dependent energy shift (Fig. 28a). A Gaussian fit of the spectra yields the position of the energy spectrum peak maximum with and without pump light, the difference of which is displayed in Fig. 28a.

Electrons arriving before the pump pulse are accelerated. When the two pulses arrive simultaneously, the electron energy gain is about 50 meV (see also Fig. 27b and Fig. 27c for comparison) and a maximum shift of 60 meV is reached around 100 ps after coincidence. Electrons arriving at delays larger than 100 ps probe a gradually decreasing effect and their energy gain is consequently weaker.

These shifts cannot be explained by changes in the elastic scattering cross section, also because the normalized spot intensity, given by the energy spectrum area, doesn't show

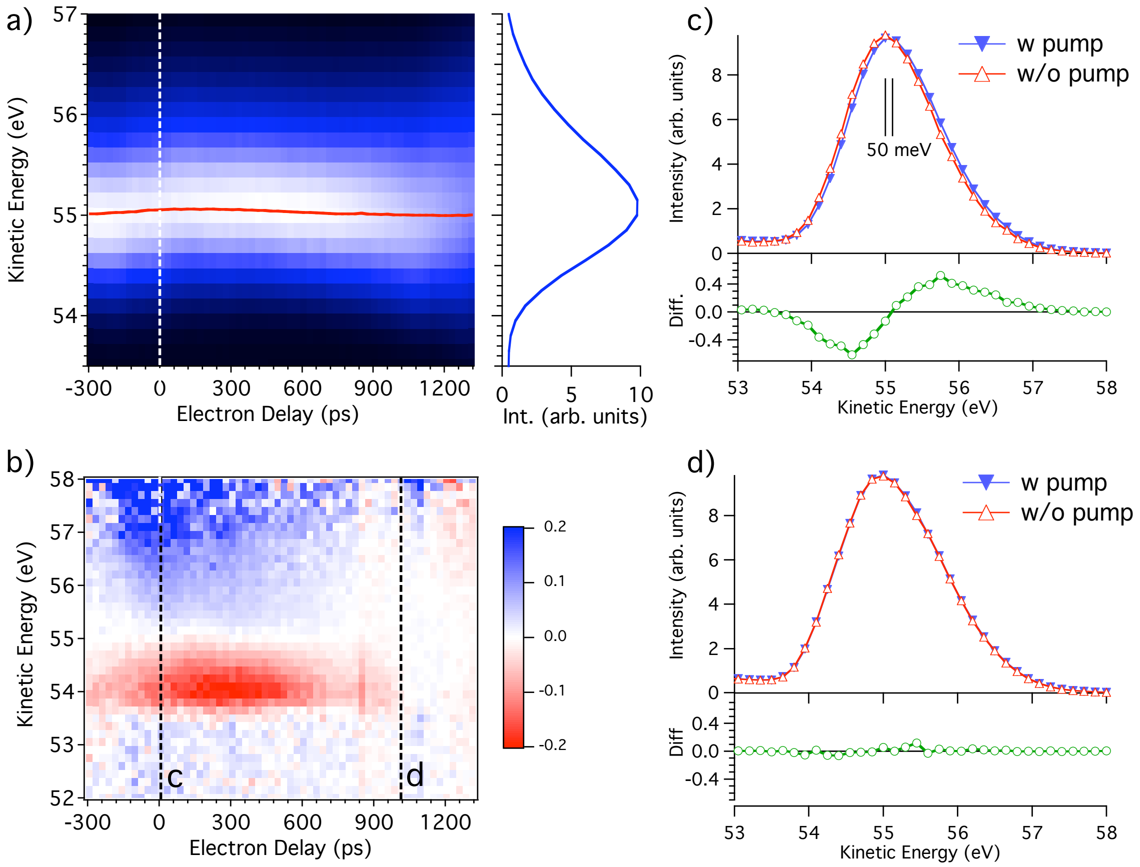

Figure 27: *Response of the energy-resolved Cu(111) specular beam upon pump laser excitation with a fluence of* 2.6 mJ/cm^2 *at* 55 eV*. a) Specular beam intensity with pump beam as a function of delay between pump and probe pulse. On the right-hand-side energy spectrum sliced out at the 0-delay (marked with the dashed line); the red solid line is the peak maximum energy position: an apparent time-dependent shift is noticeable. b) Asymmetry of the electron energy distribution* $(I_w - I_0)/(I_w + I_0)$*, where* I_w *is the intensity of the scattered electrons with pump and* I_0 *that without pump beam. c) Energy spectra with and without pump at coincidence (dashed line in b labeled 'c'). Note the shift of about* 50 meV *in the presence of the pump pulse. The bottom panel shows the difference between the two curves. d) Energy spectra with and without pump about* 1 ns *off coincidence (dashed line in b, labeled 'd').*

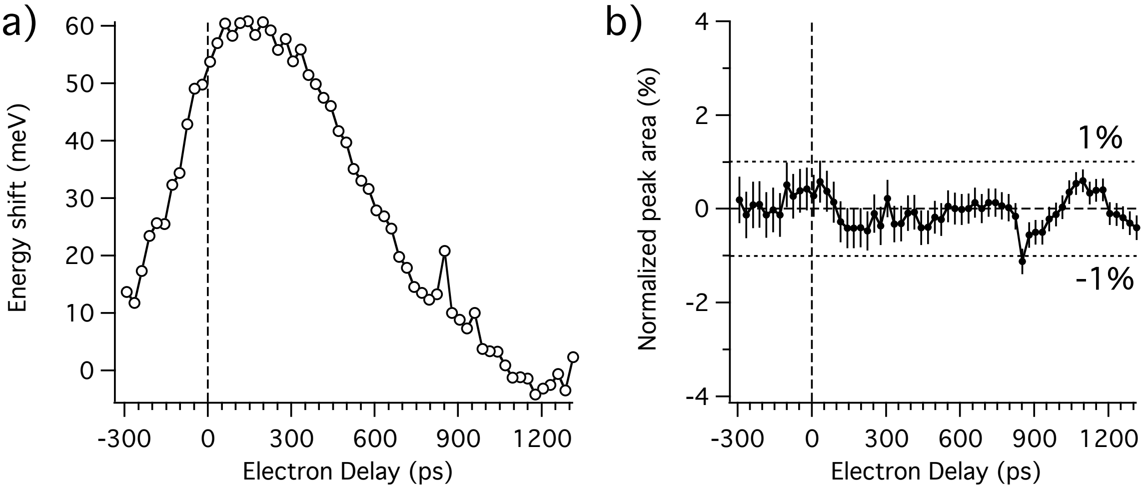

Figure 28: *Space-charge effects induced on the (0,0) spot: a) Kinetic energy gain of electrons in presence of pump beam as a function of delay: a maximum shift of* 60 meV *occurs about* 100 ps *after coincidence. b) Normalized spot intensity traced as a function of delay: no appreciable delay-dependent change is measured, since the asymmetry between the the peak area with and without pump are smaller than 1%.*

any appreciable delay-dependent modulation. Fig. 28b shows the normalized peak area as a function of delay: the total number of diffracted electrons is not altered by the presence of the pump beam, the observed changes being less than 1%, thus below the noise level. Most likely, it is the space-charge, created by the intense pump pulse (fluence of 2.6 mJ/cm^2 and duration of about 100 fs) which affects the electrons.

The time-dependent energy shift of the electron energy spectrum allows for a direct observation of the space-charge dynamics. Two asymmetry curves sliced out from the plot displayed in Fig. 27a at two different energies are displayed in Fig. 29a. The error bars are given by the statistical error due to the electron counting, defined as $\Delta = 1/\sqrt{I_w + I_0}$ [62]. Fig. 29b shows the normalized width of the diffracted spectra as a function of delay: the relative change is displayed to enhance transient effects and normalize the data with the pump with respect to the ones without the pump. This relative change is defined as $(W_w - W_0)/W_0$, where W_w is the width of the spectrum with pump and W_0 that without pump beam.

The observation that the two profiles shown in Fig. 29a are not symmetric with respect to the zero line suggests that the diffracted electrons undergo a time dependent process which strongly depends on the generation and evolution of the space-charge cloud.

Indeed due to the different electron flight time, we would expect to observe the maximum

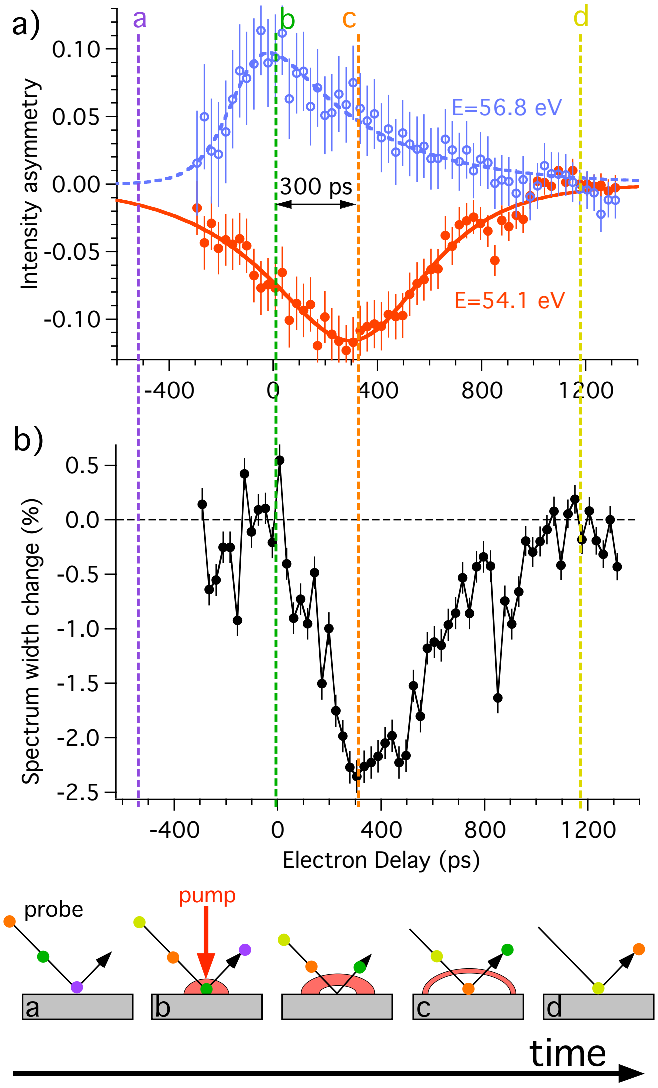

Figure 29: *a) Asymmetries as a function of time delay for electron energies equal to* 54.1 eV *(open symbols) and* 56.8 eV *(solid symbols), respectively below and above the spectral maximum. b) Energy spectrum FWHM relative change, defined as* $(W_w - W_0)/W_0$*, where* W_w *is the width of the spectrum with pump and* W_0 *that without pump beam. At a time delay about* 300 ps *after coincidence, the energy spectrum with pump beam is roughly 2% narrower than the one without pump beam. Bottom panel: sketch of the proposed model for space-charge dynamics; the colored dots represent the electron probe pulses hitting the sample surface at different delays, labeled with letters in the top panel, while the pump excited space-charge evolves with its proper lifetime (see to text for details).*

effect to occur at a different delay for any energy. However, a 2.7 eV energy difference translates into a a time of flight difference of only 5 ps/mm, too small to explain the measured 300 ps time interval (Fig. 29). Moreover this time interval cannot be due only to the experimental time resolution induced by the temporal width of the electron pulses: actually the electron-photon pinhole cross correlation curve (see section 5.2) yields in the actual setup a time resolution better than 100 ps.

An additional confirmation that what we observe is a space-charge induced effect comes from the fact that during the 300 ps time interval, the energy spectrum shape becomes narrower (Fig. 29b). However, such reduction of the spectrum energy width occurs together with a slight increase of the peak intensity: these two effects compensate each other when the integrated intensity of the diffracted spot is calculated, since no changes are measured (Fig. 28b).

In the bottom part of Fig. 29, a sketch of the proposed model of space-charge dynamics is presented for five different delays, marked with colored lines and letters in the top panel.

a) At this delay the electron probe pulses hit the surface far before the pump beam; as a consequence, they are not affected by the space-charge and neither an energy shift or a change in the diffracted peak shape is recorded.

b) This is temporal coincidence; electron pulses leave the surface after the diffraction and are accelerated by the repulsive force due to the space-charge cloud created by the pump beam just "behind" them. This measured energy shift is not energy-dependent. All the energy spectrum shifts towards higher kinetic energy in a *rigid* way, since no change in the spectrum width is observed. After its generation, the electronic density distribution evolves, most likely expanding in the region above the metal surface.

c) The electrons hitting the surface have now to pass twice across the expanding electron cloud, before and after the scattering, and are thus both decelerated and accelerated. Under the combination of these forces, the energy spectrum becomes narrower: in the 300 ps time interval after coincidence, electrons with kinetic energy smaller than 55 eV are still accelerated while those with kinetic energy greater than 55 eV are more decelerated. This "chirp" effect in the arrival time of the electrons with different energies within the pulse leads to a pulse *compression* during the space-charge lifetime.

d) The space-charge effect is over, the electron pulses undergo the diffraction process, without being affected by any external force.

The experimental results reported so far indicate that we can really see space-charge dynamics on the picosecond scale by observing the effects that the space-charge induces on the scattered electron pulses.
In particular two effects may help to highlight the space-charge generation and temporal evolution: the spectrum energy shift (Fig. 28a) and narrowing (Fig. 29b). The former will be discussed in the next section, where a simple but effective model will be presented, while more information regarding the latter will be obtained with pump fluence dependent measurements (section 6.4).

6.3 Space-charge model

We tried to simulate the space-charge induced energy shift using a model based on simple electron dynamics. The pump laser beam was assumed to generate a disc of charge in front of the Cu(111) surface by photoelectric effect. Since the photon energy (1.55 eV) is smaller than the copper work function (4.94 eV [63]), multi-photon absorption is required.

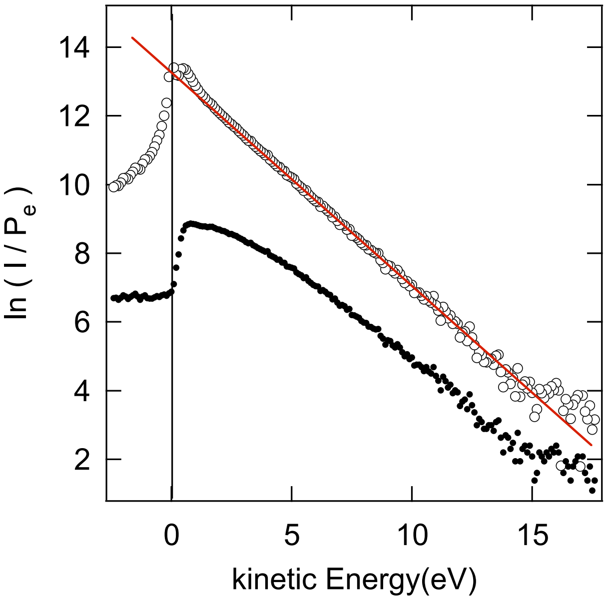

Figure 30: *Logarithmic hot electron spectrum of a* 3.2 µJ, 100 fs *laser pulse hitting a Cu(111) surface. If the spectrum (black dots) is normalized with the electron emission probability P_e [42], a perfect Boltzmann distribution with a thermal energy $k_B T$ of* 1.6 eV *is found for energies* 1.3 eV *above the vacuum level.*

The energy distribution of these electrons is shown Fig. 30: the spectrum, shown in black dots, was measured at normal emission in a separate experiment utilizing with the same pump laser energy of 3.2 µJ/pulse as in the time-resolved experiment. If the spectrum is normalized with the electron emission probability $P_e = \sqrt{E_k - E_v}$ [42], where E_k is the kinetic energy and E_v the vacuum level, one gets a perfect Boltzmann distribution of the hot electrons, yielding a thermal energy $k_B T = 1.6\,\mathrm{eV}$ for energies 1.3 eV aboveE_v. Consequently the average electron velocity was determined to be $1.35 \times 10^6\,\mathrm{m/s}$.
In the simulations we assumed that this charge distribution has a radius R equal to the laser beam waist and a uniform charge density $\rho(z)$ that evolves in time in the direction z perpendicular to the sample surface by increasing its thickness with a velocity given by the hot electron energy distribution (see Fig. 31a).
For simplicity we neglected lateral expansion; under this assumption we can consider the model valid for a thickness of the electronic distribution smaller than its diameter. After its generation the electron cloud expands out of the surface with a constant total charge, but a time-dependent charge density.
Fig. 31b shows the evolution of the charge density ρ along z as a function of time after

its generation ($t = 0$) on the sample surface ($z = 0$).

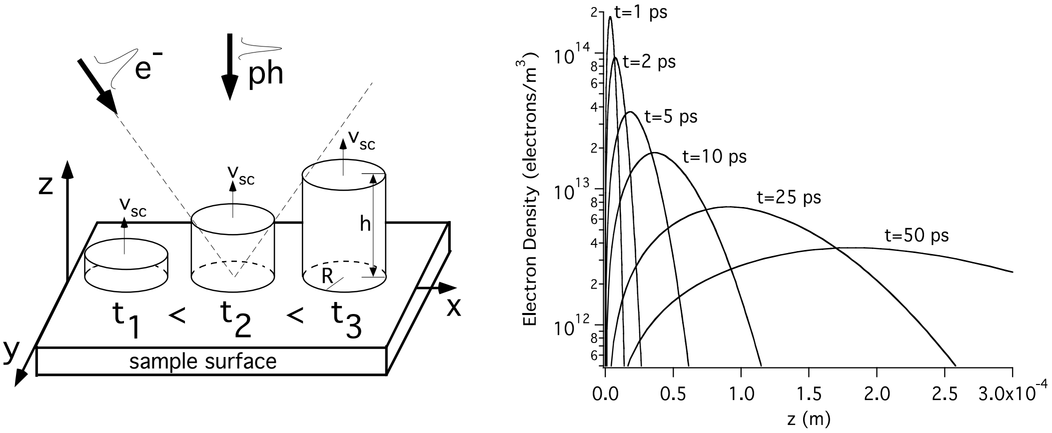

Figure 31: *a) Sketch of the model geometry: a disc of charge of radius R generated by the pump laser beam propagates out of the surface only in the z direction, increasing its thickness h according to the velocity v_{sc} given by the electron energy distribution. The electron pulses come onto the sample with an angle of incidence of* $45°$ *and they pass across the evolving disc of charge during the diffraction process b) Evolution of the electron density ρ along z at different times after its creation ($t = 0$) at the sample surface ($z = 0$).*

The motion of the probe electron of charge $-e$ located at a certain delay at a distance z_0 above the grounded Cu(111) plate is perturbed by the electric field generated along the z axis by the charge distribution $\rho(z)$:

$$E_z = \int \frac{\rho(z)}{2\epsilon_0}\Big(1 - \frac{z_0}{\sqrt{z_0^2 + R^2}}\Big)\, dz \tag{13}$$

where ϵ_0 is the electric field constant and R the radius of the space-charge disc.

In order to fulfill the requirements imposed by the Gauss' theorem, we used the method of the image charges by replacing the metal surface with a charge $+e$ located at a distance $-z_0$: this arrangement will produce the same electric field at any point above the metal plate and satisfies the boundary condition that the potential along the plate must be zero.

The energy shift of the incoming electron pulses is calculated as a function of the delay considering the angle of incidence equal to 45° but assuming for simplicity monochromatic electrons of 55 eV. For each delay the electric field given by Eq. (13) is calculated considering also the image charge. Then the equation of motion for the electrons passing across the space-charge region is solved.

Fig. 32 shows the comparison between the theory and the experimental data: the total

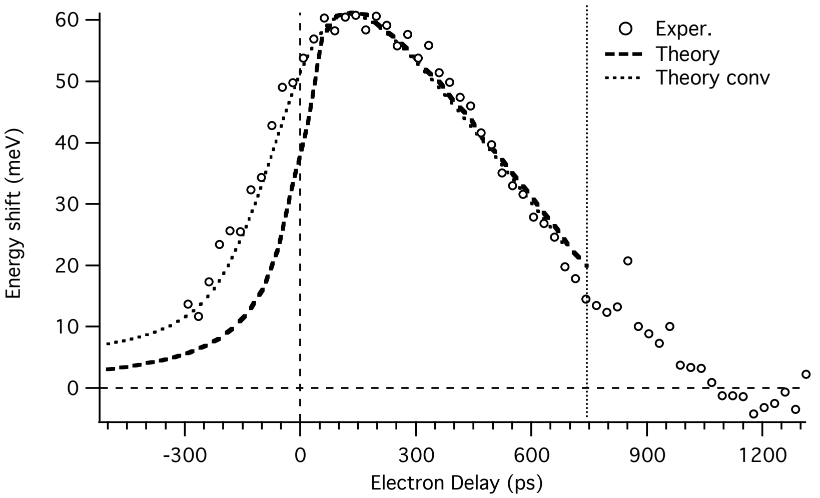

Figure 32: *Kinetic energy gain of electrons in presence of pump beam as a function of the time delay. A maximum shift of* 60 meV *occurs close to coincidence. The dotted line is the convolution of the theoretical dashed line with a* 110 ps *wide Gaussian profile, introduced to take into account the instrumental time resolution. The good agreement between the experimental data and the theory indicates that the simple model presented can explain the observed effect. The vertical dotted line at a delay of about* 750 ps *after coincidence represents the limit till which the proposed model holds, the thickness of the space-charge electronic distribution being smaller than its diameter.*

number of photoelectrons in the charge density and the radius R were left as free parameter in the fit, while the temperature of the hot electron gas (i.e. the photoelectron energy distribution) was set as a constraint and kept fixed at the measured value of $k_BT = 1.6\,\mathrm{eV}$. With a total charge of 7.9×10^7 electrons and a disc radius of 0.3 mm the delay and the amplitude of the maximum energy shift are well reproduced. It has to be noted that the deduced values are in good agreement with the measurements of these quantities realized with independent experiments: a total charge of 7×10^7 photoelectrons per was estimated by analyzing the normal emission Cu(111) spectrum shown in Fig. 30, while the pump laser spotsize was estimated to be roughly 0.25 mm for the same optical path length. The agreement between the experimental and the simulated curves is less accurate in the time region before the delay where the maximum shift occurs: the theory predicts a faster space-charge onset. However this deviation may be due to the instrumental time resolution. Indeed the convolution of the theoretical curve with a 110 ps wide Gaussian profile returns a corrected trend which fits well with the experimental data also in the region before the maximum shift as indicated by the dotted line in Fig. 32.

The utilized 110 ps wide Gaussian may be considered a reliable estimation for the instrumental time resolution for the present experiment where 55 eV electron pulses hit the sample surface with an angle of incidence of 45°.

In Fig. 32 the vertical dotted line positioned about 750 ps after coincidence represents the temporal limit below which the proposed model for the electronic space-charge dynamics holds, the electronic distribution thickness in the direction perpendicular to the surface being smaller than its dimension in the direction parallel to the surface.

The simple space-charge model presented here is not able to predict the energy spectrum narrowing observed in the 300 ps time interval after coincidence (Fig. 29). As expected if the diffraction process is simulated with two different primary energy of 54.1 eV and 56.8 eV, the position of the maximum shifts by less than 4 ps.

Most likely the electron-electron interaction that was not included in the space-charge model is the main responsible for the observed peak narrowing effect. In order to prove this, delay scans were performed at different space-charge electron densities; the latter may be controlled by varying the pump laser fluence.

6.4 Pump fluence dependence

The emission of the photoelectrons which constitute the space-charge effect is a non-linear process which strongly depends on the pump laser fluence. A series of measurements performed varying the pump laser fluence may give more insight into the space-charge effect. For instance, the kinetic energy shift of the diffracted electrons in presence of the pump beam and the energy spectrum width narrowing may be disentangled if the dependence of these effects on the pump laser fluence is studied.

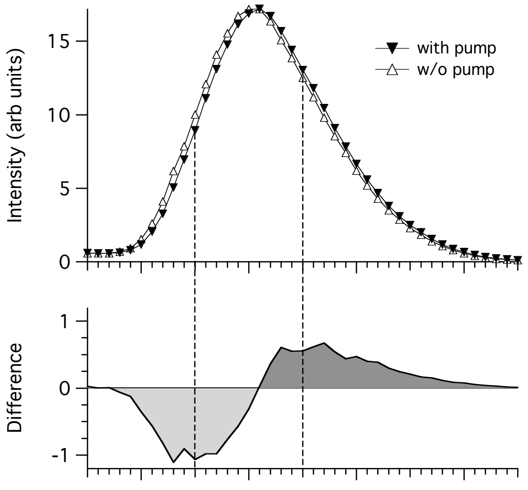

Figure 33: *Energy spectra of the specular spot of the Cu(111) crystal irradiated with pump laser pulses of a fluence equal to* 1.9 mJ/cm^2. *The spectra with and without pump are shown, together with the difference between the two curves (bottom panel). The dashed lines mark the energies at which the delay-dependent asymmetry scans presented hereafter were taken.*

For all the following set of measurements the electron beam primary energy was set to $E = 60\,\mathrm{eV}$ and the 400 nm wavelength laser pulses, used to generate the probe electron pulses, was limited to 2 nJ/pulse. The latter value is well below the cathode space-charge limit, determined to be at about 3 nJ/pulse (see section 3.4.3 for details).
Fig. 33 shows energy spectra of the Cu(111) specular spot, measured without and with pump laser. The pump fluence was $1.9\,\mathrm{mJ/cm^2}$. The calculation of the difference between the two curves allows to select at which energy the energy shift is maximum. For all the following delay scans the displayed asymmetries were measured at two fixed energies: $E = 59.5\,\mathrm{eV}$ and $E = 60.5\,\mathrm{eV}$.

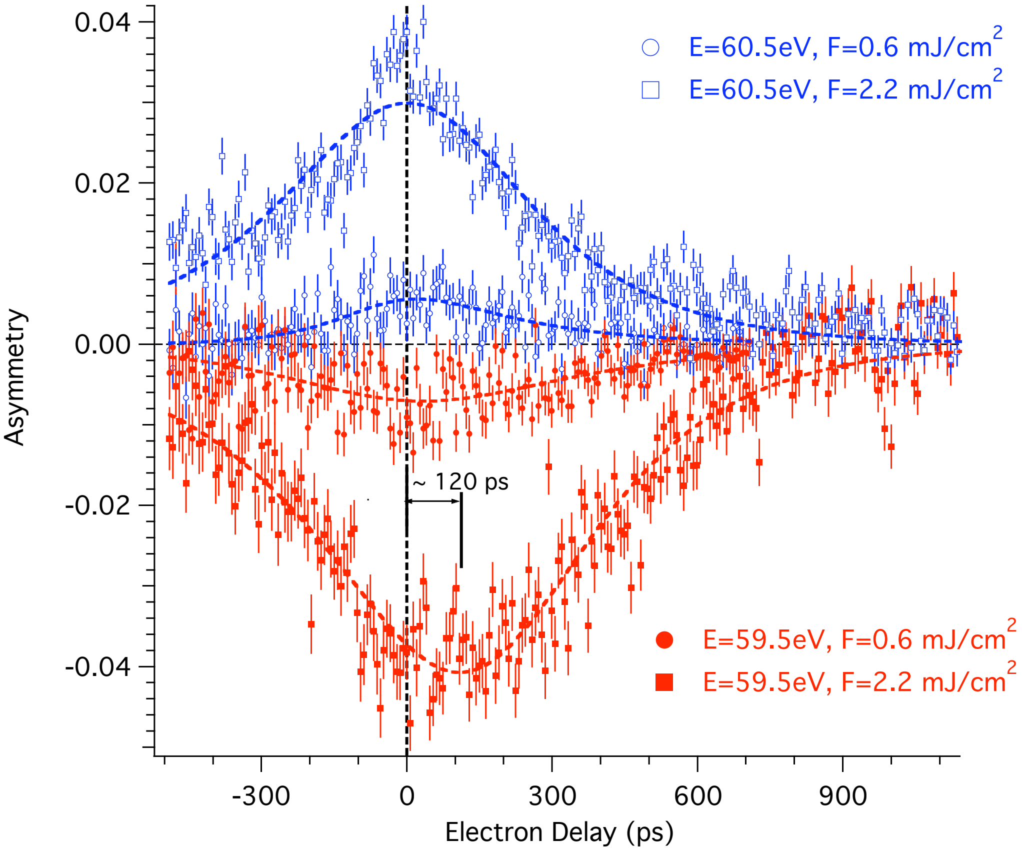

Figure 34: *Direct comparison between two sets of delay scans, realized at laser fluences of* $2.2\,\mathrm{mJ/cm^2}$ *(squares) and* $0.6\,\mathrm{mJ/cm^2}$ *(circles). For the high energy scan (*$E = 59.5\,\mathrm{eV}$*, open symbols) the signal maximum is observed at coincidence; for the low energy asymmetry (*$E = 59.5\,\mathrm{eV}$*, solid symbols) the signal minimum shifts about* 100 ps *towards negative electron delays, approaching the coincidence delay.*

Fig. 34 shows the comparison between two sets of asymmetries recorded for different pump laser fluences. The high fluence scans ($2.2\,\mathrm{mJ/cm^2}$) resemble those displayed in Fig. 29a: for the low energy scan, the minimum of the curve is detected about 100 ps *after* coincidence. As expected in the low fluence scans ($0.6\,\mathrm{mJ/cm^2}$), the signal lifetime is much shorter and its intensity lower, indicating a much smaller space-charge induced energy shift. Furthermore no time interval between the high energy scan maximum and the low energy scan minimum is observed: in the low fluence regime, the temporal coincidence is detected at the same delay.

Apparently, a reduction of the pump laser fluence by almost a factor of 4 induces no effect on the delay position of the high energy scan maximum (defined as delay zero), but causes a 100 ps time shift for the low energy scan minimum. This observation indicates that not only the kinetic energy shift intensity, but also the dynamics of the probe electrons during the interaction with the space-charge distribution are strongly dependent on the the pump laser fluence.

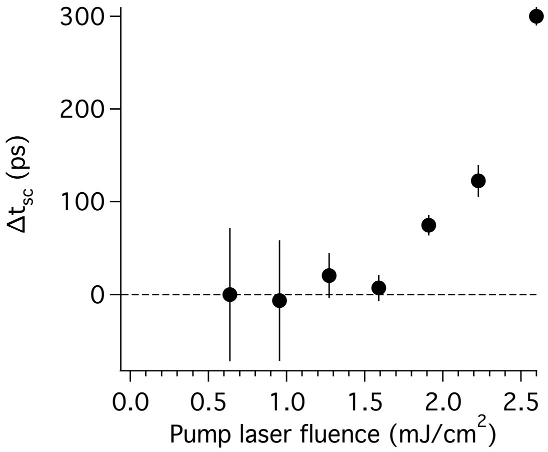

Figure 35: *Space-charge interaction time Δt_{sc} as a function of the pump laser fluence. Δt_{sc} is defined as the time interval between delay zero and the delay where low energy asymmetry reaches its minimum.*

Be the space-charge “interaction time” Δt_{sc} defined as the time difference between the high energy delay scan maximum and the low energy delay scan minimum. As displayed in Fig. 29 this is the time interval during which the energy spectrum of the scattered electrons gets narrower, besides being shifted towards higher kinetic energy values.

Fig. 35 shows the evolution of Δt_{sc} as a function of the pump laser fluence. Two clear different trends for Δt_{sc} can be identified: for fluences below a threshold of about $1.5\,\mathrm{mJ/cm^2}$ the value of Δt_{sc} is basically zero, meaning that low energy electrons are affected by the space-charge onset only by a small energy gain but their energy distribution is not modified. After the threshold Δt_{sc} increases almost exponentially: the stronger the space-charge effect is, the longer it reduces the energy width of the spectrum.

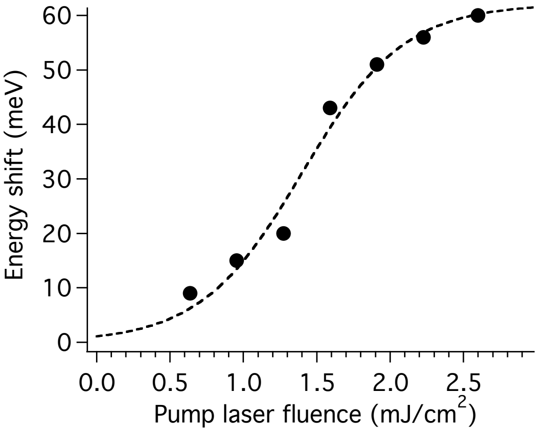

Figure 36: *Energy gain of* 60 eV *electron pulses measured at coincidence as a function of pump laser fluence: a fit with a sigmoid function returns a saturation level of* 62 meV.

Besides the interaction time Δt_{sc}, also the kinetic energy gain of the probe electrons in presence of the pump light may be monitored as a function of the pump laser fluence. Fig. 36 shows the maximum energy shift as a function of the pump laser fluence.

As expected, the shift in energy increases with increasing fluence, but it likely reaches a saturation limit. A fit with a sigmoid function defined as

$$f(x) = \frac{A}{1 + e^{\frac{x_0 - x}{\tau}}} \tag{14}$$

results in an upper limit $A = 62\,\mathrm{meV}$.

The results shown here confirm that the energy spectrum narrowing effect and the non-linearity of the energy gain are due to the interaction between the electrons of the pulses and the electrons of the space-charge cloud. Up to a certain pump laser fluence this electron-electron interaction may be neglected and only a slight *rigid* energy shift of the diffracted spectrum is observed. When the space-charge electron density is large enough, the electron-electron interaction starts to play an important role and the presented effects are observed.

6.5 Conclusions

The results discussed in this chapter show clearly that in view of the realization of a time resolved photon-pump low-energy-electron-probe experiment one has to deal with different side effects which might hide the desired signal. In particular, using electron pulses with kinetic energies lower than 100 eV as a probe, the pump induced surface space-charge effect has to be taken into account. As a matter of fact the space-charge and the diffraction process time constants are in the same order of magnitude when low energy electrons are used.

Therefore a detailed study of this phenomenon permits to discriminate changes due to true surface structural dynamics from those related to the space-charge, which shifts the electron energy distribution curves, inducing an apparent LEED spot intensity variation. We could nail down two main space-charge induced transient effects: a shift and a change in width of the electron energy spectrum. The former can be understood by simulating the scattering process of a monochromatic electron beam from a surface irradiated by the pump laser, which generates a cylindrical density of photoelectrons outside the surface. The latter is observed only when space-charge electron densities of the order of 10^8 photoelectrons are generated, when more complicated non-linear effects take place during the scattering process; most likely the electron-electron interaction between the incoming electron pulses and the electrons in the space-charge cloud is responsible of measured narrowing of the diffracted energy spectra.

In conclusion these experiments allow for the determination of the maximum pump laser fluence which can be used to irradiate the sample surface in order to induce some transient structural change, while avoiding the generation of space-charge effects which modify the electron pulses. Such a threshold can be set close to $1.5\,\mathrm{mJ/cm^2}$.

7 Time-resolved LEED

The goal of a time-resolved Low Energy Electron Diffraction (t-LEED) experiment is the *real time* observation of surface structural changes. Basically the idea is to exploit the surface sensitivity and the relatively easy experimental setup of the LEED technique, presented in Chapter 4, together with ultrafast laser pump-probe technique, described in Chapter 5.

Equipped with a pump-probe setup the LEED technique has the potential to resolve structural surface dynamics, like for instance rotations or vibrations of adsorbed molecules, which can be the responsible of order-disorder surface phase transitions. For the successful realization of the experiment one needs to convert laser pulses into electron pulses, send them onto the sample surface and detect them after the diffraction process has taken place. The change of the sample electron reflectivity as a function of the delay between the pump laser and the probe electron pulses should eventually reveal transient changes happening on the sample surface.

While in principle the t-LEED experiment looks simple and easily feasible, in reality it is much more complicated. Actually up to date, still no direct observation of surface dynamics obtained utilizing low-energy electron pulses has been ever reported in literature. It is worth mentioning some of the constraints that have to be fulfilled during the long way towards the realization of a first proof-of-principle for t-LEED experiments:

- The electron gun used to convert laser pulses into electron pulses has to be designed so that the electron beam energy is high enough to permit the collection of good quality LEED pattern in a reasonable time and the electron pulse time width at the sample position is narrow enough to ensure a good experimental time resolution. These issues have been discussed in Chapters 3 and 5, where it was concluded that a time resolution smaller than 35 ps at 55 eV can be achieved in the best case, using the novel design home-built high flux electron gun.

- The temporal and spatial overlap of the two pulses have to be accomplished; this is not a trivial task, since the electron beam propagating out of the gun head is not easily detectable at the sample position. However the simple method for cross-correlation of electron and laser pulses formerly developed in our group [22] and presented briefly in Chapter 5, can solve this problem and provide a reference delay where the signal from the crystal surface is expected.

- The low kinetic energy of the probe pulses (generally smaller than 70 eV) presents the drawback that the electrons are much more affected by the space-charge effects, induced on the sample surface by the pump laser. Consequently the signal

> of effective structural changes may be hidden by the space-charge effect and the disentanglement between the two signals may result too complicate. In Chapter 6 it was shown that it is possible to set a threshold in the pump laser fluence, below which the space charge effect is negligible and the probe electrons are no longer affected; in these conditions, all the transient changes carried by the electrons after the diffraction can be assigned to specific sample structural modifications.

The last consideration brings out another important issue, regarding the choice of the appropriate system, which is suitable to be studied by means of a t-LEED experiment: actually it is not easy to find a system exhibiting fully reversible structural changes large enough to be detected within a small temperature range. In fact the constraint of using low fluence pump pulses has the consequence that a small quantity of energy per pulse is deposited on the sample surface and thus the induced effect gets very small.

All the pump-probe results presented further and in the previous chapters were obtained exploring the dynamics of C_{60} monolayer or multilayers deposited on the (111) surface of a metal, namely silver or copper. As a first characterization the response of this system upon highly intense pulsed laser irradiation was studied.

7.1 Stability of photo-excited C_{60} adsorbed on Ag(111)

For pump-probe studies, it is desirable that the lifetime of the system under investigation is long enough, since a complete delay scan may take several hours. In a standard pump-probe experiment, during this time the sample surface is irradiated with intense laser pulses, which can reach a peak intensity as high as $500\,\mathrm{GW/cm^2}$. In the case of C_{60} molecules adsorbed on Ag(111), such a strong energy deposition per unit area may cause a local desorption of the C_{60} molecules or their disproportionation; this represents a non-reversible process that would alter the properties of the exposed surface area, rendering our experiment not feasible, since in the present stage our experimental setup doesn't allow one-shot measurements.

In order to test the stability of the system against pump laser illumination, one monolayer of C_{60}/Ag(111) was probed in a normal emission photoemission experiment. The multiphoton-photoemission spectrum was recorded applying some biasing voltage to the sample. The energy position of the vacuum level was monitored while the surface was irradiated by 800 nm wavelength photons with different pulse energies; the laser beam was highly focused, being the spot diameter of about 100 μm.

Fig. 37 shows the results of this experiment, performed on one monolayer of C_{60}/Ag(111) and on the clean Ag(111) surface as reference, during a total time of 70 minutes. After this period, no particular changes in the vacuum level position are discernible for the bare Ag(111) at any laser power and for the C_{60} monolayer for low laser pulse energies.

Actually the small fluctuations visible in Fig. 37a are likely due to laser or bias voltage instabilities.

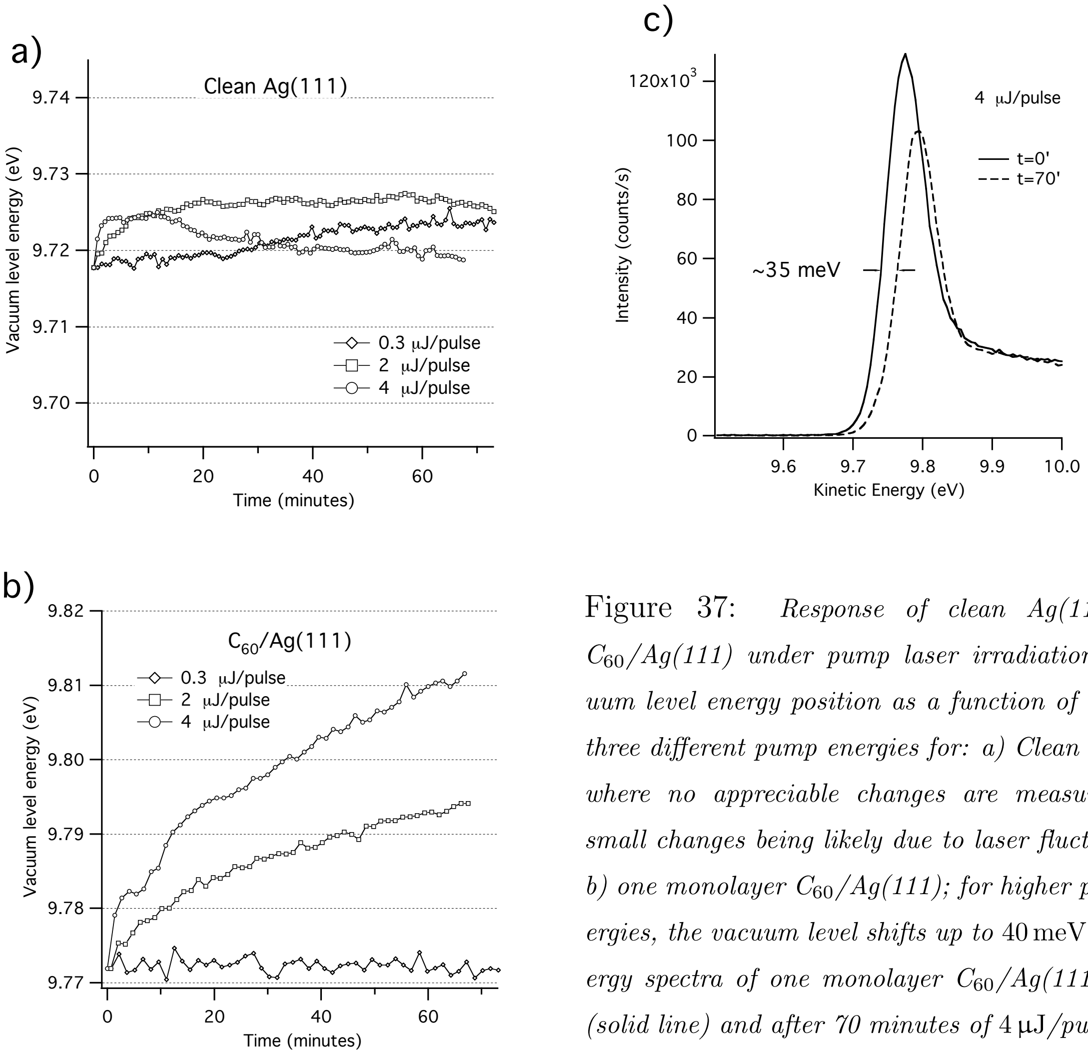

Figure 37: *Response of clean Ag(111) and C_{60}/Ag(111) under pump laser irradiation. Vacuum level energy position as a function of time for three different pump energies for: a) Clean Ag(111) where no appreciable changes are measured, the small changes being likely due to laser fluctuations; b) one monolayer C_{60}/Ag(111); for higher pulse energies, the vacuum level shifts up to* 40 meV*. c) Energy spectra of one monolayer C_{60}/Ag(111) before (solid line) and after 70 minutes of* 4 µJ*/pulse laser irradiation: an energy shift and a decrease in intensity occur.*

Instead, when the C_{60} monolayer on Ag(111) is irradiated with pulse energies larger than 2 µJ/pulse a clear energy shift and a decrease of the edge intensity become apparent, as can be seen in Fig. 37b and c, respectively.

A change in the vacuum energy position is most likely due to a local variation of the work function. The value of the work function was measured by means of Ultraviolet Photoemission Spectroscopy (UPS) with He Iα radiation, and resulted to be 4.68 eV and 4.73 eV for Ag(111) and C_{60}/Ag(111), respectively, in good agreement with the literature values [35, 37]. Therefore the adsorption of one monolayer of C_{60} induces an increase of the work function of 50 meV. A shift towards higher kinetic energies of the vacuum level would translate into an increase of the work function. The curves displayed in Fig. 37b indicate that the intense laser irradiation causes a partial damage of the C_{60} monolayer, leading to a larger value of work function.

It has to be noted that such surface degradation is local and limited to the laser spot size, which is much smaller than the He discharge lamp photon flux diameter. Therefore a comparison between two spectra of C_{60}/Ag(111) measured with UPS before and after the laser irradiation would show no peculiar differences.

In conclusion, when time-resolved experiments are executed on the C_{60} monolayer adsobed on Ag(111), the pump laser pulse energy should not exceed a value of about $1\,\mu$J/pulse, which for a laser spot size diameter of $100\,\mu$m translates into a fluence of $13\,\mathrm{mJ/cm^2}$. Nevertheless, with this laser fluence, still about 70 photons per laser pulse are striking a single C_{60} molecules, a number which should be sufficient to induce appreciable molecular excitations.

When multilayers of C_{60} are evaporated on metal surfaces, the former pump laser fluence limit has to be reduce further. This is indeed what was measured by Kusch and coauthors with a study on photo-excited C_{60} adsorbed on Ni(111) [64]: they observed that the desorbed ion yield is linearly dependent on the coverage only when multilayers of C_{60} were irradiated, while no desorption occurs for the single monolayer (most probably because of low laser peak intensity).

During routine experiments, the surface quality of the C_{60}/Ag(111) system was monitored by checking periodically the LEED patterns. The diffraction patterns were collected with the laser activated electron gun; the precaution of using the same electron source for the sample surface quality check and for the time-resolved experiments guarantees that indeed the same sample area was investigated. The result is that even after several hours during which the sample was irradiated with pump laser pulses below the limit deduced above, the diffraction spot intensities did not show any significant decrease. Therefore no indication of effective surface degradation was obtained.

7.2 C_{60} multilayer on Ag(111)

Pump-probe experiments performed on the C_{60} monolayer on Ag(111) and Cu(111) did not provide the expected results. No transient changes due to surface structural dynamics in the LEED spot intensity were obtained, even though the system was proved to be quite sensitive to small temperature variations, because the surface Debye temperature was estimated to be below 50 K (see section 4.3.1). Most likely the constraints imposed to the pump laser fluence by the space charge effect and the high reflectivity of silver and copper for radiation of $\lambda = 800\,\mathrm{nm}$ make that the energy coupling between the laser radiation and the C_{60} film and thus the deposited energy per pulse is not enough to enhance molecular vibrations.

Therefore we moved towards a system exhibiting a larger Debye-Waller effect: C_{60} multilayers adsorbed on Cu(111). In addition it is known that the solid C_{60} crystal undergoes a first-order order-disorder phase transition at a temperature $T_B = 260\,\mathrm{K}$ [65]. Goldoni *et al.* [26] have shown that such a phase transition is initiated at the surface, since for the (111) surface of C_{60} it happens at a temperature of $T_S = 225\,\mathrm{K}$, when the surface structure changes from (1×1) to (2×2) [66]. This phase transition is assigned to the "freezing" of the quasispherical C_{60} molecules, which stop rotating around their center below T_S. The higher degree of order of $C_{60}(111)$ in the low temperature phase is proved by the surface structural change and can be observed by LEED with the appearance of additional diffraction spots, as displayed in Fig. 38, taken from reference [26].

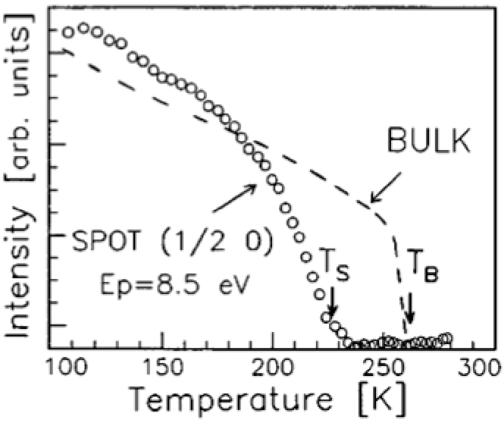

Figure 38: *Intensity of the* $(1/2, 0)$ *LEED spot as a function of T, measured at* $8.5\,\mathrm{eV}$*: the fractional-order diffraction spot disappears at temperatures higher than* $T_S = 225\,\mathrm{K}$ *(from ref. [26]).*

A thick film of ordered C_{60} shows the same properties of solid C_{60} crystal; indeed in electron diffraction experiments utilizing low energy electrons, the escape length is of the order of the molecular diameter, so that most of the diffraction signal comes from the first layers.

Such a system would represent an ideal case to be studied by means of t-LEED. In principle, the sample is kept at a temperature few degrees below T_S and is positioned in such a way that one of the fractional-order LEED spot enters the aperture of the electron energy analyzer. The pump pulses impinging onto the molecules would deposit enough energy to make them rotate, so that the symmetry is broken and the diffracted spot vanishes.

The fullerene films were grown on Ag(111) at a low evaporation rate of about 0.04 ML per minute and keeping the substrate at 400 K. The thickness of the multilayer was calibrated via XPS examining the intensity of the C1s and Ag3d peaks. According to the literature, this recipe would guarantee a highly ordered C_{60} film growth [67].

When more than a monolayer is evaporated on Ag(111), the resulting diffraction pattern is given by a $(2\sqrt{3} \times 2\sqrt{3})R30^\circ$ commensurate structure and two additional structures rotated by ±14° [33, 35]. In the present study we found that such LEED pattern is visible only at low energies, below 70 eV. This may be due to the fact that electrons with higher energy (shorter wavelength) are more sensitive to the random orientation of the C_{60} molecules than electrons with low energy [66]: thus, the diffraction pattern is visible only for low electron energies.

At higher energies, the LEED spots quench together and only an intense background is visible. This situation gets even worse, when the laser activated electron gun is used, because the LEED spots are broader and the background more intense due to the not perfect collimation of the beam: at room temperature no discernible diffraction spots were visible already at energies higher than 20 eV.

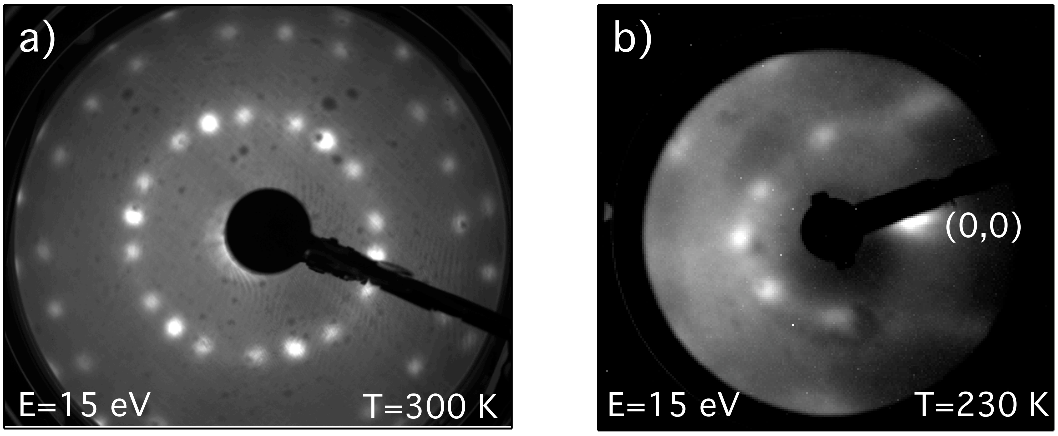

Figure 39: *LEED patterns of C_{60} multilayer on Ag(111), recorded at* 15 eV *with two different electron sources: a) with a standard electron gun, at normal incidence, at room temperature b) with the laser activated electron gun, close to specular incidence, at* 230 K *(*30 s *exposure time).*

Fig. 39 shows the diffraction patterns of C_{60}/Ag(111) when the C_{60} coverage was about 3 monolayer. On the left-hand-side, the LEED pattern at 15 eV is collected with a standard LEED apparatus at normal incidence. The $(2\sqrt{3} \times 2\sqrt{3})R30^\circ$ structure is the majority phase but consistent amount of the $R \pm 14^\circ$ phases are present, so that the first "ring" of diffraction is composed by 6 not-equivalent beams, making a total of 18 diffraction spots.

On the right-hand-side of Fig. 39 the LEED pattern is collected with the laser activated gun at 15 eV. As already presented elsewhere (see section 2.2), the 90° angle between the gun and the detector allows the measurements of normal incidence LEED pattern when the sample is tilted about 45° with respect to electron beam; this is the reason why the ring of diffraction spots is not circular around the (0,0).

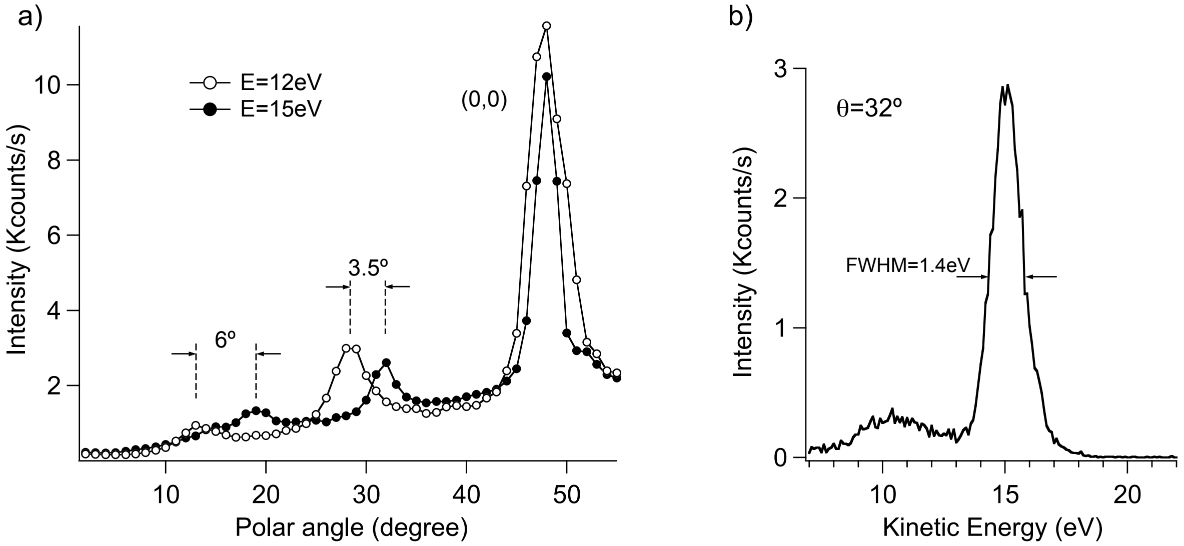

Figure 40: *a) Polar scan across the specular spot along the* $(1, 1/2)$ *direction for* 12 eV *(open circles) and* 15 eV *(solid circles). b) Energy spectrum of the* $(1/3, 1/6)$ *LEED spot, measured at a polar angle of* 32° *at* 15 eV.

In the same way as in the other experiments reported before, the sample was tilted so that the diffracted spots were directed into the entrance of the electron energy analyzer. Fig. 40 shows the LEED spots recorded with the analyzer. In order to have the correct assignment of the LEED spots, polar scans over a range of more than 50° were measured at two different energies: this procedure permits to nail down unambiguously the position of the specular spot. As expected the LEED pattern shrinks towards the (0,0), whose maximum in intensity is located at an incident angle of 48°. Fig. 40b shows the energy spectrum at 15 eV of one of the diffraction spots belonging to the first ring close to the specular.

In order to obtain the response of the C_{60} multilayer to temperature changes, we have measured the temperature dependence of a fractional order spot of the C_{60}/Ag(111) LEED pattern. Fig. 41 shows the intensity of the $(1/3, 1/6)$ spot as a function of temperature. Two regimes characterized by different slopes in the intensity drops are observable and the transition between the two phases can be set quite close to the surface

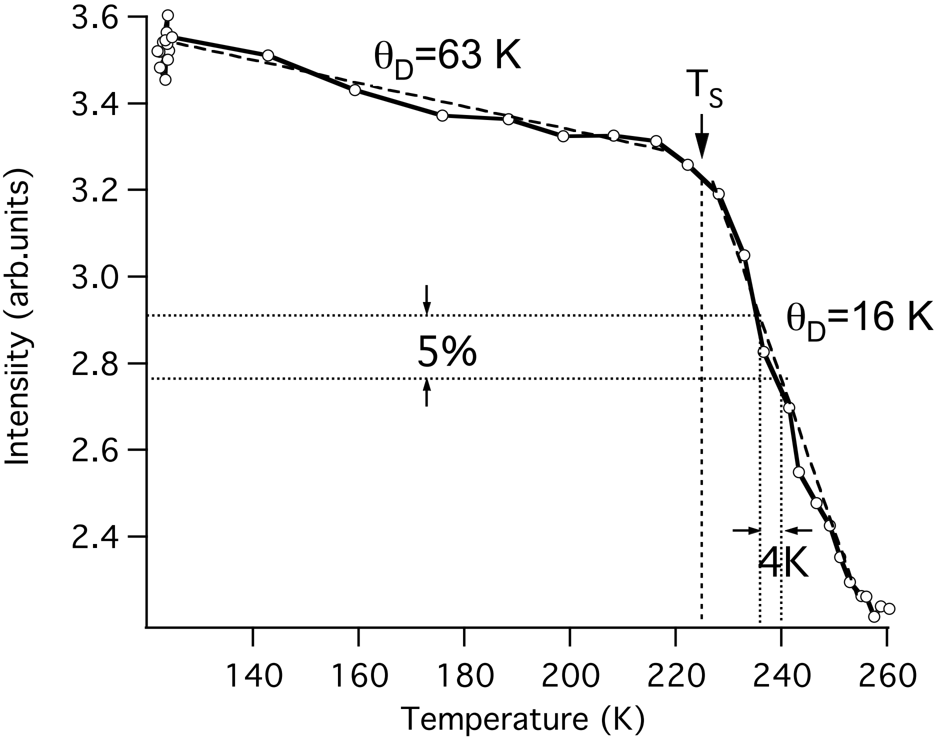

Figure 41: *Debye-Waller curve for the* $(1/3, 1/6)$ *spot of* C_{60} *multilayer on Ag(111) LEED pattern at* 15 eV*. For temperatures higher than* $T_S = 225\,\mathrm{K}$*, the intensity drop is quite steep, resulting in a very small surface Debye temperature* Θ_D *of* 16 K*: in this phase an intensity drop of 5% corresponds to a temperature increase of only* 4 K*.*

phase transition temperature $T_S = 225\,\mathrm{K}$.

In the high temperature phase the surface Debye temperature is only 16 K; this means that the system is particularly sensitive to small temperature variations. A change of only 4 K of the sample temperature would be registered as a decrease of 5% in the LEED spot intensity.

It has to be noted that the curve displayed in Fig. 41 is quite different to the one obtained by Goldoni *et al.* for the $(1/2, 0)$ superstructure spot (see Fig. 38). In our case we evaporated on Ag(111) no more than 3 layers of C_{60}, therefore the film thickness is too small to observe a LEED pattern of an ordered $C_{60}(111)$ surface. Nevertheless, utilizing electrons with an energy as low as 15 eV, we can investigate only the topmost layer of molecules and obtain apparent informations about their motion.

7.3 t-LEED from C_{60} multilayer on Ag(111)

Time resolved LEED experiments were performed on a diffraction spot of C_{60} multilayer at a temperature $T = 230\,\mathrm{K}$, where the spot intensity is still high and the slope of the Debye-Waller curve, shown in Fig. 41 is steep. At this temperature most of the C_{60} molecules are not allowed to rotate freely around their vertical axis. Therefore we expect to transfer with the pump pulses enough energy to the molecules to induce their motion, and follow this surface structural change by monitoring the diffraction spot intensity variations.

In order to limit the pump laser fluence below the threshold where space-charge effects become negligible, we adopted the strategy of increasing the laser spot size, instead of reducing its power. This approach bears the further advance that the spatial overlap results more easily achieved.

For the $(1/3, 1/6)$ superstructure spot, the normalized integrated LEED intensity shows at coincidence an effect close to 2%, when the C_{60} multilayer is irradiated by pump laser pulses of fluence $0.15\,\mathrm{mJ/cm^2}$ (Fig. 42). The comparison of energy spectra collected at coincidence and off coincidence (Fig. 42a-b) shows an apparent loss of intensity when electron and light pulses reach the sample at the same time. Such temporal coincidence was determined by using the method presented in section 5.2, based on the space-charge effect on a metal pinhole: to perform this measurement the pump laser was focused more to increase the fluence and produce the space-charge cloud.

The electron-photon cross correlation curve yields an upper limit of time resolution of 420 ps. This value indicates how difficult it is to achieve a picosecond time resolution in a t-LEED experiment, when electron pulses of 15 eV are used and the angle of incidence is about 30° with respect to the sample normal.

The observation that the t-LEED curve minimum occurs exactly at coincidence suggests that the measured intensity decrease is not referred to the space-charge effect. In fact, in Chapters 5 and 6 it was shown that the space-charge related effects are detected a few hundreds of picosecond *after* coincidence (see Fig. 25 and Fig. 26 for comparison); indeed also in Fig. 42 the pinhole correlation curve, based on space-charge effect, shows its minimum about 500 ps after coincidence.

Moreover the spectra with and without pump measured at coincidence clearly indicate that the loss of intensity is *not* energy dependent like in the case of space-charge.

Most likely we can really observe molecular dynamics induced by the pump laser pulses: before coincidence, at $T = 230\,\mathrm{K}$, the C_{60} molecules have not enough energy to rotate freely. At coincidence, the energy transferred by the pump pulses is enough to induce a 2% decrease of the LEED spot intensity, which correspond to a temperature raise of

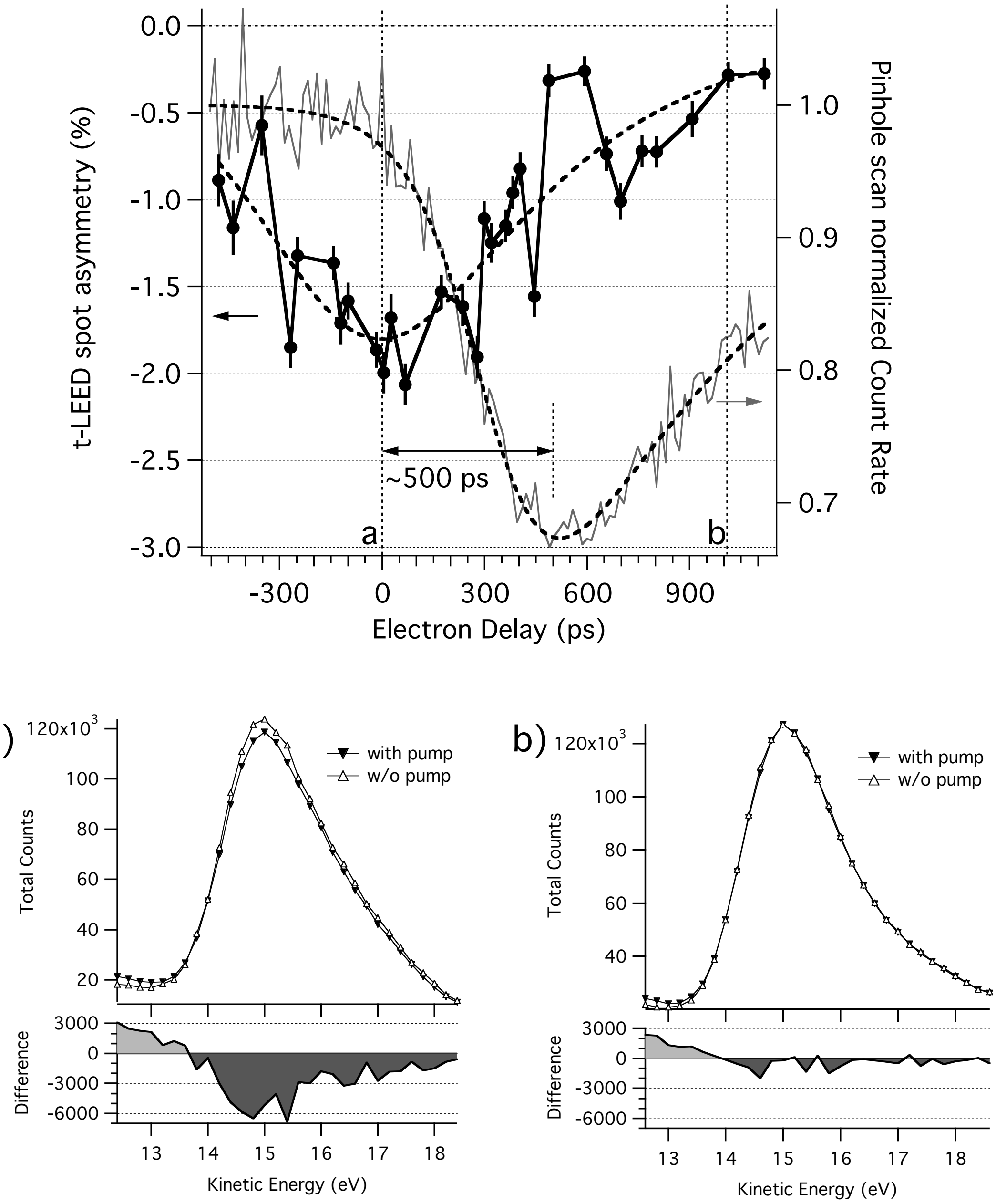

Figure 42: *Top: normalized integrated LEED spot intensity for the* $(1/3, 1/6)$ *spot as a function of delay, at* $15\,\mathrm{eV}$ *and* $230\,\mathrm{K}$ *(solid circles). An apparent loss of counts is recorded at temporal coincidence. The latter is determined with the pinhole correlator (see section 5.2), the correlation curve of which is displayed in light gray. Bottom: energy spectra with and without pump at coincidence (dashed line 'a' in the top graph) and off coincidence (around* $1\,\mathrm{ns}$ *after coincidence, dished line 'b' in the top graph). The bottom panels show the difference between the two curves. The pump laser fluence was* $0.15\,\mathrm{mJ/cm^2}$.

about 3 K. After coincidence, the rotation of the molecules gradually stops and the system relaxes towards the equilibrium.

The drop of the spot intensity can be converted into the surface temperature raise using the the curve of Fig. 41 for calibration.

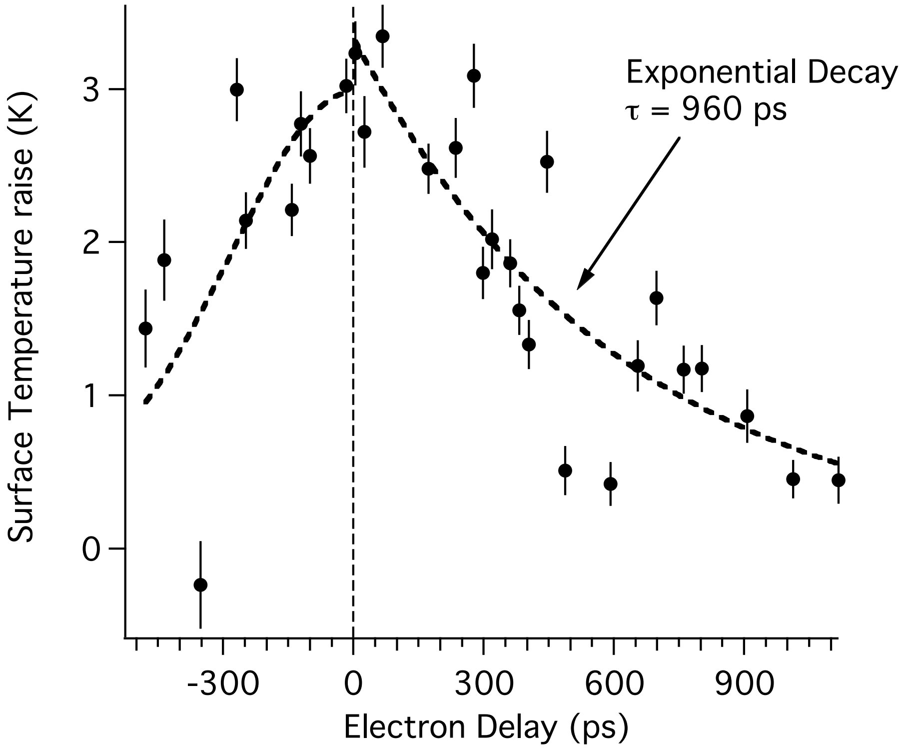

Figure 43: *Surface temperature raise after conversion of the LEED spot intensity drop (Fig. 42) with the Debye-Waller curve measured in the high temperature phase (Fig. 41): the fit of the relaxation process towards equilibrium yields a time constant* $\tau = 960 \pm 130\,\mathrm{ps}$.

Therefore the temporal evolution of surface temperature can be obtained (Fig. 43) and an exponential fit of the data after coincidence yields the time constant of the relaxation process. For the data set of Fig. 43 the time constant is 960 ± 130 ps.

In order to prove the reproducibility of the experiment, another t-LEED scan on the same LEED spot was performed after a complete new sample preparation. The temporal coincidence was moved towards smaller electron delays by changing the pump laser optical path, in order to investigate more in detail the delay region up to 1.3 ns after coincidence.

Like in the delay scan shown in Fig. 42, the minimum of the normalized LEED spot integrated intensity is found at coincidence, defined by the electron-photon cross correlation curve as the delay where the normalized intensity starts dropping. The phase transition time constant resulted to be $1020 \pm 110\,\mathrm{ps}$, consistent with the first measurement, even though the induced temperature raise was almost twice bigger, being in the order of $5\,\mathrm{K}$ (5% LEED spot intensity decrease). This may be due to small differences in the C_{60} multilayer quality.

It has to be noted that further experiments were performed in the low temperature phase, below T_S (Fig. 41): no transient changes related to any pump laser induced molecular motion was observed up to laser fluences of $0.5\,\mathrm{mJ/cm^2}$. Like in the case of the C_{60} monolayer on metal substrates, the energy coupling between laser light and the molecules is not enough to enhance detectable surface structural changes.

The experiments reported here constitute the first proof-of principle for time resolved LEED. The very low electron energy, which is necessary to use in order to see well defined diffraction patterns, worsens dramatically the experimental time resolution. This prevents the observation of possible coherent motion of the molecules, like in-phase layer vibrations or rotations. Indeed, these motions are known to happen within periods of few picoseconds. Nevertheless the collective response of molecular systems can be studied on a longer time of scale; this permits to deduce key parameters of structural changes like phase transitions relaxation times, which are in the order of nanoseconds.

The measured time constant can be used to understand how the C_{60} film reacts upon the laser induced heat transfer. Heat conduction is the transfer of heat from warm areas to cooler ones, and effectively occurs by diffusion; in the present case we consider for simplicity that the heat diffusion takes place from the surface only in the direction z perpendicular to the surface, with a heat flux $\dot{Q}$ given by (Fourier's law):

$$\frac{\partial Q}{\partial t} = -kA\nabla_z T \tag{15}$$

where k is the thermal conductivity, A the area of the heated region ∇T is the temperature gradient. With the assumption that $\nabla_z T \sim \Delta T/d$, where ΔT is the temperature raise and d the depth up to which the heat diffuses, than Eq. (15) becomes

$$\frac{\partial Q}{\partial t} = -kA\frac{\Delta T}{d} \tag{16}$$

Furthermore $Q = C\rho V\Delta T$, where C is the specific heat, ρ the mass density and V the volume, which can be written as $V = Ad$. Plugging into Eq. (16) the expression of Q we obtain:

$$\frac{\partial \Delta T}{\partial t} = -\frac{k}{C\rho d^2}\Delta T \tag{17}$$

the solution of which is given by

$$\Delta T = \Delta T_0 + e^{-t/\tau} \tag{18}$$

with a time constant $\tau = Cd^2\rho/k$. Therefore, the evolution of ΔT as a function of time after a heat deposition, follows an exponential decay. This is exactly what is found experimentally (Fig. 43).

With the further assumptions that C, k and ρ for the C_{60} multilayer are the same as the literature value for bulk C_{60} and are constant over the small temperature raise of few degrees [68], we obtain a value of $d = 18\,\mathrm{nm}$.

This estimation is in good agreement with the value of light penetration depth into a copper crystal, which is in the order of 12 nm for 800 nm wavelength [69]. Therefore the observed raise of the surface temperature can be effectively assigned to a molecular motion consequent to a local heat transfer induced by the pump laser.

8 Conclusions and outlook

In this thesis space-charge and molecular dynamics were studied by means of time-resolved Low-Energy-Electron-Diffraction (t-LEED). LEED is a well established tool in surface science and is generally considered as the prime technique to study surface long-range order, thanks to its excellent surface sensitivity. Several attempts of endowing this tool within the frame of the time-resolved techniques were not successful. The main reason for that resides in the difficulty to get a satisfying experimental time resolution and a system which exhibits a surface structural change that can be triggered by light and followed in time.

Here we show the first proof-of-principle experiment for t-LEED which was realized on the system constituted by a C_{60} multilayer on Ag(111). Even though the achieved time resolution is in the order of few hundred picoseconds, long-lived photo-induced molecular rearrangements could be observed. In particular the order-disorder surface phase transition, known to happen at 230 K was triggered with photons and probed with electron pulses and its relaxation time was estimated to be about 1 ns.

On the long way towards the realization of the main t-LEED experiment, two particular issues were treated more in detail: the realization of a high-flux electron gun of novel design, to produce ultrashort electron pulses, and the observation of surface space-charge dynamics.

The conversion of laser pulses into electron pulses at the cathode of an electron gun through photoeffect and the propagation of such electron pulses towards the sample surface are key parameters which define both the experimental time resolution and duration. All the experiments presented in this thesis were realized using the in-house-built electron gun which was tested to provide pulses showing a measured energy width of 0.7 eV at 100 eV and a beam current of roughly 1 electron/pulse. This last value allows the recording of LEED pattern with standard signal-to-background ratio within a few seconds.

Equipped with this device, surface space-charge dynamics were first investigated. It was shown that the emission of electrons caused by the pump laser pulses impinging on a metal surface, induces quite intriguing effects to the 55 eV electron pulses, like a kinetic energy gain of up to 60 meV. Low energy electrons constitute the best tool to investigate these effects, since their average speed is in the same order of magnitude as the velocity of the space-charge electrons and therefore the interaction time is longer. We presented a theoretical approach based on simple electron kinematics, which is capable to model the observed energy shift and space-charge dynamics. Moreover, measurements performed at different pump laser fluences permitted to determine a threshold below which the electron pulses are no longer affected by the space-charge.

All the results presented in this thesis indicate that watching molecular dynamics in real time and on the picosecond scale by using low energy electrons is a realizable but challenging task. Here we have shown how one can deal with “standard” problems like laser instabilities, generation of electron pulses and their detection after the diffraction process, achievement of temporal and spatial overlap between photons and electrons, space-charge effects both on the sample surface and at the electron gun photocathode and so on. However, among the several systems which have been investigated with t-LEED, only one (C_{60}/Ag(111)) provided a reproducible laser-induced response, which could be assigned to effective molecular dynamics.

This means that at the present stage t-LEED is still a pioneering experiment, but the first encouraging results open the door for further developments which will render time-resolved experiments based on low-energy electron diffraction the standard tool to study surface structural dynamics.

In order to do that the main improvement has to deal with the experimental time resolution. The realization of t-LEED experiments at a geometry as close as possible to normal incidence conditions would help. Indeed, already a difference of 1° between the direction of the incident electron beam and the sample surface normal causes at 100 eV a time delay of 1 ps, resulting from different trajectories within the electron beam. However, in the actual experimental setup, LEED patterns are difficult to record at normal incidence: the intensity of the high-order LEED spot is too small, mainly because of the low electron flux. Higher pulsed beam currents can be attained working at higher laser repetition rate. For instance with a pulse repetition rate of 50 GHz, beam currents in the order of 80 nA can be achieved with laser powers below the cathode space-charge limit of 3 nJ/pulse.

Furthermore such a high electron flux would permit a better energy selection of the diffracted electrons, by decreasing the slit dimensions and the pass energy value of the electron spectrometer. Also these changes would help in boosting the temporal resolution down to few picosecond, thus allowing the real-time observation not only of collective molecular motion but also of coherent intermolecular modes, like vibration or rotations.

References

[1] C. V. Shank, *Investigation of Ultrafast Phenomena in the Femtosecond Time Domain*, Science **233**, 1276 (1986).

[2] J. C. Polanyi and A. H. Zewail, *Direct observation of the Transition State*, Accts. Chem. Res. **28**, 119 (1995).

[3] M. G. Evans and M. Polanyi, *Some applications of the transition state method to the calculation of reaction velocities, especially in solution*, Trans. Faraday Soc. **31**, 875 (1935).

[4] A. H. Zewail, *Laser Femtochemistry*, Science **242**, 1645 (1988).

[5] U. Höfer, I. L. Shumay, Ch. Reuss, U. Thomann, W. Wallauer, and Th. Fauster, *Time-Resolved Coherent Photoelectron Spectroscopy of Quantized Electronic States on Metal Surfaces*, Science **277**, 1480 (1997).

[6] M. Bonn, S. Funk, Ch. Hess, D. N. Denzler, C. Stampfl, M. Scheffler, M. Wolf, and G. Ertl, *Phonon- Versus Electron-Mediated Desorption and Oxidation of CO on Ru(0001)*, Science **285**, 1042 (1999).

[7] G. Dutton and X.-Y. Zhu, *Distance-Dependent Electronic Coupling at Molecule-Metal Interfaces: C_{60}/Cu(111)*, J. Phys. Chem. B **108**, 7788 (2004).

[8] K. Sokolowski-Tinten, C. Blome, J. Blums, A. Cavalleri, C. Dietrich, A. Tarasevitch, I. Uschmann, E. Fröster, M. Klammer, M. Horn von Hoegen, and D. von der Linde, *Femtosecond X-ray measurement of coherent lattice vibrations near the Lindemann stability limit*, Nature (London) **422**, 287 (2003).

[9] K. Sokolowski-Tinten, C. Blome, C. Dietrich, A. Tarasevitch, M. Horn von Hoegen, D. von der Linde, A. Cavalleri, J. Squier, and M. Kammler, *Femtosecond X-Ray Measurement of Ultrafast Melting and Large Acoustic Transients*, Phys. Rev. Lett. **87**, 225701 (2001).

[10] C. Rose-Petruck, R. Jimenez, T. Guo, A. Cavalleri, C. W. Siders, F. Rksi, J. A. Squier, B. C. Walker, K. R. Wilson, and C. P. J. Barty, *Picosecond milliÅngström lattice dynamics measured by ultrafast X-ray diffraction*, Nature (London) **398**, 310 (1999).

[11] C. Rischel, A. Rousse, I. Uschmann, P.-A. Albouy, J.-P. Geindre, P. Audeberti, J.-C. Gauthier, E. Fröster, J.-L. Martin, and A. Antonetti, *Femtosecond time-resolved X-ray diffraction from laser-heated organic films*, Nature (London) **390**, 490 (1997).

[12] A. M. Lindenberg, I. Kang, S. L. Johnson, T. Missalla, P. A. Heimann, Z. Chang, J. Larsson, P. H. Bucksbaum, H. C. Kapteyn, R. W. Lee, J. S. Wark, and R. W. Falcone, *Time-Resolved X-Ray Diffraction from Coherent Phonons during a Laser-Induced Phase Transition*, Phys. Rev. Lett. **84**, 111 (2000).

[13] K. Heinz, *LEED and DLEED as modern tools for quantitative surface structure determination*, Rep. Prog. Phys. **58**, 637 (1995).

[14] B. J. Siwick, J. R. Dwyer, R. E. Jordan, and R. J. D. Miller, *An atomic-level view of melting using femtosecond electron diffraction*, Science **302**, 1382 (2003).

[15] T. E. Felter, R. A. Baker, and P. J. Estrup, *Phase Transition on Mo(100) and W(100) Surfaces*, Phys. Rev. Lett. **38**, 1138 (1977).

[16] M. Aeschlimann, E. Hull, J. Cao, C. A. Schmuttenmaer, L. G. Jahn, Y. Gao, H. E. Elsayed-Ali, D. A. Mantell, and M. R. Scheinfein, *A picosecond electron gun for surface analysis*, Rev. Sci. Instrum. **66**, 1000 (1995).

[17] R. Karrer, H. J. Neff, M. Hengsberger, T. Greber, and J. Osterwalder, *Design of a miniature picosecond low-energy electron gun for time-resolved scattering experiments*, Rev. Sci. Instrum. **72**, 4404 (2001).

[18] X. Zeng, B. Lin, I. El-Kholy, and H. E. Elsayed-Ali, *Time-resolved reflection high-energy electron diffraction study of the Ge(111)-c(2×8)(1×1) phase transition*, Phys. Rev. B **59**, 14907 (1999).

[19] X. Zeng and H. E. Elsayed-Ali, *Time-resolved structural study of low-index surfaces of germanium near its bulk melting temperature*, Phys. Rev. B **64**, 085410 (2001).

[20] C.-Y. Ruan, V. A. Lobastov, F. Vigliotti, S. Y. Chen, and A. H. Zewail, *Ultrafast electron crystallography of interfacial water*, Science **304**, 80 (2004).

[21] J. R. Thompson, P. M. Weber, and P. J. Estrup, *Pump-probe low energy electron diffraction*, Proc. SPIE **2521**, 113 (1995).

[22] A. Dolocan, M. Hengsberger, H. J. Neff, M. Barry, C. Cirelli, T. Greber, and J. Osterwalder, *Electron-photon pulse correlator based on space-charge effects in a metal pinhole*, Jpn. J. Appl. Phys. **45**, 285 (2006).

[23] H. Park, S. Nie, X. Wang, R. Clinite, and J. Cao, *Optical Control of Coherent Lattice Motions Probed by Femtosecond Electron Diffraction*, J. Phys. Chem. B **109**, 13854 (2005).

[24] R. Kodama et al., *Plasma devices to guide and collimate a high density of MeV electrons*, Nature (London) **432**, 1005 (2004).

[25] Y. T. Li et al., *Observation of a Fast Electron Beam Emitted along the Surface of a Target Irradiated by Intense Femtosecond Laser Pulses*, Phys. Rev. Lett. **96**, 165003 (2006).

[26] A. Goldoni, C. Cepek, and S. Modesti, *First-order oriental-disordering transition on the (111) surface of* C_{60}, Phys. Rev. B **54**, 2890 (1996).

[27] A. Goldoni, C. Cepek, R. Larciprete, L. Sangaletti, S. Pagliara, G. Paolucci, and M. Sancrotti, *Core Level Photoemission Evidence of Frustrated Surface Molecules: A Germ of Disorder at the (111) Surface of* C_{60} *before the Order-Disorder Surface Phase Transition*, Phys. Rev. B **54**, 2890 (1996).

[28] Coherent Inc., Santa Clara, CA, USA.

[29] H. J. Neff, *Electronic and Structural Aspects of Metal on Semiconductor Surfaces and Development of a Time-Resolved Surface-Structure Probe*, PhD thesis, Universität Zürich, 2002.

[30] OCI Vacuum Microengineering Inc., London (Ontario), Canada.

[31] Spectroscopy Instruments GmbH, Gilching, Germany.

[32] VG (Vacuum Generators) Scienta, Hastings, United Kingdom.

[33] E.I. Altman and R.J. Colton, *The interaction of* C_{60} *with noble metal surfaces*, Surf. Sci. **295**, 13 (1993).

[34] C.-T. Tzeng, W.-S. Lo, J.-Y. Yuh, R.-Y. Chu, and K.-D. Tsuei, *Photoemission, near-edge x-ray-absorption spectroscopy, and low-energy electron-diffraction study of* C_{60} *on Au(111) surfaces*, Phys. Rev. B **61**, 2263 (2000).

[35] A. Tamai, *Molecular Arrangement and Electronic Properties of Low-Dimensional* C_{60} *systems*, PhD thesis, Universität Zürich, 2006.

[36] E.I. Altman and R.J. Colton, *Determination of the orientation of* C_{60} *adsorbed on Au(111) and Ag(111)*, Phys. Rev. B **48**, 18244 (1993).

[37] L. H. Tjeng, R. Hesper, A. C. L. Heessels, A. Heeres, H. T. Jonkman, and G. A. Sawatzky, *Development of the electronic structure in a K-doped* C_{60} *monolayer on a Ag(111) surface*, Solid State Commun. **103**, 31 (1997).

[38] C. Ton-That, A. G. Shard, S. Egger, V. R. Dhanak, and M. E. Welland, *Modulations of valence-band photoemission spectrum from* C_{60} *monolayers on a Ag(111) surface*, Phys. Rev. B **67**, 155415 (2003).

[39] Tomihiro Hashizume, K. Motai, X. D. Wang, H. Shinohara, Y. Saito, Y. Maruyama, K. Ohno, Y. Kawazoe, Y. Nishina, H. W. Pickering, Y. Kuk, and T. Sakurai, *Intramolecular structures of* C_{60} *molecules adsorbed on the Cu(111)-(1×1) surface*, Phys. Rev. Lett. **71**, 2959 (1993).

[40] R. Karrer, *Bau einer Elektronenkanone für zeitaufgelöste Beugung mit langsamen Elektronen (LEED)*, Diploma thesis, Universität Zürich, 2000.

[41] SIMION 3D 7.0 software package, Idaho National Engineering Laboratory, EG&G Idaho Inc., Idaho Falls.

[42] T. Greber, *Charge-transfer induced particle emission in gas surface reactions*, Surf. Sci. Reports **28**, 3 (1997).

[43] J.B. Pendry, *Low Energy Electron Diffraction*, Academic (London), 1974.

[44] M. A. Van Hove and S. Y. Tong, *Surface Cristallography by LEED*, Springer (Berlin), 1979.

[45] M.A. van Hove, W. H. Weinberg, and C.M. Chan, *Low-Energy Electron Diffraction*, Vol. 6 of *Springer Series in Surface Sciences*, ed. by G. Ertl and R. Gomer, Springer-Verlag (Berlin, Heidelberg, New York, London), 1986.

[46] H. E. Elsayed-Ali, *Surface Debye temperature measurement with reflection high-energy electron diffraction*, J. Appl. Phys. **79**, 6853 (1996).

[47] M. Fink and A. C. Yates, *Theoretical electron scattering amplitudes and spin polarizations. Part I.*, Atomic Data and Nuclear Data Tables. **1**, 385 (1970).

[48] M. Fink and J. Ingram, *Theoretical electron scattering amplitudes and spin polarizations. Part II*, Atomic Data and Nuclear Data Tables. **4**, 129 (1972).

[49] C. J. Davisson and L. H. Germer, *Diffraction of electrons by a crystal of nickel*, Phys. Rev. **30**, 705 (1927).

[50] N. C. Kothari, H. Over, and D. K. Saldin, *Optimum scaling for structural optimization in low-energy electron diffraction*, Phys. Rev. B **49**, 11088 (1994).

[51] M. Gierer and H. Over, *Complex surface structures studied by low-energy electron diffraction*, Z. Kristallogr. **214**, 14 (1999).

[52] H. Over, M. Gierer, H. Blundau, and G. Ertl, *Anisotropic thermal displacements of adsorbed atoms and molecules on surfaces studied by low-energy electron diffraction*, Phys. Rev. B **52**, 16812 (1995).

[53] J. T. McKinney, E. R. Jones, and M. B. Webb, *Surface Lattice Dynamics of Silver. II. Low-Energy Electron Thermal Diffuse Scattering*, Phys. Rev. **160**, 523 (1968).

[54] G. E. Laramore and C. B. Duke, *Effect of Lattice Vibrations in a Multiple-Scattering Description of Low-Energy Electron Diffraction. II. Double-Diffraction Analysis of the Elastic Scattering Cross Section*, Phys. Rev. B **2**, 4783 (1970).

[55] J. Yu, L. Bi, R. K. Kalia, and P. Vashishta, *Intermolecular and intramolecular phonons in solid C_{60}: Effects of orientational disorder and pressure*, Phys. Rev. B **49**, 5008 (1994).

[56] N.W. Ashcroft and N.D. Mermin, *Solid State Physics*, Saunders College (Philadelphia), 1976.

[57] P. J. Horoyski and M. L. W. Thewalt, *Optically detected librons and phonons in crystalline C_{60}*, Phys. Rev. B **48**, 11446 (1993).

[58] H. Park, J. Park, A. K. L. Lim, E. H. Anderson, A. P. Alivisatos, and P. L. McEuen, *Nanomechanical oscillations in a single-C_{60} transistor*, Nature (London) **407**, 57 (2000).

[59] J. C. Williamson, J. Cao, H. Ihee, H. Frey, and A. H. Zewail, *Clocking transient chemical changes by ultrafast electron diffraction*, Nature (London) **386**, 159 (1997).

[60] J. W. James, *The Optical Principles of the Diffraction of X Rays*, Bell, London, 1962.

[61] A. Dolocan, *Time-Resolved Low-Energy Electron Diffraction and Photoemission Pump-Probe Experiments*, PhD thesis, Universität Zürich, 2006.

[62] M. Hoesch, *Spin-Resolved Fermi Surface Mapping*, PhD thesis, Universität Zürich, 2002.

[63] K.-D. Tsuei, J.-Y. Yuh, C.-T. Tzeng, R.-Y. Chu, S.-C. Chung, and K.-L. Tsang, *Photoemission and photoabsorption study of C_{60} absorption on Cu(111) surfaces*, Phys. Rev. B **56**, 15412 (1997).

[64] Ch. Kusch, B. Winter, R. Mitzner, A. Gomes Silva, E. E. B. Campbell, and I V. Hertel, *Stability of photo-excited C_{60} chemisorbed on Ni(111)*, Chem. Phys. Lett. **275**, 469 (1997).

[65] W. I. F. David, R. M. Ibberson, J. C. Matthewman, K. Prassides, T. J. S. Dennis, J. P. Hare, H. W. Kroto, R. Taylor, and D. R. M. Walton, *Crystal structure and bonding of ordered* C_{60}, Nature (London) **352**, 147 (1991).

[66] P. J. Benning, F. Stepniak, and J. H. Weaver, *Electron-diffraction and photoelectron-spectroscopy studies of fullerene and alkali-metal fulleride films*, Phys. Rev. B **48**, 9086 (1993).

[67] S. T. Shipman, S. Garrett-Roe, P. Szymanski, A. Yang, M. L. Strader, and C. B. Harris, *Determination of Band Curvatures by Angle-Resolved Two-Photon Photoemission in Thin Films of* C_{60} *on Ag(111)*, J. Phys. Chem. B **110**, 10002 (2006).

[68] K. Allen and F. Hellman, *Specific heat of* C_{60} *and* K_3C_{60} *thin films for* $T = 6 - 400\,\mathrm{K}$, Phys. Rev. B **60**, 11765 (1999).

[69] P. B. Johnson and R. W. Christy, *Optical Constants of the Noble Metals*, Phys. Rev. B **6**, 4370 (1972).

Acknowledgements

I would like to thank all the people who helped me during the realization of this work.

First of all I'm very grateful to Prof. Herbert Over and Jürg Osterwalder who gave me the opportunity to perform the experiments presented here in their groups in Giessen and Zürich, respectively.

Prof. Over was my guide in the first nine months of my thesis, that I spent in Giessen, and I would like to thank him not only for his precious teachings regarding surface science and LEED but also for all the help in the "logistics" of the ordinary life, in particular for his efforts in dealing with the German bureaucracy.

I thank Prof. Osterwalder for the enthusiasm and the interest he always reserved to my work. Many times his clear explanations were necessary to identify the major problems, solve them and find back the correct way; and I'm particularly grateful to him for the realization of the space-charge simulation program.

My advisor in Zürich, Prof. Thomas Greber was a continuous source of ideas and suggestions, which contributed to give new lymph to the project, especially when it seemed to be unfeasible: any discussion in his office was always a boost towards the final results, of course never forgetting that "Einmal ist keinmal". Moreover we share the same passion for traveling and visiting the most remote sites of world.

Most of the work presented here would not have been possible without the contribution of Dr. Matthias "Matze" Hengsberger: he helped to move my first steps in the Laser Lab and was always at disposal for any problem, not only regarding the experiments. His great skills and expertise in the *time-resolved world* were essential in any part of this work.

For the construction of the new electron gun, I have profited from the support of different people: thanks to Prof. Hans-Werner Fink and his group for all the pieces of wonderful gold mesh they gave me; thanks to Hansruedi Scherrer from ETH Zürich for the preparation of the photocathodes; thanks to Martin (Klöckner) for all the technical problems solved and for the designs of the gun and to all the team of our workshop led by Kurt Bösiger for their amazing work in constructing many sub-millimiter pieces and their always prompt collaboration; thanks to Prof. Andreas Schilling and Raffaele Dell'Amore for letting me use their microscope to assemble the gun head.

When I started in Giessen, the group was still quite small, nevertheless it was nice to share the office with Attila Farkas and discuss with Marcus Knapp, Georg Mellau, Stefan Klee and Bernhard Schwabe.

Special thanks go to my colleagues of the Laser Lab Andrei, who taught me how to work with our femtosecond laser system, and Dominik, who was also my office mate in the

last year of my thesis; Dominik, thanks for *that* translation! In the last months of my thesis, I really enjoyed sharing the office also with Carine and Cynthia.

Furthermore it was a great pleasure to work in the Surface Physics group with all the other colleagues: Anna, Martina, Matthias (Muntwiler), Milan, Richard, Jorge, Louis, Simon, Martin (Morscher), Thomas (Brugger) (thanks for the SI units package!), Thomas (Mattle) and Taichi.

Each of them contribute with his own character to the cheerful atmosphere, which is often envied by people visiting the surface physics group.

Out of the group I cannot forget thanking other PhD students of the Physics Institute like Fabio, Marco, Raffaele, who were always ready to sustain me in many *dark days* (literally!) spent in the Laser Lab.

Thanks to Andrea because it is also “his fault” if I came here to Zürich and for welcoming me in his beautiful small house in the first months; and thank you for bearing all those boring discussion in the evenings.

Infine, ringrazio i miei genitori, mio fratello Marco e Anna per avermi sempre aiutato e Franci semplicemente ... per tutto, per avermi sempre incoraggiato e per essere in grado di sopportarmi ogni giorno.

Curriculum Vitae

Name	Claudio Cirelli
Birth	28.04.1977 in Milano, Italy
Nationality	Italian

Education

1991-1996	Liceo Scientifico Statale “B. Pascal”, Milano, Italy
Jun 1996	**Maturita’ scientifica**
1996-2002	Undergraduate **Studies of Physics, Milano University**
Jan 2001-Feb 2002	Diploma work at the University of Milano-Bicocca at the Department of Materials Science in the “Chemical Physics of Semiconductors: Defects, Impurities and Surfaces” Group of Prof. S. Pizzini *Thesis Title*: “Study of the correlation between radiative and non-radiative recombination channels in single crystal silicon”; supervisors: Prof. P. Milani (Milano University) and Prof. S. Pizzini (University of Milano-Bicocca)
Feb 2002	Graduation with full marks (110/110 *cum laude*)
Feb 2002-Jun2002	Collaboration at the Material Science Dept. of Milano-Bicocca University in the context of the European Reasearch Project FAST-IQ (Fast inline characterization tools for crystalline silicon material and cell process quality control in the PV-Industry).
since Jan 2003	**Employed as PhD student** in the Surface Chemistry and Model Catalysis Group of Prof. Dr. Herbert Over, **University of Giessen**, Germany in collaboration with the Surface Physics Group of Prof. Dr. Jürg Osterwalder, University of Zurich
since Apr 2006	**Employed as PhD student at the University of Zürich**
Nov 2006	PhD Thesis; *Title*: “Dynamics of Space-Charge and Molecules on Surfaces investigated by Means of Picosecond Low-Energy-Electron-Diffraction”; supervisors: Prof. Dr. J. Osterwalder, Prof. Dr. T. Greber and Dr. M. Hengsberger

Teaching and Working Experiences

since Apr 2004	Teaching Assistant, University of Zurich; taught lab-courses for medical students and problem classes in elementary and advanced solid state physics.
2001-2002	English to Italian translations of patents concerning growth techniques of semiconductor materials (MEMC Electronic Materials).
2001-2003	Collaboration with Parma and Genoa research units of INFM (National Institute for the Physics of Matter) on exhibitions of popular science subjects in meetings and conferences.

Publications

1. M. Acciarri, **C. Cirelli**, S. Pizzini, S. Binetti, A. Castaldini and A. Cavallini,
   "Study of the correlation between radiative and non-radiative recombination channels in silicon",
   Journal of Physics-Condensed Matter **14 (48)**, 13223 (2002), (Proceedings of the "Conference on Extended Defects in Semiconductors (EDS2002), Bologna, taly, June 2002)

2. A. Dolocan, M. Hengsberger, H. J. Neff, M. Barry, **C. Cirelli**, T. Greber and J. Osterwalder,
   "Electron-Photon Pulse Correlator Based on Space-Charge Effects in a Metal Pinhole",
   Japanese Journal of Applied Physics, **45**, 285 (2006)

3. **C. Cirelli**, M. Hengsberger, H. Over, T. Greber and J. Osterwalder,
   "Direct observation of Space-Charge dynamics by means of picosecond Low-Energy-Electron-Diffraction",
   in preparation (2006)

4. **C. Cirelli**, M. Hengsberger, H. Over, T. Greber and J. Osterwalder,
   "Design of a high-flux electron gun for picosecond Low-Energy-Electron-Diffraction experiments",
   in preparation (2006)